

**Detailed Photophysical Investigations of OLED  
Relevant Cu(I) Complexes – From Phosphorescence  
to Thermally Activated Delayed Fluorescence  
(TADF)**



**Dissertation**

zur Erlangung des Doktorgrades der Naturwissenschaften (Dr. rer. nat.)

an der Fakultät für Chemie und Pharmazie

der Universität Regensburg

vorgelegt von

**Alexander Schinabeck**

2020

Promotionsgesuch eingereicht am: 27. August 2020  
Tag der mündlichen Prüfung: 4. Dezember 2020

Diese Arbeit wurde angeleitet von Herrn Prof. Dr. Hartmut Yersin am Institut für Physikalische und Theoretische Chemie der Universität Regensburg.

Prüfungsausschuss: Prof. Dr. Arno Pfitzner, Vorsitzender  
Prof. Dr. Bernhard Dick, Erster Gutachter  
Prof. Dr. Hartmut Yersin, Zweiter Gutachter  
Prof. Dr. Manfred Scheer

## Parts of this thesis have been published previously

Dinuclear Cu(I) Complex with Combined Bright TADF and Phosphorescence. Zero-Field Splitting and Spin-Lattice Relaxation Effects of the Triplet State

**Schinabeck, A.**; Leitl, J. M.; Yersin, H., *J. Phys. Chem. Lett.* **2018**, *9*, 2848-2856

Deep blue emitting Cu(I) tripod complexes. Design of high quantum yield materials showing TADF-assisted phosphorescence

**Schinabeck, A.**; Rau, N.; Klein, M.; Sundermeyer, J.; Yersin. *Dalton Trans.* **2018**, *47*, 17067-17076

Symmetry-Based Design Strategy for Unprecedentedly Fast Decaying Thermally Activated Delayed Fluorescence (TADF). Application to Dinuclear Cu(I) Compounds

**Schinabeck, A.**; Chen, J.; Kang, L.; Teng, T.; Homeier, H. H. H.; Suleymanova, A. F.; Shafikov, M. Z.; Yu, R.; Lu, C.-Z.; Yersin, H. *Chem. Mater.* **2019**, *31*, 4392-4404

## Further publications

Copper(I) Complexes for Thermally Activated Delayed Fluorescence: From Photophysical to Device Properties

Leitl, M. J.; Zink, D. M.; **Schinabeck, A.**; Baumann, T.; Volz, D.; Yersin, H., *Top. Curr. Chem.* **2016**, *374*, 1-34.

Dinuclear Ag(I) Complex Designed for Highly Efficient Thermally Activated Delayed Fluorescence

Shafikov, M. Z.; Suleymanova, A. F.; **Schinabeck, A.**; Yersin, H., *J. Phys. Chem. Lett.* **2018**, *9*, 702-709

Gold(I) Complexes Containing Phosphanyl- and Arsanylborane Ligands

Bräse, J.; **Schinabeck, A.**; Bodensteiner, M.; Yersin, H.; Timoshkin Y. A.; Scheer, M., *Chem. Eur. J.* **2018**, *24*, 10073-10077

Sky-blue thermally activated delayed fluorescence (TADF) based on Ag(I) complexes: strong solvation-induced emission enhancement

Artem'ev, A. V.; Shafikov, M. Z.; **Schinabeck, A.**; Antonova, O. V.; Berezin, A. S.; Bagryanskaya, I. Y.; Plusnin, P. E.; Yersin, H., *Inorg. Chem. Front.* **2019**, *6*, 3168-3176

Cu(I) and Ag(I) complexes with a new type of rigid tri-dentate N,P,P-ligand showing highly efficient TADF and remarkable OLED performance

Klein, M.; Rau, N.; Wende, M.; Sundermeyer, J.; Cheng, G.; Che, C.-M.; **Schinabeck, A.**; Yersin, H., *Chem. Mater.* **2020**, *32*, 10365-10382

Cu(I) Complexes of Multidentate N,C,N- and P,C,P-Carbodiphosphorane Ligands and their Photoluminescence

Klein, M.; Demirel, N.; **Schinabeck, A.**; Yersin, H.; Sundermeyer, J. *Molecules* **2020**, *25*, 3990

## Content

Motivation .....	6
1 Di-nuclear Cu(I) complex showing bright TADF combined with phosphorescence.....	9
1.1 Theoretical Characterization and Photophysical Issues.....	10
1.3 Emission spectra, quantum yields and TADF.....	13
1.4 Decay dynamics and electronic structure.....	15
1.5 Combined TADF and Phosphorescence at ambient Temperature.....	20
1.6 Spin-Lattice Relaxation (SLR) and Zero-field splitting (ZFS).....	21
1.7 Conclusion.....	23
2 Deep blue Cu(I) tripod complexes – increase of quantum yield by tuning sterical hindrance.....	24
2.1 Synthesis and structural characterization.....	25
2.2 Computational studies.....	26
2.3 Quantum yield design. Steric demands and host rigidity .....	28
2.4 Absorption and emission spectra .....	30
2.5 Detailed electronic structure of [Cu(tpym)(P(o-tol) <sub>3</sub> )]PF <sub>6</sub> 3 .....	31
2.6 Combined emission. Interplay between phosphorescence and TADF .....	34
2.7 Conclusion.....	36
3 Symmetry based design strategy of dinuclear Cu(I) compounds with unprecedentedly fast decaying TADF.....	37
3.1 Monomer Cu(dppb)(PPh <sub>3</sub> )Cl .....	40
3.1.1 Synthesis and chemical characterization .....	40
3.1.2 DFT and TD-DFT calculations of the monomer Cu(dppb)(PPh <sub>3</sub> )Cl ..	40
3.1.3 Photophysical studies of the monomer Cu(dppb)(PPh <sub>3</sub> )Cl .....	42
3.2. Dimers Cu <sub>2</sub> (tppb)(PPh <sub>3</sub> ) <sub>2</sub> X <sub>2</sub> with X = Cl 6, Br 7, I 8, and NCS 9 .....	47
3.2.1 Syntheses and chemical characterizations .....	47
3.2.2 DFT and TD-DFT calculations for the representative dimer Cu <sub>2</sub> (tppb)(PPh <sub>3</sub> ) <sub>2</sub> Cl <sub>2</sub> 6.....	47
3.3 TD-DFT calculations and guiding model .....	50

3.4 Photophysical studies of the dimer $\text{Cu}_2(\text{tppb})(\text{PPh}_3)_2\text{Cl}_2$ .....	51
3.5 Comparison of photophysical properties of the different dimers studied..	56
3.6. Highlights of the guiding-model dimers .....	58
3.7. Conclusion and outlook.....	61
Conclusion.....	62
Experimental.....	63
References .....	64
Danksagung .....	75
Erklärung .....	76

## Motivation

In the last decades organic light emitting diodes (OLEDs) steadily gained attention. Their value in display technology and next generation lighting is tremendous.

OLED lighting products do not emit UV light and may therefore also be used for challenging tasks, like in museums or art galleries,<sup>1,2</sup> where they can serve as a sensitive, pigment conserving light source. Furthermore, OLEDs are able to provide daylight-like warm and natural white light with qualities quite close to daylight, avoiding the additional amounts of potentially unhealthy blue light components in LEDs.<sup>2-4</sup> However, due to its high production costs and problems with long-term stability, OLED illumination is still a niche product.

Though, OLED displays are already available as high quality technological product. They show better image quality, enhanced contrast, higher brightness, a larger viewing angle, a wider range of colors and much faster refresh rates compared to the still widely used liquid crystal displays (LCDs).<sup>5</sup>

OLED technology was implemented first in small displays of smart watches, smartphones, tablets but nowadays also in larger TV screens (up to 87.6 inch Diag<sup>6</sup>). Due to the ever growing implementation of OLEDs, Display Supply Chain Consultants (DSCC) expects an increase of the OLED display market from \$26.5 billion in 2018 to \$46.2 billion by 2023.<sup>7</sup>

This huge success story began with a discovery of Henry. J. Round. He observed in 1907 light emission for certain substances exposed to an electric field, the so-called electroluminescence. In his landmarking contribution *A note on carborundum*, he describes the light emission of carborundum crystals (SiC) as yellow at a potential of 10 V and depending on a specific sample as yellow light-green, orange or blue, when a potential of 110 V got applied.<sup>8</sup>

The next important step towards modern *organic* LEDs was the observation of light emission from single crystal anthracene at a voltage above about 400 V, achieved in 1963 by Pope et al.<sup>9</sup> Here, the necessary high operating voltage is to be attributed to the layer thickness of the OLED device. As a consequence, a significant progress was made, when Tang and Van Slyke presented 1987 a thin-layer OLED with an operating voltage below 10 V.<sup>10</sup>

In their publication a four-layer OLED device is depicted, consisting of the following subsequent layers (from top to bottom): a Mg:Ag cathode, a recombination/emissive layer of 8-hydroxyquinoline aluminium (Alq<sub>3</sub>, thickness about 600 Å), a diamine layer (hole transport layer HTL, thickness about 750 Å) and an indium-tin-oxide (ITO) anode. Where the Alq<sub>3</sub> layer acting as combination of an electron transporting layer (ETL)<sup>11</sup> and an emissive layer.

In modern OLED devices, these layers are separated and consist as a consequence of at least a five-layer stack, containing an electron transport layer and an emitter doped

emissive layer.

In the following a summary of the discussion of the working principle, including the radiative and non-radiative decay paths in an OLED device is reproduced:<sup>11,12</sup>

- From the side of the anode (ITO) holes and from the side of the cathode (for example Mg:Ag) electrons get injected in the OLED stack.
- Under the driving force of the electric field the holes move through the hole transport layer (HTL) and the electrons through the electron transport layer (ETL) in order to meet in the electron-hole recombination/emission layer. This movement can be described as a thermally activated hopping process in each layer.<sup>11</sup>
- In the emission layer, the emitter and matrix molecules, respectively, are subject to be oxidized by holes or reduced by electrons.
- if the distance of an electron and hole falls below a certain distance  $R$ , a long-range Coulomb attraction becomes effective
- Such a pair of electron and hole is denoted as „exciton“. Since both charges carries a spin, triplet and singlet excitons are obtained at a 3:1 ratio.
- Due to the electrostatic interaction, the exciton is finally “trapped” at the emitter molecule
- After relaxation, the first singlet ( $S_1$ ) or first triplet ( $T_1$ ) state of the emitter molecule is excited, depending on the spin multiplicity.
- It is also possible that the exciton can be “trapped” at a matrix molecule.
- In this case a matrix molecule in the excited singlet or triplet state results (formation probability 3:1 ratio)
- By long-range Förster energy transfer mechanism, the singlet excitation energy and by short-range Dexter energy transfer mechanism the triplet energy of the excited matrix molecules can be also transferred to the emitter molecule
- In that way, all excitations are transferred to the emitter molecule
- Thereafter, the relaxation of the emitter compound to the ground state of the emitter compound occurs by radiative or non-radiative decay paths.

At that point, the photophysical properties of the applied emitter molecules are crucial for the efficiency of an OLED device. There are three basic groups of OLED emitter compounds: *organic (prompt) fluorescent, triplet- and singlet harvesting emitters*. In OLED devices utilizing organic or usual fluorescent emitter compounds only 25 % of the singlet excitons formed contribute to generation of light, since the transition from the excited triplet to the singlet ground state is spin forbidden for 75% of the emitter molecules and therefore non-radiative. Thus, three quarters of the induced energy is wasted. The percentage of the injected charges (e.g. electrons) which lead to the formation of a photon within a device is described by the internal quantum yield.<sup>13</sup> In

the example presented, the internal quantum yield cannot be larger than 25 %.

A first improvement is constituted by the introduction of a triplet harvesting mechanism in 1998 by Thompson and Forrest et al.<sup>14</sup> as well as by Chi-Ming Che et al.<sup>15</sup> According to this mechanism, 100 % internal OLED quantum efficiency may be achieved. However, this success is achieved by using high-cost 3rd row organo-transition metal compounds, such as Ir(III)<sup>12,16-23</sup> or Pt(II)<sup>12,14,16,17,22,24-32</sup> complexes. In such complexes metal ions induce high spin-orbit coupling (SOC) which opens fast intersystem crossing (ISC) and effective phosphorescence pathways ( $T_1 \rightarrow S_0$ , with  $T_1$  and  $S_0$  being the lowest triplet state and the electronic ground state, respectively). Besides the high costs of the rare metals, another challenge is the research of stable 3<sup>rd</sup> row organo-transition metal complexes, which show blue light emission.

Because of lacking breakthrough in this regard, Yersin et al.<sup>33</sup> proposed in 2006/2008 application of compounds that show thermally activated delayed fluorescence (TADF) in OLEDs as an alternative mechanism to harvest all singlet and triplet excitons through emission from the lowest singlet state  $S_1$ . This mechanism was named “singlet harvesting mechanism”.<sup>33-35</sup>

The requirement for efficient TADF, and hence efficient singlet harvesting, is a small energy separation between the lowest excited triplet state  $T_1$  and the lowest excited singlet state  $S_1$  ( $\Delta E(S_1-T_1) \approx 1000 \text{ cm}^{-1}$  or less) as well as a fast radiative rate (high allowedness) of  $k_r(S_1 \rightarrow S_0)$ .<sup>36-38</sup> Suitable emitter molecules can be charge transfer (CT) compounds, such as Cu(I)<sup>34,35,37,39-59</sup> or Ag(I)<sup>36,60-64</sup> complexes as well as purely organic molecules.<sup>65-73</sup> Due to the promising properties of Cu(I) complexes, namely low-cost, blue emitting compounds and enabling 100 % internal quantum yield, the “Bundesministerium für Bildung und Forschung” (German Ministry of Education and Research) supported the research of Cu(I) complex singlet-harvesting OLEDs. Within this research project called cyCESH new efficient Singulett-Harvesting Cu(I) complexes were designed and characterized.<sup>74</sup> These large scale investigations strongly stimulated the scientific and material research in the field of Cu(I) complex - TADF compounds substantially. However, several basic problems were not yet addressed in this project. Accordingly, the focus of this thesis lies in deeper studies of selected compounds and in the development of improved Cu(I) based - TADF materials. These investigations are addressed in three chapters.

In the first chapter, a Cu(I) dimer exhibiting a short emission decay time of 7  $\mu\text{s}$  with the high emission quantum yield  $\Phi_{\text{PL}}$  of 85 % at ambient temperature is presented. In a comprehensive discussion the short emission decay is explained by the significant  $T_1$  state phosphorescence in addition to the  $S_1$  state TADF emission at ambient temperature. Due to this strong participation it was instructive to discuss zero-field splitting of the  $T_1$  state and effects of spin-lattice relaxation (SLR) for this Cu(I) complex in detail.

In the second chapter a design strategy is described to achieve high photoluminescence emission quantum yield of Cu(I) complexes in degassed solution. This is a quite difficult task, because Cu(I) complexes usually undergo distinct geometry distortions after electronic excitations. The resulting large Franck-Condon (FC) factors lead to a strong increase of the non-radiative rates and therefore to a small photoluminescence emission quantum yield, especially in non-rigid environments. It is described in detail how it was possible to reduce these geometry distortions and obtain the outstanding emission quantum yield of a Cu(I) complex of  $\Phi_{\text{PL}} = 76\%$  in degassed solution

The investigated compounds show also the effect of a significant participation of the  $T_1$  state emission to the emission at ambient temperature which is investigated in detail in chapter 1. Since the phosphorescence dominates the ambient temperature emission it is named as TADF-assisted phosphorescence.

In the last chapter, the lower limit of about  $4\ \mu\text{s}$ <sup>75</sup> TADF emission decay time gets disproved. This was a challenging task, since both for effective TADF crucial requirements, a small  $\Delta E(S_1-T_1)$  and a fast radiative rate (high allowedness)  $k_r(S_1 \rightarrow S_0)$  can usually not be obtained at the same time. This is rationalized by a small exchange interaction due to a small donor-HOMO to acceptor-LUMO overlap and, in this situation, mostly also in a small transition dipole moment results, giving a small radiative rate  $k_r(S_1 \rightarrow S_0)$ . Although these requirements (a small  $\Delta E(S_1-T_1)$  and a fast  $k_r(S_1 \rightarrow S_0)$ ) are contradictory, in this chapter a group of four Cu(I) dimer compounds is presented, which show an extraordinarily short radiative emission decay time between  $\tau = 1.5\ \mu\text{s}$  and  $1.8\ \mu\text{s}$ . For the design of these dinuclear complexes a schematic guiding model inspired by the Davidov model was applied.

## **1 Di-nuclear Cu(I) complex showing bright TADF combined with phosphorescence**

This chapter has been published recently in reference 53. The focus of this chapter lies on a discussion of the lowest excited singlet and triplet states as well as on TADF properties of a dinuclear Cu(I) complex, in which the two Cu(I) centers are bound by two iodo-bridges in a  $\text{Cu}_2\text{I}_2$  core and additionally by a third bridge consisting of an  $\text{N}^{\wedge}\text{P}$  ligand (Figure 1.1). Due to this structure motif,<sup>76</sup> the compound shows an exceptional structural rigidity which is advantageous for reducing nonradiative processes and thus, for obtaining high emission quantum yield  $\Phi_{\text{PL}}$ . Moreover, this compound is very soluble in organic solvents, such as dichloromethane or toluene, due to the *n*-butyl functionalization of the 1,2,4-triazole ligand.<sup>77</sup> Therefore, application of  $\text{Cu}_2\text{I}_2(\text{P}^{\wedge}\text{N})_3$  **1** as emitter for solution-processed OLEDs is proposed.

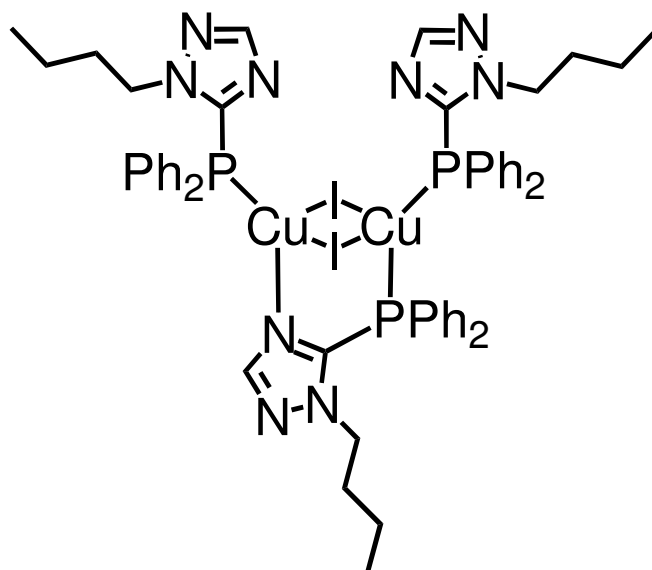


**Figure 1.1:** Chemical structure of  $\text{Cu}_2\text{I}_2(\text{P}^{\wedge}\text{N})_3$  **1** ( $\text{Cu}_2(\mu\text{-I})_2(1N\text{-}n\text{-butyl-5-diphenylphosphino-1,2,4-triazole})$ ).

In a first report, this complex was already described with respect to its synthesis and chemical characterization.<sup>77</sup> Moreover, first photophysical investigations carried out with the powder material indicated a high photoluminescence quantum yield  $\Phi_{\text{PL}}$  combined with a short emission decay time at ambient temperature. In particular, these properties stimulated us to study photophysical details of  $\text{Cu}_2\text{I}_2(\text{P}^{\wedge}\text{N})_3$  **1**. The investigations presented here reveal that the ambient-temperature emission represents the rare situation where phosphorescence *and* TADF contribute to the emission at ambient temperature.<sup>78,79</sup> According to this two-path emission, an overall shorter decay time is obtained. This behavior is of particular interest because it can only occur for compounds that show relatively high SOC of the emitting  $T_1$  state with (a) nearby lying singlet state(s)  $S_n$ . Further, significant SOC should have a clear impact on the  $T_1$  state properties. Therefore, not only is a higher rate of the  $T_1 \rightarrow S_0$  transition (phosphorescence) expected, but in contrast to most other Cu(I) complexes, significant zero-field splitting (ZFS) of the triplet into substates should occur. Such a splitting is expected to be combined with specific relaxation processes between these substates, i.e., effects of spin-lattice relaxation (SLR), should be observable. Accordingly, in this chapter the interplay of phosphorescence and TADF with temperature change as well as triplet state properties, such as ZFSs and effects of SLR will be studied.

## 1.1 Theoretical Characterization and Photophysical Issues

Results from density functional theory (DFT) and time-dependent DFT (TD-DFT) calculations provide first information about the electronic structure and the state dependent geometries of the complex. The calculations were performed at the B3LYP<sup>80</sup>/def2-SVP level of theory at gas phase conditions (including electron core

potentials (ECP) for iodine atoms)<sup>81</sup> using the NWChem 6.5 code.<sup>82</sup> As discussed below, the lowest states will be assigned as charge transfer (CT) states. With this excitation substantial structural changes between the electronic ground state and the emitting excited state occur. Similar structural changes were reported for other Cu(I) and Ag(I) complexes with CT character of the lowest excited states.<sup>17,34,35,37,45,46,49,50,52,54,56,60-62,64,78,83-93</sup> Such geometry changes usually favor extensive nonradiative relaxations that are connected with small emission quantum yields.<sup>35,37,49,56,94</sup> However, a rigid environment will frequently reduce the extent of geometry change and, thus, can lead to high emission quantum yields.<sup>17,34-37,46,49,52,56,60,61,64,87,89-91,93</sup>

In the context of this chapter, the focus is on emission properties. Therefore, the TD-DFT calculations are carried out in the optimized T<sub>1</sub> state geometry. The resulting frontier orbitals show that the HOMO is mainly distributed over the copper(I) centers (49 %) and iodine atoms (27 %), whereas the LUMO is localized on the bridging 1*N*-*n*-butyl-5-diphenyl-phosphino-1,2,4-triazole ligand (Figure 1.2). Thus, a transition between the spatially well separated HOMO and LUMO may be assigned as (metal+iodide)-to-ligand (M+I)LCT transition, shortly as a CT transition. According to TD-DFT calculations, the resulting states <sup>1</sup>((M+I)LCT) (S<sub>1</sub>) and <sup>3</sup>((M+I)LCT) (T<sub>1</sub>) are both of 98 % HOMO → LUMO character. Thus, both HOMO and LUMO correspond largely to “hole” and “electron” of natural transition orbitals, respectively. Due to the significant spatial separation of HOMO and LUMO, a small exchange integral and accordingly, a small ΔE(S<sub>1</sub>-T<sub>1</sub>) value is expected.<sup>95,96</sup> Indeed, the TD-DFT calculations give a value of ΔE(S<sub>1</sub>-T<sub>1</sub>) ≈ 290 cm<sup>-1</sup> (36 meV), close to the experimentally determined activation energy of 430 cm<sup>-1</sup> (53 meV) (see below). This small singlet-triplet splitting would be well suited for an efficient TADF effect. Hence, a short TADF decay time is expected to occur.

A complete calculation that includes SOC is rather demanding and costly. However, a very simple approach can also help to get an indication, whether SOC between the T<sub>1</sub> state and a higher lying singlet state S<sub>n</sub> can be important.<sup>36,37</sup> It is well-known that SOC between the T<sub>1</sub> and S<sub>1</sub> states is negligible, if both states result from the same HOMO-LUMO transition.<sup>12,16,17,22,97</sup> For efficient SOC, mixing with a state that carries different d-orbital character than the T<sub>1</sub> state is required. Moreover, the corresponding energy separation should be less than about 0.5 eV (4000 cm<sup>-1</sup>).<sup>37</sup> Indeed, the calculated energy gap between HOMO and HOMO-1 comprising different d-orbitals amounts to 0.31 eV.

The related excited state is S<sub>2</sub>. The calculated energy separation amounts to ΔE(S<sub>2</sub>-T<sub>1</sub>) ≈ 2900 cm<sup>-1</sup> (360 meV). Due to this relatively small value, mixing of the S<sub>2</sub> state to the T<sub>1</sub> state is expected to be significant (compare ref. 98). Accordingly, distinct SOC should occur and influence the triplet state properties. Indeed, experimentally, this is clearly observed, as shown below.

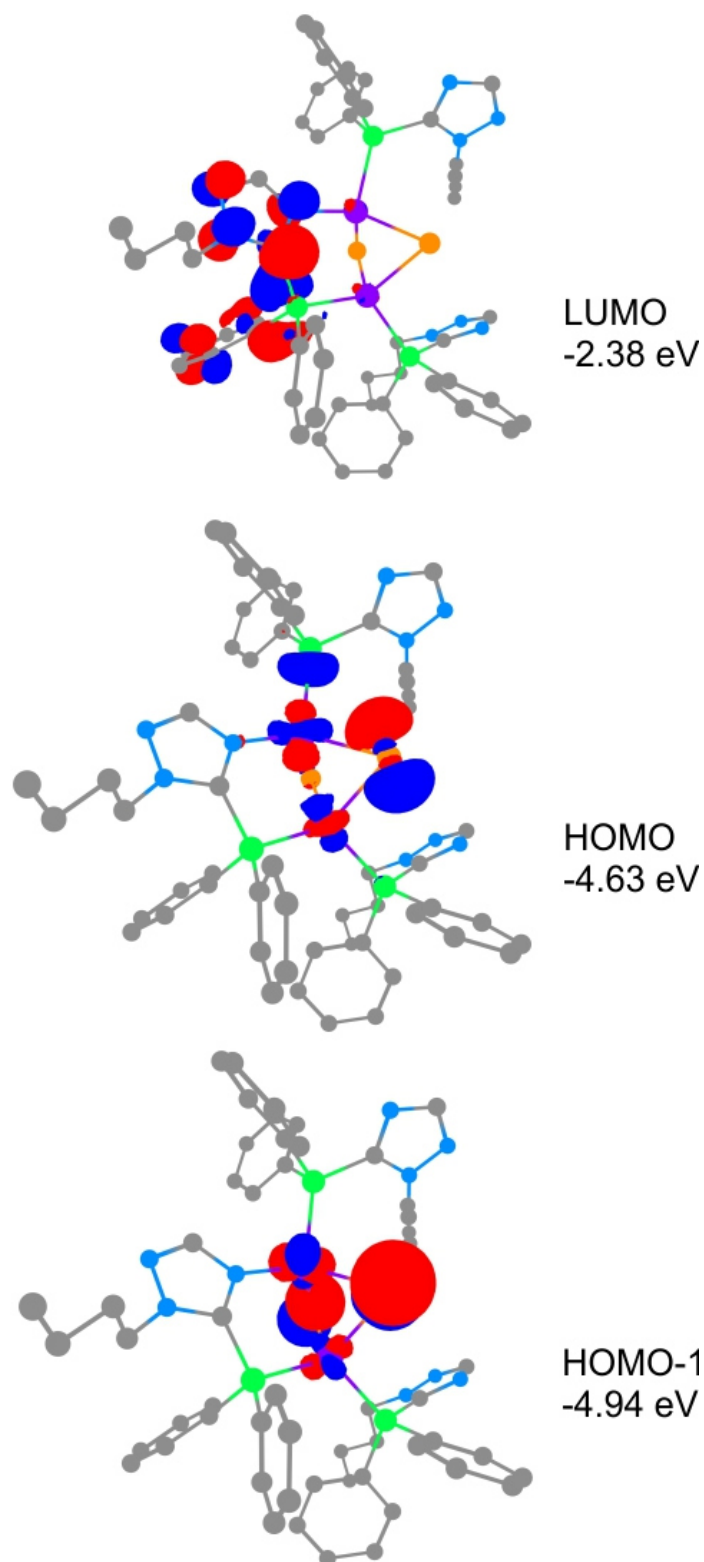


**Figure 1.2:** HOMO-1, HOMO and LUMO contour plots (isovalue = 0.05) of the geometry-optimized  $T_1$  state of  $\text{Cu}_2\text{I}_2(\text{P}^{\wedge}\text{N})_3$  **1** as well as the corresponding energies. Hydrogen atoms are omitted for clarity. The atoms are characterized by colors: Cu purple, I orange, P green, N blue, and C gray.

### 1.3 Emission spectra, quantum yields and TADF

$\text{Cu}_2\text{I}_2(\text{P}^\wedge\text{N})_3$  **1** was synthesized, purified and provided by Dr. Thomas Baumann and Dr. Daniel Zink et al. as reported in ref. 77. Figure 1.3 displays the 300 K excitation spectrum and emission spectra measured at different temperatures.

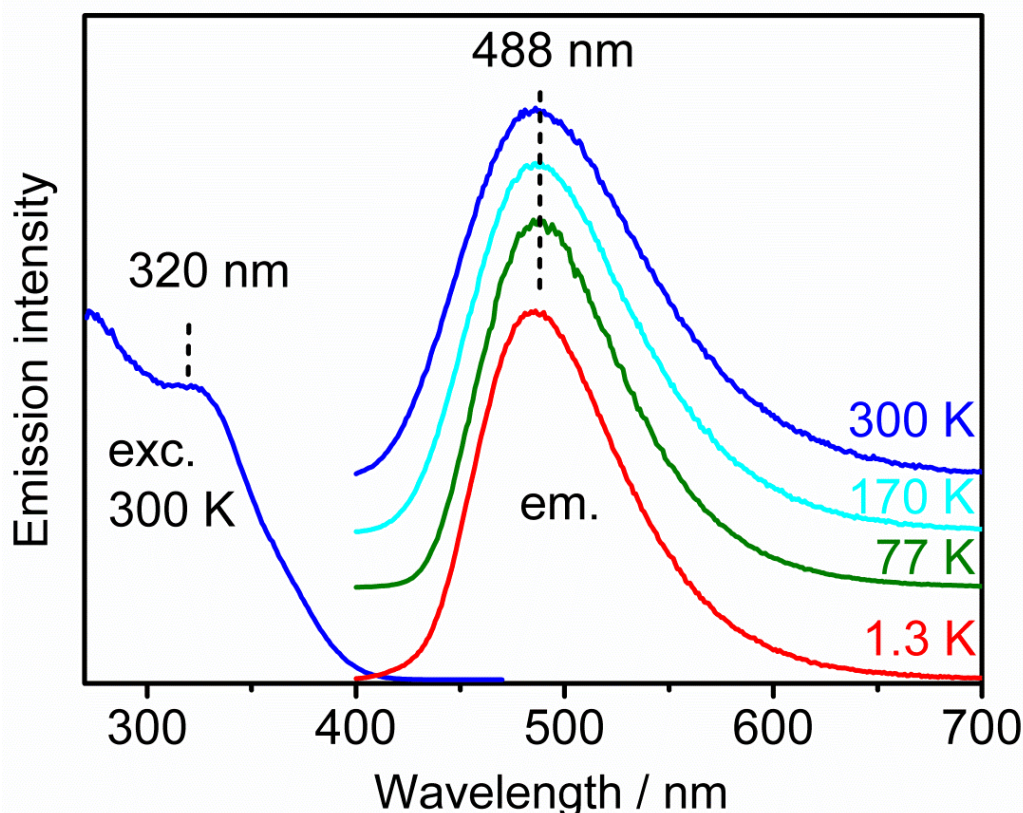


**Figure 1.3:** Excitation spectrum at 300 K and emission spectra of  $\text{Cu}_2\text{I}_2(\text{P}^\wedge\text{N})_3$  **1** powder at different temperatures;  $\lambda_{\text{exc}} = 330$  nm,  $\lambda_{\text{det}} = 490$  nm.

The excitation spectrum shows a shoulder at about 320 nm, and a distinct tail in the range of  $\approx 350$  nm to 415 nm. According to TD-DFT calculations and in analogy to literature assignments, the high-energy absorption in the wavelength range below 325 nm is assigned to ligand-centered transitions, while the long-wavelength tail is characterized to CT transition(s).<sup>36,49,54,99</sup> The emission is assigned to stem from the lowest excited  $^1,^3\text{CT}$  states. The spectra are broad and unstructured in the whole temperature range studied. This is consistent with the CT assignment. Interestingly, apart from a slight reduction of the emission bandwidth, no obvious spectral change is observed, even when cooled to  $T = 1.3$  K. Although the emission character strongly changes with temperature increase (see below), this behavior is not displayed in the spectra due to the relatively small singlet-triplet splitting  $\Delta E(\text{S}_1-\text{T}_1)$ . As a consequence, the emissions from the two states  $\text{T}_1$  and  $\text{S}_1$  essentially overlap. Also, the emission quantum yield is only slightly temperature-dependent, amounting to  $\Phi_{\text{PL}}(77 \text{ K}) \approx 100 \%$

and  $\Phi_{\text{PL}}(300 \text{ K}) = 85 \%$ . This small reduction is attributed to a frequently observed increase of emission quenching with increasing temperature.<sup>94</sup>

On the other hand, the emission decay time  $\tau$  changes drastically; for example, at  $T = 77 \text{ K}$  and  $300 \text{ K}$ ,  $52 \mu\text{s}$  and  $7 \mu\text{s}$ , respectively, at monoexponential decay dynamics are found. With these data and the  $\Phi_{\text{PL}}$  values, the radiative rates  $k_r = \Phi_{\text{PL}} \tau^{-1}$  can be determined as  $k_r(77 \text{ K}) = 1.9 \cdot 10^4 \text{ s}^{-1}$  and  $k_r(300 \text{ K}) = 12 \cdot 10^4 \text{ s}^{-1}$ , representing an increase by a factor of 6.3. The nonradiative rates can also be calculated according to  $k_{\text{nr}} = (1 - \Phi_{\text{PL}}) \tau^{-1}$ , giving  $k_{\text{nr}}(300 \text{ K}) = 2.1 \cdot 10^4 \text{ s}^{-1}$  and  $k_{\text{nr}}(77 \text{ K}) \approx 0 \text{ s}^{-1}$ . These data are summarized in Table 1.1. The significant increase of the radiative rate with increasing temperature shows the involvement of different emitting states, that is, the energetically higher lying singlet state  $S_1$ , emitting fluorescence, and the lower lying triplet state  $T_1$ , emitting phosphorescence. With growing temperature, the singlet state is increasingly populated from the triplet. Obviously, already these properties indicate the occurrence of the TADF effect. In the next section, the electronic properties of the compound will be discussed in more detail.

**Table 1.1:** Emission properties of  $\text{Cu}_2\text{I}_2(\text{P}^\wedge\text{N})_3$  **1** powder at 300 K and 77 K.

	300 K	77 K
Type of emission	TADF and phosphorescence	phosphorescence
$\lambda_{\text{max}} / \text{nm}$	488	488
$\tau / \mu\text{s}$	7	52
$\Phi_{\text{PL}} / \%$	85	$\approx 100$
$k_r / \text{s}^{-1}$ <sup>a</sup>	$12 \cdot 10^4$	$1.9 \cdot 10^4$
$k_{\text{nr}} / \text{s}^{-1}$ <sup>a</sup>	$2.1 \cdot 10^4$	$\approx 0$

<sup>a</sup> The radiative decay rate  $k_r$  and the non-radiative decay rate  $k_{\text{nr}}$  are calculated according to  $k_r = \Phi_{\text{PL}} \tau^{-1}$  and  $k_{\text{nr}} = (1 - \Phi_{\text{PL}}) \tau^{-1}$ , respectively.

## 1.4 Decay dynamics and electronic structure

Deeper insight into the electronic structure of the studied compound can be obtained from an investigation of the decay behavior over a large temperature range, for example,  $1.3 \text{ K} \leq T \leq 300 \text{ K}$ .<sup>100</sup> Although the half-width (FWHM) of the CT emission band at  $T \approx 1.3 \text{ K}$  is as broad as  $\approx 3500 \text{ cm}^{-1}$  (440 meV), this method allows us to get insight into the structure of the electronic states with a resolution of better than  $0.5 \text{ cm}^{-1}$ . Figure 1.4 displays the decay curves at selected temperatures. For  $T > 10 \text{ K}$ , the decay is largely monoexponential. Thus, it can be concluded that at higher temperatures, the states involved are in a fast thermal equilibration, whereby “fast” means that the equilibration processes are much faster than the observed decay times. Clearly, this is not the case below  $T \approx 10 \text{ K}$  for the short time range where relatively slow SLR processes become important (see below).

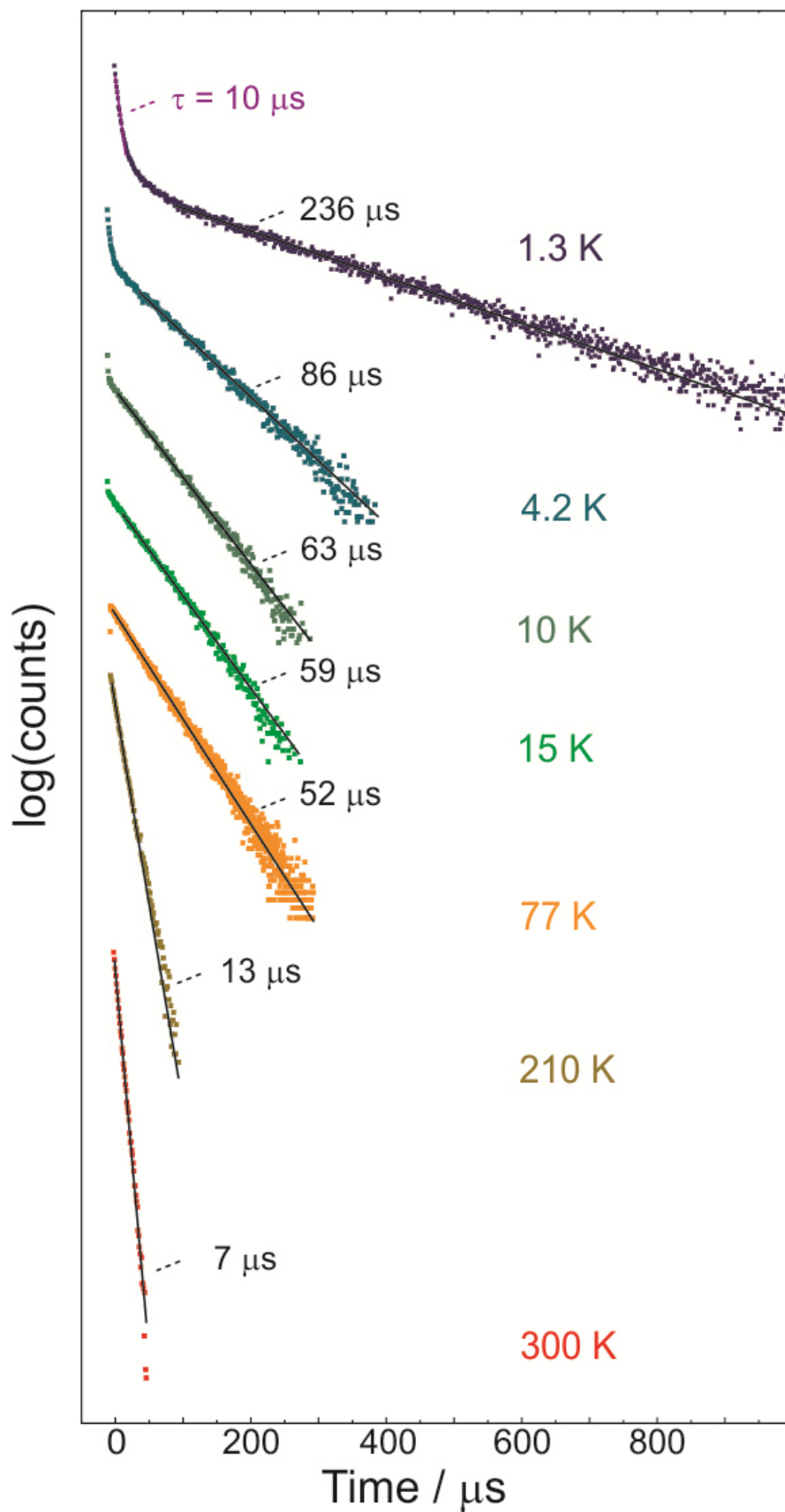


**Figure 1.4:** Emission decay curves and decay times of  $\text{Cu}_2\text{I}_2(\text{PAN})_3$  **1** powder at selected temperatures;  $\lambda_{\text{exc}} = 378 \text{ nm}$ ,  $\lambda_{\text{det}} = 490 \text{ nm}$ , pulse width  $< 100 \text{ ps}$ .

However, if the discussion in this section is restricted to the longer time range (ref. 101, p.194), the temperature dependence of the emission decay time  $\tau(T)$  can be described by a (modified) Boltzmann distribution for a set of four excited states, involving three  $T_1$  substates I, II, and III as well as the  $S_1$  state:<sup>16,17,78,102</sup>

$$\tau(T) = \left[ 1 + e^{-\frac{\Delta E(II-I)}{k_B T}} + e^{-\frac{\Delta E(III-I)}{k_B T}} + e^{-\frac{\Delta E(S_1-T_1)}{k_B T}} \right] \times \left[ k(I) + k(II)e^{-\frac{\Delta E(II-I)}{k_B T}} + k(III)e^{-\frac{\Delta E(III-I)}{k_B T}} + k(S_1)e^{-\frac{\Delta E(S_1-T_1)}{k_B T}} \right]^{-1} \quad (1.1)$$

Herein,  $\Delta E(II-I)$  and  $\Delta E(III-I)$  refer to the energy separations between the  $T_1$  substates I, II, and III representing the ZFS values.  $\Delta E(S_1-T_1)$  is the energy difference between the  $T_1$  and the  $S_1$  states.  $k(I)$ ,  $k(II)$ ,  $k(III)$ , and  $k(S_1)$  are the rates of the  $I \rightarrow S_0$ ,  $II \rightarrow S_0$ ,  $III \rightarrow S_0$ , and  $S_1 \rightarrow S_0$  transitions, respectively.  $k_B$  is the Boltzmann constant.

Figure 1.5 shows a plot of the emission decay time versus temperature. Applying eq. 1.1 to the measured data allows us to determine important decay and ZFS parameters. In the temperature range  $1.3 \text{ K} \leq T \leq 20 \text{ K}$ , a steep decrease of the emission decay time is found with growing temperature. Using eq. (1.1) for the fit to this temperature range,  $\Delta E(I-II) \approx 0$  and for  $\Delta E(III-II, I) \approx 2.5 \text{ cm}^{-1}$  (0.31 meV) is found. The decay rates (and the formally calculated decay times) are  $k(I) + k(II) \approx 4.4 \cdot 10^3 \text{ s}^{-1}$  and  $k(III) \approx 5 \cdot 10^4 \text{ s}^{-1}$  (20  $\mu\text{s}$ ), respectively. The fitting procedure is only successful for an almost zero splitting between substates I and II, that is, the splitting is less than  $1 \text{ cm}^{-1}$  (0.1 meV), presumably  $\ll 1 \text{ cm}^{-1}$ . Such behavior has already been found experimentally<sup>17,35,50,87</sup> and theoretically<sup>103</sup> for other Cu(I) complexes. The fit, however, does not provide information on the individual rates  $k(I)$  and  $k(II)$ . Therefore, only the sum of both rates is given. These data may be used to calculate an average decay time  $\tau_{av}$  that corresponds to the decay time of the triplet state  $T_1$ .<sup>32,104</sup>

$$\tau_{av} = \frac{3}{k(I) + k(II) + k(III)} \quad (1.2)$$

Inserting the obtained values from the fit procedure,  $\tau_{av} = 55 \mu\text{s}$  is obtained. The same decay value is experimentally found for  $T = 50 \text{ K}$ . It lies in the plateau range, as displayed in Figure 1.5. Thus, the steep decrease of the emission decay time with temperature increase in the low-temperature range is a consequence of splitting of the  $T_1$  state into substates and of an increasing population of triplet substate III. This state exhibits a more than 20 times greater decay rate of the transition to the electronic ground state than the two substates I and II (see inset a of Figure 1.5).

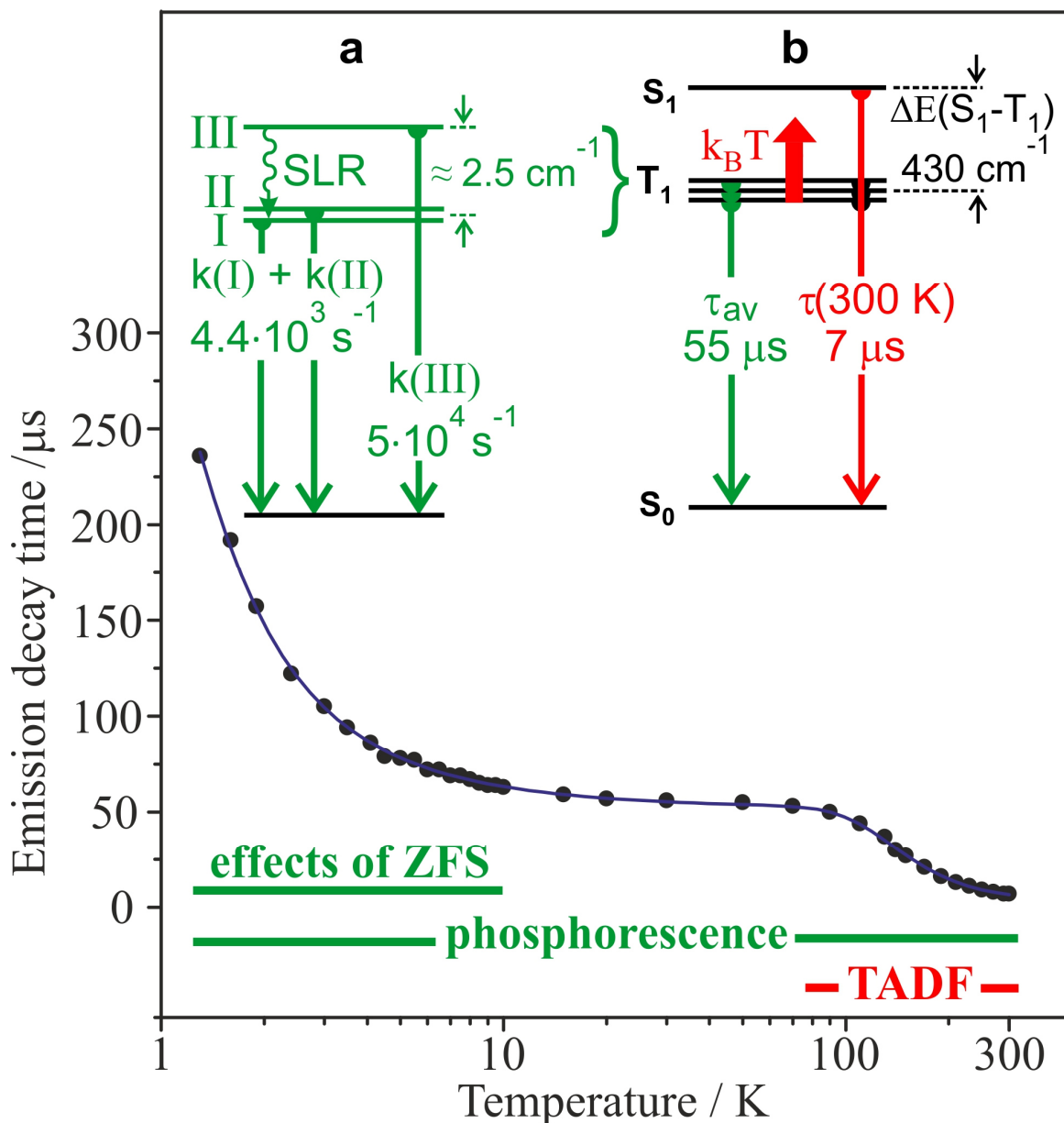


**Figure 1.5:** Temperature dependence of the emission decay time of  $\text{Cu}_2\text{I}_2(\text{P}^{\text{N}})_3$  **1** powder and fit according to eq. (1.1). The insets show energy level diagrams displaying the ZFS of the  $T_1$  state (a) and the singlet-triplet splitting (b) with state-related decay times/ rates. SLR represents spin-lattice relaxation between triplet substate III and the substates II/I. The corresponding SLR time is determined to be  $\tau(\text{SLR}) = 20 \mu\text{s}$  (see below).

When focusing on the temperature range  $\approx 20 \text{ K} \leq T \leq \approx 80 \text{ K}$ , a plateau-like behavior is observed with a decay time of about  $55 \mu\text{s}$ , which is essentially assigned to an average phosphorescence decay related to transitions from the three triplet substates to the ground state. As compared to other Cu(I) complexes, showing, for example, phosphorescence decay times of  $500^{35-37}$  or even  $1200 \mu\text{s}$ ,<sup>36,37,98</sup> the short decay time of  $\approx 55 \mu\text{s}$  indicates relatively efficient SOC of the  $T_1$  state with (a) higher-lying singlet state(s). For the studied compound, SOC induces also distinct ZFS of the  $T_1$  state,

which is not the case for compounds showing long phosphorescence decay times. An important SOC path was already discussed in the theoretical section. (For further details see refs.12, 16, 22 and 37.)

In the temperature range of  $\approx 80 \text{ K} \leq T \leq 300 \text{ K}$ , the emission decay time decreases from near  $55 \mu\text{s}$  (plateau) to  $7 \mu\text{s}$  at ambient temperature (Figure 1.5). This decrease is assigned to the temperature-dependent thermal activation of the  $S_1$  state emission, representing the TADF effect. The fit of eq. (1.1) gives an activation energy of  $\Delta E(S_1 - T_1) = 430 \text{ cm}^{-1}$  (53 meV) (see inset b of Figure 1.5). This represents a relatively small energy separation and relates to the small HOMO-LUMO overlap as resulting from DFT calculations. The value found for  $\text{Cu}_2\text{I}_2(\text{P}^\wedge\text{N})_3$  **1** belongs to the smallest singlet-triplet gaps reported so far for Cu(I) complexes.<sup>34,36,37</sup>

The fit of eq. (1.1) to the experimental data allows us also to determine the rate of the prompt fluorescence  $k(S_1 \rightarrow S_0) = 3.3 \cdot 10^6 \text{ s}^{-1}$  (300 ns). Comparable  $k(S_1 \rightarrow S_0)$  values are also found for other Cu(I) complexes. In refs. 36 and 37 it is shown that these values correlate with the singlet-triplet splitting. That is, a small HOMO-LUMO overlap leads to a small gap between the  $^1\text{CT}(S_1)$  and  $^3\text{CT}(T_1)$  states and to a small transition rate  $k(^1\text{CT}(S_1) \rightarrow S_0)$ . The value of  $k(S_1 \rightarrow S_0) = 3.3 \cdot 10^6 \text{ s}^{-1}$  determined for  $\text{Cu}_2\text{I}_2(\text{P}^\wedge\text{N})_3$  fits well to the relation presented in refs. 36 and 37. For completeness, it is mentioned that a prompt fluorescence is not observed with our experimental time resolution, since the ISC time is too fast (range of several ps<sup>32,85,105</sup>) and largely quenches the prompt fluorescence (but not the TADF emission). The resulting data are summarized in Table 1.2 and in the insets of Figure 1.5.

**Table 1.2:** Transition energies, energy splittings, and emission decay rates of  $\text{Cu}_2\text{I}_2(\text{P}^\wedge\text{N})_3$  **1** powder.

$E_{0-0}(S_1 \rightarrow S_0)$ <sup>a</sup>	$\approx 23800 \text{ cm}^{-1}$ (2.95 eV)
$\Delta E(S_1 - T_1)$	$430 \text{ cm}^{-1}$ (54 meV)
$k(S_1 \rightarrow S_0)$	$3.3 \cdot 10^6 \text{ s}^{-1}$ (300 ns)
$I(T_1) \rightarrow S_0$	} $\approx 23370 \text{ cm}^{-1}$ <sup>b</sup>
$II(T_1) \rightarrow S_0$	
$III(T_1) \rightarrow S_0$	
$k(I) + k(II)$	$\approx 4.4 \cdot 10^3 \text{ s}^{-1}$
$k(III)$	$\approx 5 \cdot 10^4 \text{ s}^{-1}$ (20 $\mu\text{s}$ ) <sup>c</sup>
$\Delta E(II-I)$	$\ll 1 \text{ cm}^{-1}$ (0.1 meV)
$\Delta E(III-I)$	$\approx 2.5 \text{ cm}^{-1}$ (0.31 meV)

<sup>a</sup> Electronic origin (approximately determined from Figure 1.3), <sup>b</sup>  $E_{0-0}(S_1 \rightarrow S_0) - \Delta E(S_1 - T_1)$ , <sup>c</sup> Formal value for the individual decay time constant of  $T_1$  substate III.

## 1.5 Combined TADF and Phosphorescence at ambient Temperature

The emission observed for the studied material at  $T = 300$  K represents a combined emission stemming from the  $T_1$  state as phosphorescence with  $k(T_1 \rightarrow S_0) = (55 \mu\text{s})^{-1}$  and from the  $S_1$  state as TADF emission with  $k(\text{TADF})$ . Such a combined emission can be also observed from a Cu(I) tripod complex studied in chapter 2. The rate can be determined by use of the measured combined rate  $k(\text{comb}) = k(T_1 \rightarrow S_0 + \text{TADF}) = (7 \mu\text{s})^{-1}$  and the phosphorescence rate of  $k(T_1 \rightarrow S_0) = (55 \mu\text{s})^{-1}$

$$k(\text{TADF}) = k(\text{comb}) - k(T_1 \rightarrow S_0) \quad (1.3)$$

Thus, one obtains  $k(\text{TADF}) = (8 \mu\text{s})^{-1}$ . The additionally active process of phosphorescence at  $T = 300$  K reduces the overall decay time by  $\approx 13$  %. Obviously, “tuning in” of a short-lived phosphorescence represents a suitable strategy for obtaining shorter-lived OLED emitters.<sup>78,79</sup> Figure 1.6 summarizes the relevant emission processes in an energy level diagram. According to the equations presented in ref. 50, the emission intensities at  $T = 300$  K stem by 87 % from the  $S_1$  state as TADF and by 13 % as phosphorescence from the  $T_1$  state.

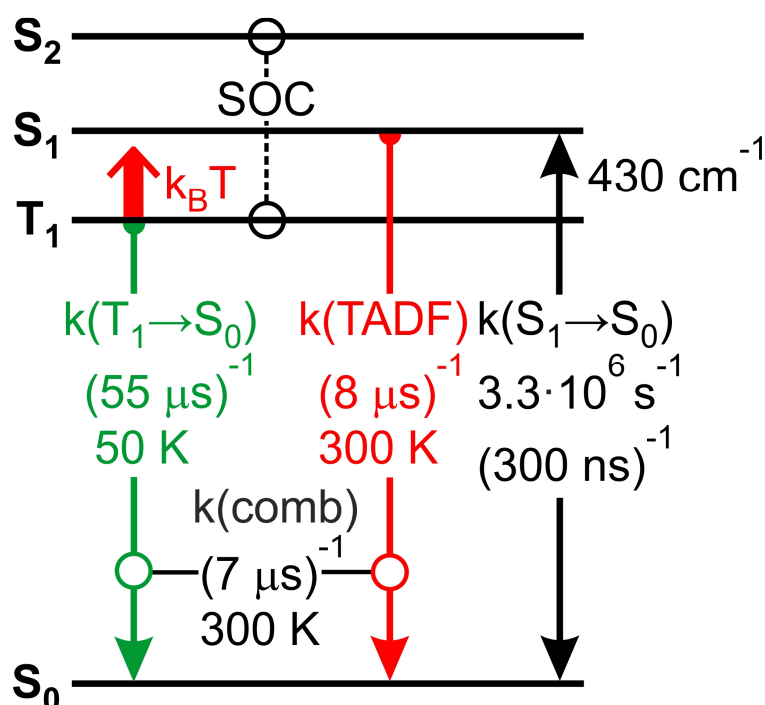


**Figure 1.6:** Simplified energy level diagram and decay times of Cu<sub>2</sub>I<sub>2</sub>(P<sup>^</sup>N)<sub>3</sub> 1 powder. The ambient temperature emission represents combined TADF and phosphorescence. The S<sub>2</sub> state is displayed schematically to illustrate an effective SOC path.

## 1.6 Spin-Lattice Relaxation (SLR) and Zero-field splitting (ZFS)

The occurrence of a distinct ZFS is displayed in the short time range of the emission decay curves below  $T \approx 15$  K. In particular, at 1.3 K a short component of  $\tau(\text{exp}) = 10$   $\mu\text{s}$  is observed in addition to the thermalized long-lived component of 236  $\mu\text{s}$ . (Figure 1.4) The occurrence of the short-lived component is related to a relatively slow and, thus, easily observable thermalization between the three triplet substates I, II, and III at low temperature showing small energy separation(s) of a few  $\text{cm}^{-1}$ . Such effects of SLR have already been investigated thoroughly for Ru(II) and Pt(II) complexes,<sup>32,101,106,107</sup> but barely for Cu(I) complexes. SLR mechanisms are strongly temperature dependent and may be characterized by the *direct*, *Raman*, and/ or *Orbach* mechanism.<sup>32,101,106-112</sup> However, at very low temperature, only the direct process of SLR is of importance, whereby the corresponding rate  $k(\text{direct})$  is only very weakly temperature dependent and may be approximated by<sup>32,101,106</sup>

$$k(\text{direct}) \approx \text{const} \cdot \Delta E^3 \quad (1.4)$$

wherein  $\Delta E$  is the energy distance between two electronic energy states separated by a few  $\text{cm}^{-1}$  (a few 0.1 meV). The constant depends on material properties of the matrix and coupling of the involved states with the environment. Thus, for  $\text{Cu}_2\text{I}_2(\text{P}^\wedge\text{N})_3 \mathbf{1}$ , the rate of SLR between the triplet substates II and I with an energy splitting of  $\Delta E(\text{II} - \text{I}) \ll 1 \text{ cm}^{-1}$  is negligibly small. However, the rate (time) for the relaxation from substate III to the substates II and I according to the *direct* process can be determined. The experimentally available decay rate at  $T = 1.3$  K (Figure 1.4) of  $k(\text{exp}) = (\tau(\text{exp}))^{-1} = (10 \mu\text{s})^{-1}$  is related to the SLR rate according to<sup>32</sup>

$$k(\text{direct}) = k(\text{exp}) - k(\text{III} \rightarrow \text{S}_0) \quad (1.5)$$

wherein  $k(\text{III} \rightarrow \text{S}_0)$  represents the rate of the transition from triplet substate III to the electronic ground state  $\text{S}_0$  and has been determined by the fitting procedure to  $(20 \mu\text{s})^{-1}$ . (Figure 1.5, inset a) Accordingly, for the SLR time a value of  $\tau(\text{SLR}) = (k(\text{direct}))^{-1} = 20 \mu\text{s}$  is obtained. This is the relaxation time from triplet substate III to the two substates II and I. In Figure 1.7, the  $T_1$  energy level diagram and the relevant relaxation paths and times are summarized.

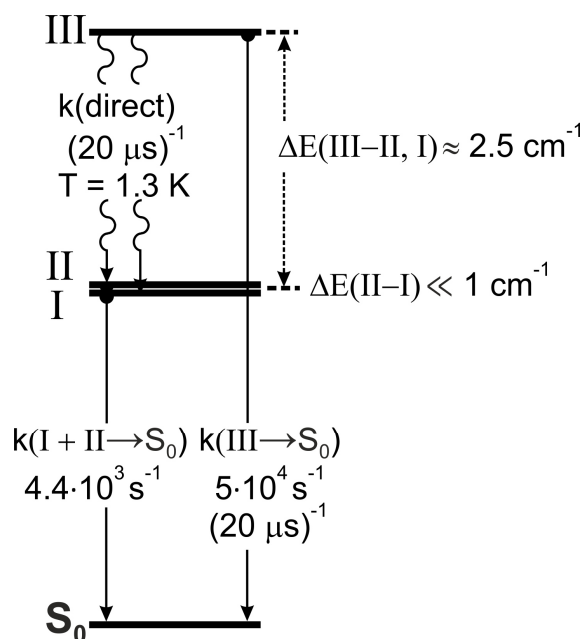


**Figure 1.7:** Energy level diagram for the  ${}^3\text{CT}(\text{T}_1)$  state and relaxation data for  $\text{Cu}_2\text{I}_2(\text{P}^\wedge\text{N})_3 \mathbf{1}$  powder. The values result from a fit of eq.(1.1) to the decay plot according to Figure 1.5 and are calculated from the short decay component measured at 1.3 K (Figure 1.4).

The magnitude of the ZFS can independently and roughly be estimated just from the SLR time as determined to be  $\tau(\text{SLR}) \approx 20 \mu\text{s}$ . For such an estimate, it is assumed that the constant in eq.(1.4) is approximately similar for different compounds. For example, for  $\text{Pt}(\text{2-thpy})_2$  (with  $\text{2-thpy}^- = 2\text{-(2-thienyl)-pyridinate}$ ) dissolved in an *n*-octane matrix, Yersin et al. determined from highly resolved spectra an energy separation between two triplet substates of  $7 \text{ cm}^{-1}$  and a SLR time of 720 ns at  $T = 1.3 \text{ K}$ .<sup>32</sup> With these values and applying eq.(1.4), the expected ZFS for a compound showing  $\tau(\text{SLR}) \approx 20 \mu\text{s}$  can be easily calculated. Interestingly, by this rough estimate one obtains  $\Delta E = 2.3 \text{ cm}^{-1}$ . This is almost the same splitting as found for  $\text{Cu}_2\text{I}_2(\text{P}^\wedge\text{N})_3 \mathbf{1}$  from the fitting procedure as displayed in Figure 1.5. Apparently, this accordance represents a nice confirmation of the model described above. In conclusion, for an interpretation of the SLR effects measured below  $T \approx 10 \text{ K}$ , it is crucial to take the results from a successful fitting procedure into account, as presented in Figure 1.5. In particular, the ZFS energy of  $\Delta E(\text{III-II,I}) \approx 2.5 \text{ cm}^{-1}$  will lead to an additional decay component that results from the direct effect of SLR (compare refs. 78, 87 and 106). This component cannot be mixed up with individual decay components of the triplet substates, as observed frequently. The individual components may be used to calculate an average decay time (according to eq. 1.2). This calculated value will usually fit to the measured decay time in the plateau range (compare refs. 35, 50, 107, 113 and 114), while the SLR decay time does not fulfill this condition (compare refs. 78, 87 and 106). This is also the case for the  $10 \mu\text{s}$  SLR decay component observed for  $\text{Cu}_2\text{I}_2(\text{P}^\wedge\text{N})_3 \mathbf{1}$  at  $T = 1.3 \text{ K}$  (Figure 1.4).

## 1.7 Conclusion

The studied dinuclear Cu(I) complex  $\text{Cu}_2\text{I}_2(\text{P}^\wedge\text{N})_3$  **1** is characterized by a rigid molecular structure due to the three-fold bridging between the Cu(I) centers. Hence, the photoluminescence quantum yield is as high as  $\Phi_{\text{PL}} = 85\%$  at  $T = 300\text{ K}$  for the powder material. It shows a sky-blue CT emission peaking at  $\lambda_{\text{max}} = 488\text{ nm}$ . The triplet state exhibits distinct admixtures of higher-lying singlet state(s) due to SOC. As a consequence, a relatively fast phosphorescence decay rate is observed. Thus, the ambient-temperature emission represents a combined phosphorescence (13 %) and TADF (87 %) luminescence. Accordingly, the overall decay time is reduced by about 13 % compared to the TADF-only situation (8  $\mu\text{s}$ ) and becomes as short as 7  $\mu\text{s}$ . In general, mechanisms that help to decrease the population time of the excited states are highly requested for OLED applications mainly to reduce stability problems. Moreover, because the studied complex is very soluble in many organic solvents, such as toluene and dichloromethane, the material represents an attractive candidate to be applied as an emitter for solution-processed OLEDs.

For future material improvements and new design strategies, it is essential to learn more about the electronic structures of emitter materials.

Accordingly, the focus is on details of the triplet state properties that are of particular interest due to the significance of SOC. Thus, as compared to most other Cu(I) complexes,<sup>35-37,98</sup>  $\text{Cu}_2\text{I}_2(\text{P}^\wedge\text{N})_3$  **1** shows a relatively large ZFS of the  $T_1$  state into triplet substates by  $\Delta E \approx 2.5\text{ cm}^{-1}$ . Such a splitting is connected to specific emission decay properties at low temperature induced by relatively slow SLR. Corresponding photophysical properties are elucidated here in detail for the first time for Cu(I) complexes. These deeper studies might lead to future material improvements, in particular, with respect to a larger involvement of the triplet state to induce a combined *singlet harvesting* emission (via TADF) and *triplet harvesting* emission (via phosphorescence). Maybe the detailed photophysical investigations will guide us to a next-generation OLED mechanism also with Cu(I) compounds, similarly as recently designed for purely organic emitter molecules by developing the *direct singlet harvesting* (DSH) mechanism.<sup>115-117</sup> For such emitter molecules, the overall emission decay time can be reduced even to the sub- $\mu\text{s}$  range.

## 2 Deep blue Cu(I) tripod complexes – increase of quantum yield by tuning sterical hindrance

This chapter was published recently in ref. 59. In this chapter, the focus is on a special class of Cu(I) complexes built with a tri-dentate tpym (tpym = tris(2-pyridyl)methane) and a mono-dentate triphenylphosphine ligand that coordinate to the Cu(I) center. The chemical structures of the complexes studied here are shown in Figure 2.1. Compound **2** was already presented in a previous paper.<sup>47</sup> It reveals remarkable properties. For example, it shows deep blue emission ( $\lambda_{\max}(300\text{ K}) = 466\text{ nm}$ ) and a phosphorescence decay time of only  $26\ \mu\text{s}$  (at  $T = 77\text{ K}$ ), which is unusually short compared to other Cu(I) complexes.<sup>34-37,40,41,44-47,49-51,53,56-58,98</sup> However, the emission quantum yield of compound **2** at ambient temperature is relatively low depending on the environment ( $\Phi_{\text{PL}}$ : powder: 43 %, PMMA doped: 7 %, dissolved in dichloromethane (DCM):  $\ll 1\%$ ). Thus, the compound is not attractive as an OLED emitter. Moreover, the dominating nonradiative quenching and its temperature variation do not allow the characterization of the electronic structure of this compound by straightforward investigations. Therefore, it was decided to design related complexes that exhibit higher emission quantum yields. These investigations were carried out after density functional theory (DFT) and time dependent DFT (TD-DFT) calculations, by which it was possible to identify specific and distinct geometry distortions that occur after electronic excitation. Usually, such distortions are responsible for large Franck-Condon factors that are responsible for nonradiative relaxations.<sup>94</sup> These studies led to the proposal of the structures **3** and **4**, in which the identified distortions are strongly reduced by introducing sterical hindrances, such as *ortho* methyl and *n*-butyl substitutions, respectively, to the aryl groups of the phosphine ligand (Figure 2.1).

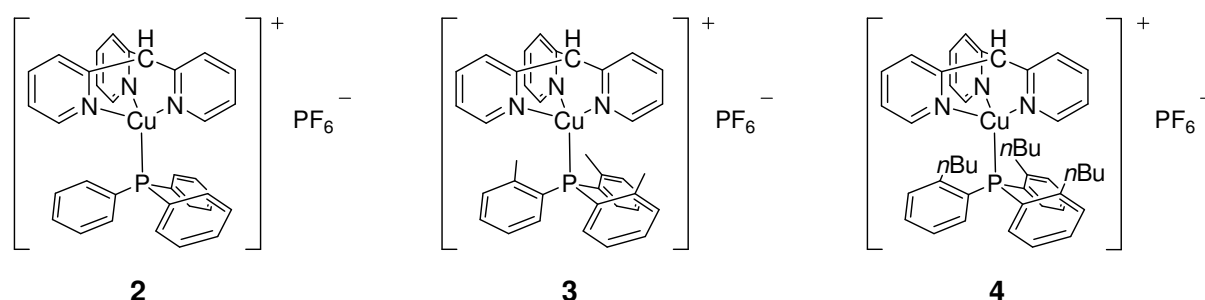


**Figure 2.1:** Structures of [Cu(tpym)(PPh<sub>3</sub>)]PF<sub>6</sub> **2**, [Cu(tpym)(P(*o*-tol)<sub>3</sub>)]PF<sub>6</sub> **3** and [Cu(tpym)(P(*o*-butyl-ph)<sub>3</sub>)]PF<sub>6</sub> **4** (Figure 2.1 was provided by Dr. Nicholas Rau<sup>59</sup>).

This design strategy is highly successful with respect to the ambient-temperature emission quantum yield. For compound **4** dissolved in a fluid medium, it can be enhanced up to 76 %. This is an increase by more than three orders of magnitude as compared to compound **2** dissolved in DCM. Interestingly, this high emission quantum

yield represents the highest value reported for dissolved Cu(I) complexes at publication date. Also the emission quantum yield of the powder samples can be tuned to significantly higher values without losing the deep blue emission color observed for compound **2**. With this success in hand, it was possible to characterize the electronic structure of this type of material in detail. Moreover, it will be shown that these complexes, show an even higher contribution of phosphorescence to the overall emission at ambient temperature than compound **1** (see chapter 1). The total emission consists of  $\approx 60\%$  phosphorescence combined with  $\approx 40\%$  TADF. Hence, the material, if applied in an OLED, stands for a *triplet harvesting-plus-singlet harvesting* situation.

## 2.1 Synthesis and structural characterization

Guided by the computational results (see below), Dr. Nicholas Rau<sup>59</sup> prepared and chemically characterized the compounds **3** (including X-ray structure determination) and **4** both shown in Figure 2.1.

The X-ray structure of the model compound **3** is shown in Figure 2.2. Detailed X-ray data of complex **2** and **3** can be found in SI of ref. 59.

For both compounds **3** and **2**, the Cu(I) center is coordinated by the three N atoms of tpym with Cu-N bond distances between 2.047 and 2.080 Å. These values are not remarkable if compared to other tripod complexes.<sup>46,47</sup> The Cu-P bond length is slightly longer for **3** (2.167 Å) than for **2** (2.160 Å). Presumably, this is a consequence of the sterical demand of the methyl groups. Of particular interest is the P-Cu-C16 angle. In the electronic ground state, it is not very different for both compounds (**2**: 177.6°, **3**: 178.1°). But it will be shown below that this angle changes strongly, but differently, after excitation.

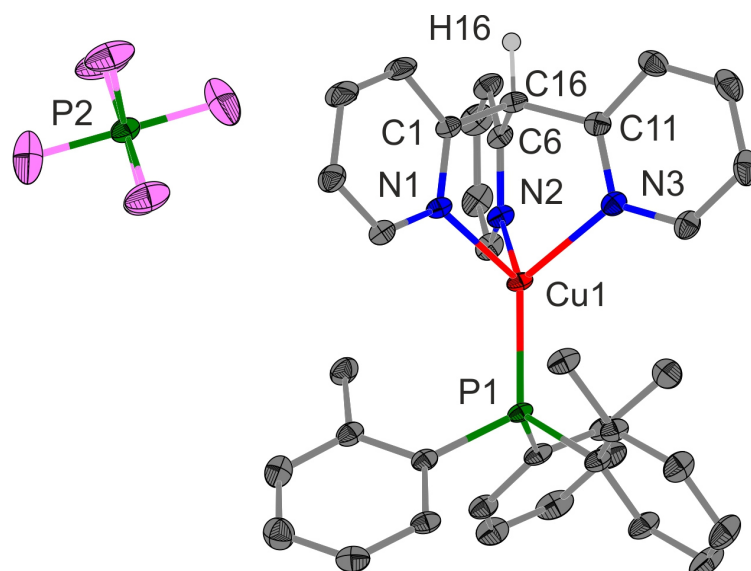


**Figure 2.2:** Molecular structures of  $[\text{Cu}(\text{tpym})(\text{P}(\textit{o}\text{-tol})_3)]\text{PF}_6$  **3** (thermal ellipsoids with 50 % probability) determined by X-ray diffractometry. Hydrogen atoms (except H16) as well as solvent molecules are omitted for clarity (for further details see table S-1 of SI of ref. 59). (X-ray crystal structure and data was provided by Dr. Nicholas Rau<sup>59</sup>)

## 2.2 Computational studies

The theoretical investigations were performed in the scope of density functional theory (DFT) and time-dependent density functional theory (TD-DFT) at the B3LYP/def2-SVP level of theory<sup>80,81</sup> using the NWChem 6.6 code.<sup>82</sup> For all three compounds gas phase optimizations of the electronic ground state  $S_0$  and first excited triplet state  $T_1$  were carried out. For compound **2**, the results agree well with those reported earlier.<sup>47</sup> The calculated ground state structure data of **2** and **3** agree well with those of the X-ray structure determinations. (Compare data of Table S-5 and S-6 with those of Table S-2 in SI of ref. 59.)

Of special interest are the geometry changes upon excitation of the  $T_1$  state as compared to the electronic ground state  $S_0$ . It is well known that pseudo-tetrahedrally coordinated Cu(I) and Ag(I) complexes undergo significant flattening distortions towards a planar geometry, if the corresponding electronic excitation represents a metal-to-ligand charge transfer (MLCT) transition.<sup>34-37,39,40,42-47,49,50,53,61,85,86,88</sup> For the complexes studied, the calculations predict and the experimental investigations show, that the lowest excited states are also of  $^1,^3\text{MLCT}$  character (see below). However, for the Cu(I) complexes with relatively rigid tripodal ligands and sterically demanding coligands such as substituted phosphines, a typical flattening distortion upon excitation is not expected to occur. The molecule reacts with a significant reduction of the P-Cu-C16 bending angle, apart from a number of less distinct reorganizations. For

compound **2** the change is as large as  $\approx 25^\circ$  (from  $179.6^\circ$  to  $155.0^\circ$ ), while for compounds **3** and **4**, the angle change is much smaller and amounts only to  $\approx 16^\circ$ . Obviously, this is related to the steric demand of the *ortho* methyl and *n*-butyl aryl phosphine substituents, respectively. Motivated by this theoretical design approach, Dr. Nicholas Rau synthesized the complexes **3** and **4** in order to obtain higher emission quantum yields than found for complex **2**.

The main interest lies in emission properties. Therefore, the calculations were done for the  $T_1$  state geometry of compound **3** (The  $S_1$  state has a very similar geometry as is shown in Table S-6 of the SI of ref. 59). Both states,  $T_1$  and  $S_1$ , are of 94.4 % and 97.1 % of HOMO  $\rightarrow$  LUMO character, respectively. Figure 2.3 displays the iso-contour plots of the frontier orbitals for **3** as a representative example. While the HOMO is largely characterized by a d-orbital of the Cu center, the LUMO is essentially distributed over the tpym ligand. Accordingly, both states  $T_1$  and  $S_1$ , can be assigned to  $^1MLCT$  and  $^3MLCT$ , respectively.

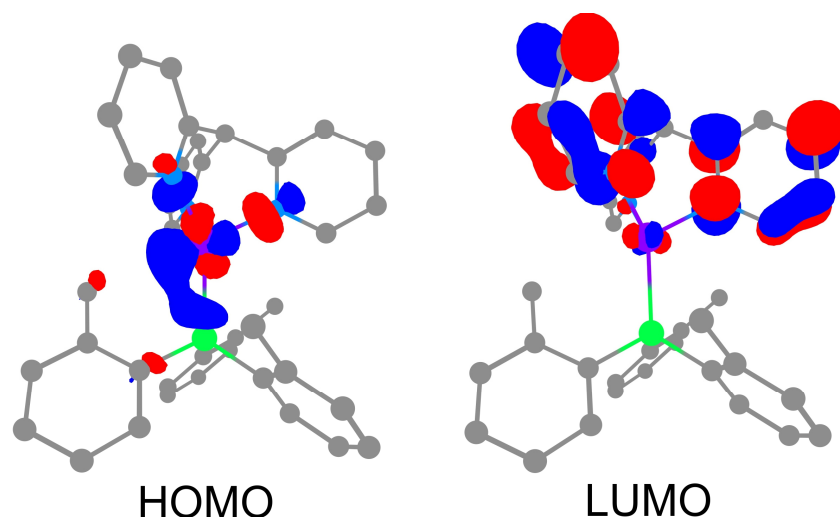


**Figure 2.3:** Iso-contour plots of the highest occupied (HOMO) and lowest unoccupied molecular orbital (LUMO) of  $[\text{Cu}(\text{tpym})(\text{P}(o\text{-tol})_3)]^+$  **3** calculated for the optimized  $T_1$  state geometry (isovalue = 0.05). Calculations were performed at the B3LYP/def2-SVP level of theory. All hydrogen atoms are omitted for clarity. The HOMO and LUMO correspond largely to “hole” and “electron” of natural transition orbitals, respectively, for both transitions  $S_0 \rightarrow T_1$  and  $S_0 \rightarrow S_1$ .

The spatial separation of the orbital distributions shown in Figure 2.3 indicates the occurrence of a small exchange interaction between the unpaired electrons.<sup>95,96</sup> Hence, a relatively small  $\Delta E(S_1-T_1)$  value is expected.<sup>34-37,39,41-44,46,47,49,50,53,60-62,98</sup> The calculations give a splitting value of  $\approx 1400 \text{ cm}^{-1}$  (174 meV) for the energy separation of the vertical transitions. The amount of this value indicates that the compound might exhibit TADF. Below it will be shown that the experimental value amounts to  $\Delta E(S_1-T_1) = 900 \text{ cm}^{-1}$  (112 meV).

## 2.3 Quantum yield design. Steric demands and host rigidity

Based on the results of DFT and TD-DFT calculations, in particular, comparing the calculated excited state geometry variations of  $[\text{Cu}(\text{tpym})(\text{PPh}_3)]\text{PF}_6$  **2** with those of  $[\text{Cu}(\text{tpym})(\text{P}(o\text{-tol})_3)]\text{PF}_6$  **3** and  $[\text{Cu}(\text{tpym})(\text{P}(o\text{-butyl-ph})_3)]\text{PF}_6$  **4**, the compounds were synthesized and the emission quantum yields measured. Characteristic trends are observed as displayed in Table 2.1. Most simply, the trend of quantum yield increase is explained for the compounds dissolved in DCM. Complex **2** undergoes very distinct geometry distortions in the fluid environment after electronic excitation. In this situation, the molecule exhibits a good overlap of the energetically higher lying vibrational wave functions of the electronic ground state  $S_0$  with lower lying ones of the excited state. Thus, large Franck-Condon (FC) factors result that govern the rates of nonradiative processes; see also references. 36, 37, 49, 52, 60, 61 and 94 As a consequence, nonradiative deactivation leads to emission quenching. With increasing sterical hindrance from **2** to **3** and finally to **4**, the FC factors become smaller. Thus, the quantum yield grows in drastically, reaching the highest  $\Phi_{\text{PL}}$  value found (at the date of publication) for Cu(I) complexes dissolved in fluid environments at ambient temperature (Compare to ref. 57, later even a higher  $\Phi_{\text{PL}}$  value was reported<sup>118</sup>.) Very likely, the reduction of the change of the P-Cu-C16 bending angle upon excitation from  $\approx 25^\circ$  for complex **2** to  $\approx 16^\circ$  for **3** and **4** and the related increase of the molecular rigidity are dominantly responsible for the quantum yield increase. Other less important excitation-induced geometry changes are also reduced or suppressed (compare Table S-4 in SI of ref. 59). This is seen, when the quantum yields  $\Phi_{\text{PL}}$  of **3** and **4** dissolved in DCM are compared.  $\Phi_{\text{PL}}$  is distinctly higher for the more rigid compound **4** than that for **3**. (Table 2.1) In this chapter, however, not all related distortion modes are specified.

**Table 2.1:** Emission quantum yields and peak maxima at  $T = 300$  K for the compounds studied in different environments

Matrix		$[\text{Cu}(\text{tpym})(\text{PPh}_3)]\text{PF}_6^{\text{a}}$	$[\text{Cu}(\text{tpym})(\text{P}(o\text{-tol})_3)]\text{PF}_6$	$[\text{Cu}(\text{tpym})(\text{P}(o\text{-butyl-ph})_3)]\text{PF}_6$
		<b>2</b>	<b>3</b>	<b>4</b>
powder	$\lambda_{\text{max}}$	466 nm	458 nm	452 nm
	$\Phi_{\text{PL}}$	43 %	86 %	56 %
PMMA	$\lambda_{\text{max}}$	470 nm	466 nm	467 nm
	$\Phi_{\text{PL}}$	7 %	75 %	70 %
DCM <sup>b</sup>	$\lambda_{\text{max}}$	– <sup>c</sup>	488 nm	488 nm
	$\Phi_{\text{PL}}$	$\ll 1$ %	58 %	76 %

<sup>a</sup> Compare ref. 47; <sup>b</sup> DCM = dichloromethane; <sup>c</sup> Could not be measured

For the compounds doped in PMMA, higher quantum yields than in fluid solutions (Table 2.1) are found, because the more rigid host suppresses part of the possible geometry changes. This is even more obvious for very rigid crystalline (powder) matrices.

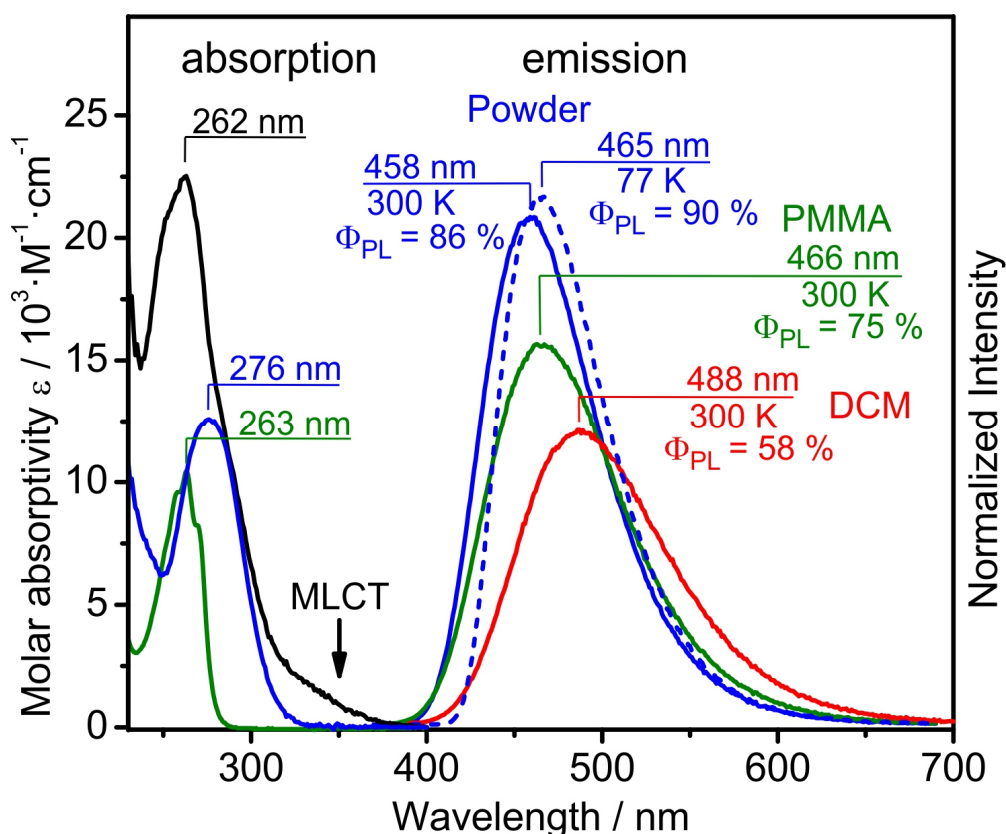
At first sight, the described trend found for the powder materials **2** and **3** does not seem to be valid, if compound **4** is also taken into account. Its emission quantum yield decreases for the powder as compared to the less rigid molecules **2** and **3**. Interestingly, this is a very rare situation for Cu(I) or Ag(I) compounds that exhibit low-lying  $^1,^3$ MLCT states. For these, usually much larger quantum yields are found for powder materials than for compounds dissolved in fluid solutions.<sup>17,35-37,49,53,60-62</sup> This behavior is related to the relatively rigid crystalline environments. Nevertheless, even in these rigid cages, some geometry distortions in the excited  $^1,^3$ MLCT states can still occur. For powder materials of Cu(I) and Ag(I) complexes, these distortions and the related energy stabilizations are usually large enough to tune-off the resonance conditions for energy transfer to adjacent non-excited molecules.<sup>17,35-37,50</sup> Accordingly, the excitation is trapped at the initially excited molecule. As a consequence, such powder samples can be applied to investigate the emission properties of individual complexes that are located in the neat material. The occurrence of such self-trapping effects<sup>119,120</sup> represents a condition for successful measurements, in particular, of the temperature-dependence of the emission decay time, as presented below and in other studies.<sup>34-37,49,50,52,53,60-62,64,98</sup> For compound **4**, the situation is, however, different. Due to the distinct molecular-based rigidity combined with the matrix-dependent rigidity, the self-trapping effect is (partly) suppressed. As a consequence, excitation energy migration and the related concentration quenching can occur. Hence, the quantum yield of **4** is smaller for the powder material than for the diluted fluid solution.

Table 2.1 reproduces also the positions of the emission maxima. Clear trends of red shifts are observed, (i) with decreasing rigidity of the host from powder to DCM and (ii) with decreasing molecular-based rigidity from **4** to **2**. This behavior is easily explained by the extent of the geometry change upon excitation as described above. The geometry change leads to a specific energy stabilization and, hence, to a related red shift of the emission bands. However, changes of the host polarity will also have an influence on the energy of the  $^1,^3$ MLCT emissions, but discussions of these influences are not in the scope of this investigation, but see ref. 69.

All these compounds studied show a similar importance of the  $T_1 \rightarrow S_0$  phosphorescence for the whole temperature range investigated (see below and Table S-22 of ref. 59). Thus, in the subsequent sections, mainly [Cu(tpym)(P(*o*-tol)<sub>3</sub>)]PF<sub>6</sub> **3** will be studied. Focusing on **3** is also advised, because a detailed elucidation of the electronic properties of the compounds **2** and **4** is not straightforward due to the distinct temperature dependences of the nonradiative rate and the concentration quenching effects, respectively.

## 2.4 Absorption and emission spectra

Figure 2.4 reproduces the absorption and emission spectra of compound **3**. The absorption spectra of **2**<sup>47</sup> and **4** are very similar. Intense absorptions are found below  $\approx 300$  nm. They are assigned to  $\pi \rightarrow \pi^*$  transitions within the ligands, as is substantiated by a comparison with the spectra of the pure ligands, tpym and P(*o*-tol)<sub>3</sub>, also displayed in Figure 1.4. A weaker, unstructured absorption band between about 300 and 380 nm is only observed for the complex. It is assigned to  $S_0 \rightarrow {}^1\text{MLCT}$  transition(s).



**Figure 2.4:** Absorption spectra of [Cu(tpym)(P(*o*-tol)<sub>3</sub>)]PF<sub>6</sub> **3** (black), tpym (green), and triphenylphosphine ligand (blue) measured in dichloromethane (DCM) at  $c \approx 10^{-5}$  M ( $T = 300$  K). Emission spectra of the powder (blue) measured at  $T = 300$  K and 77 K, respectively, and doped in PMMA (green) ( $\approx 1$  w%) at  $T = 300$  K as well as in degassed DCM solution (red) ( $c \approx 10^{-5}$  M). Excitation wavelength  $\lambda_{\text{exc}} = 350$  nm.

Emission spectra of compound **3** powder, measured at  $T = 77$  K and 300 K, respectively, are also reproduced in Figure 2.4. The spectral bands are broad with halfwidths of  $\approx 3600$   $\text{cm}^{-1}$  (450 meV). No better spectral resolution could be obtained even if cooled to  $T = 1.5$  K. This behavior is related to MLCT type of electronic transitions, which usually lead to broad bands. At  $T = 77$  K, the emission band peaks at  $\lambda = 465$  nm. This transition showing a decay time of 21  $\mu\text{s}$  is assigned to  ${}^3\text{MLCT}$

( $T_1$ )  $\rightarrow$   $S_0$  phosphorescence as will be substantiated below. With the temperature increase, an energetically higher lying emission band stemming from the  $^1MLCT$  ( $S_1$ ) state is thermally activated and a TADF band grows in. However, due to the high phosphorescence radiative rate (short decay time), both phosphorescence and TADF overlap at ambient temperature. Thus, essentially a blue shift of the high-energy flank occurs. Therefore, the related blue shift of the peak maximum amounts only to 7 nm ( $330\text{ cm}^{-1}$ , 41 meV). Obviously, this shift does not display the energy gap  $\Delta E(S_1 - T_1)$  as frequently found for other Cu(I) TADF compounds.<sup>17,34-37,49</sup> In the next section, it will be shown that the corresponding activation energy  $\Delta E(S_1 - T_1)$  can be determined to be  $900\text{ cm}^{-1}$  (112 meV) by temperature dependent studies of the emission decay dynamics.

A summary of emission data of all three compounds  $[Cu(tpym)(PPh_3)]PF_6$  **2**,  $[Cu(tpym)(P(o\text{-tol})_3)]PF_6$  **3**, and  $[Cu(tpym)(P(o\text{-butyl-ph})_3)]PF_6$  **4** is found in the SI of ref. 59 (Table S-22).

## 2.5 Detailed electronic structure of $[Cu(tpym)(P(o\text{-tol})_3)]PF_6$ **3**

A deeper understanding of electronic structures is frequently gained from an analysis of the emission decay time over a large temperature range, for example, of  $1.5\text{ K} \leq T \leq 300\text{ K}$ .<sup>36,37,49,53</sup> Again, the focus is on compound **3**. The emission decay behavior is largely mono-exponential in the investigated temperature range, indicating that the equilibration processes between the emitting states are much faster than the emission times. Consequently, the variation of the decay time with temperature  $\tau(T)$  can be described by a modified Boltzmann distribution. For compound **3**, four excited energy states have to be taken into account, consisting of the three  $T_1$  substates I, II, and III as well as the lowest excited  $S_1$  state. This leads to eq.(2.1):<sup>16,17,36,78,102</sup> (Compare also ref. 121.)

$$\tau(T) = \left[ 1 + e^{-\frac{\Delta E(II-I)}{k_B T}} + e^{-\frac{\Delta E(III-I)}{k_B T}} + e^{-\frac{\Delta E(S_1-I)}{k_B T}} \right] \times \left[ k(I) + k(II)e^{-\frac{\Delta E(II-I)}{k_B T}} + k(III)e^{-\frac{\Delta E(III-I)}{k_B T}} + k(S_1)e^{-\frac{\Delta E(S_1-I)}{k_B T}} \right]^{-1} \quad (2.1)$$

Herein,  $\Delta E(II-I)$ ,  $\Delta E(III-I)$ , and  $\Delta E(S_1-I) \approx \Delta E(S_1 - T_1)$  are the energy separations between the  $T_1$  substates I, II, III and the energy difference between the  $T_1$  state (average energy of the three substates) and the  $S_1$  state.  $k(I)$ ,  $k(II)$ ,  $k(III)$ , and  $k(S_1)$  represent the corresponding transition rates to the electronic ground state  $S_0$ .  $k_B$  is the Boltzmann constant.

As shown in Figure 2.5, fitting of eq.(2.1) to the measured data is successful over the complete temperature range. For  $1.5 \text{ K} \leq T \leq 30 \text{ K}$ , information on the  $T_1$  substates and the transition rates to the electronic ground state are obtained. At a very low temperature ( $T \leq 1.5 \text{ K}$ ), a first plateau is seen with a decay time of  $\approx 290 \mu\text{s}$ . It refers to the emission from the lowest triplet substates I and II. Under assumption of thermal equilibration and with substate III emission being frozen out, a joint transition rate of  $k(\text{I}) + k(\text{II}) \approx 2/(290 \mu\text{s}) \approx 6.8 \cdot 10^3 \text{ s}^{-1}$  (Note, the factor 2 results from the two thermally equilibrated states, compare eq. 2.2.) With temperature increase, a drop of the decay time to a second plateau, found for the range of  $30 \text{ K} \leq T \leq 160 \text{ K}$ , is observed. This plateau is characterized by a decay time of  $\approx 20 \mu\text{s}$ . The drop is related to a population of triplet substate III that exhibits a significantly faster transition rate than  $k(\text{I}) + k(\text{II})$ . The fitting procedure leads to the following data for the  $T_1$  state:  $k(\text{I}) + k(\text{II}) \approx 6.8 \cdot 10^3 \text{ s}^{-1}$  (first plateau) and  $k(\text{III}) \approx 1.4 \cdot 10^5 \text{ s}^{-1}$  ( $7 \mu\text{s}$ ) (second plateau). Thus,  $k(\text{III})$  is faster than  $k(\text{I}) + k(\text{II})$  by more than a factor 20. A splitting of the substates I and II is not observed. Therefore, and in analogy to several other Cu(I) complexes<sup>17,35,36,50,53,87</sup>, a splitting of  $\Delta E(\text{II-I}) < 0.5 \text{ cm}^{-1}$  (presumably  $\ll 0.5 \text{ cm}^{-1}$ ) is assumed. For  $\Delta E(\text{III-II, I})$ , representing the total zero-field splitting (ZFS),  $7 \text{ cm}^{-1}$  ( $0.87 \text{ meV}$ ) is obtained. The average decay time of  $T_1$  can be expressed by<sup>32,104</sup>

$$\tau_{av} = \frac{3}{k(\text{I}) + k(\text{II}) + k(\text{III})} \quad (2.2)$$

Inserting the fit values obtained for the rates of the substate transitions to the electronic ground state,  $\tau(T_1) = 20.4 \mu\text{s}$  is found. This value fits well to the emission decay time of the plateau of  $\tau(T_1) = 21 \mu\text{s}$  (measured at  $T = 77 \text{ K}$  (at  $\Phi_{\text{PL}}(77 \text{ K}) = 90 \%$ )).

This  $T_1 \rightarrow S_0$  decay time belongs to the shortest values found for Cu(I) complexes investigated so far.<sup>36,46,47,51,87</sup> Most Cu(I) complexes exhibit significantly longer decays, for example, of several hundred  $\mu\text{s}$ .<sup>34-37,49</sup> Obviously, substate III experiences distinct SOC to (a) higher lying singlet state(s), while mixing with higher lying triplet(s) seems to be responsible for the relatively large ZFS of  $7 \text{ cm}^{-1}$ , as compared to other Cu(I) complexes.

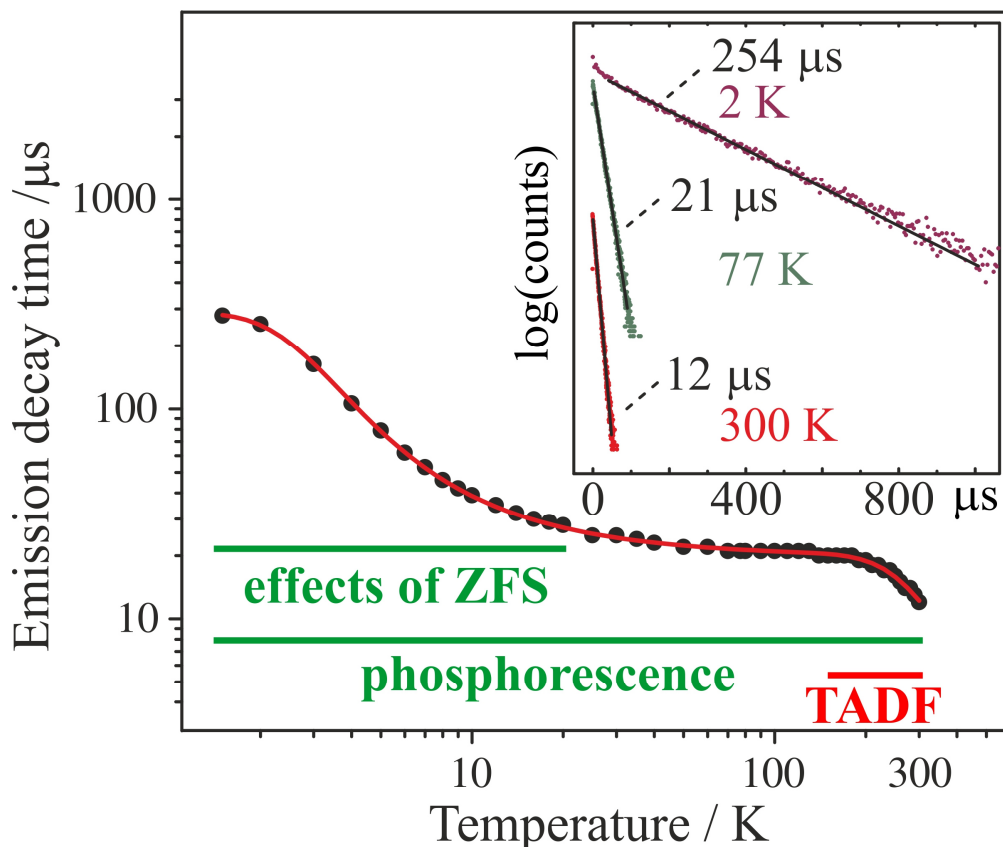


**Figure 2.5:** Emission decay time versus temperature measured for a powder sample of compound  $[\text{Cu}(\text{tpym})(\text{P}(o\text{-tol})_3)]\text{PF}_6$  **3**. The red line represents a fit to the data according to equation (2.1). In the inset, emission decay curves at selected temperatures are depicted. ( $\lambda_{\text{exc}} = 378$  nm and  $\lambda_{\text{det}} = 465$  nm)

With further temperature increase from  $T \approx 160$  K to 300 K, the emission decay time decreases to  $\tau(300 \text{ K}) = 12 \mu\text{s}$ . (Figure 2.5) In this temperature range, an additional decay path with higher allowedness is opened, representing the TADF path. The fitting procedure allows the determination of  $\Delta E(S_1-T_1) = 900 \text{ cm}^{-1}$  (112 meV) and  $k(S_1 \rightarrow S_0) = 7.1 \cdot 10^6 \text{ s}^{-1}$  (140 ns).<sup>122</sup> This rate corresponds to the prompt fluorescence which, however, cannot be observed directly, because of the much faster competitive inter-system crossing processes, lying in the picoseconds time range.<sup>32,85,105</sup>

The value of  $\Delta E(S_1-T_1) = 900 \text{ cm}^{-1}$  is relatively large. Thus, a third plateau, the  $\tau(\text{TADF})$  plateau, is not attained at  $T = 300$  K.

Figure 2.6 displays an energy level diagram for compound **3** and reproduces relevant emission parameters (compare also next section).

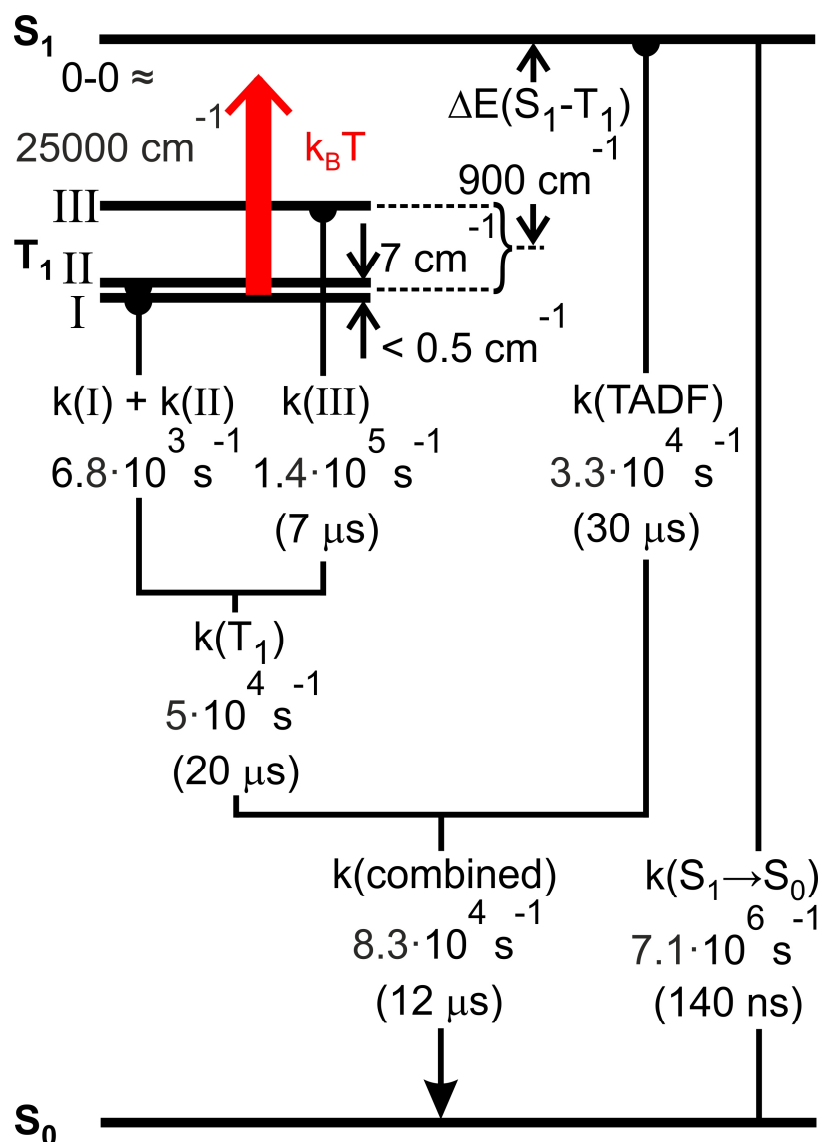


**Figure 2.6:** Schematic energy level diagram with state-related decay rates (times) of [Cu(tpym)(P(*o*-tol)<sub>3</sub>)]PF<sub>6</sub> **3** powder.

## 2.6 Combined emission. Interplay between phosphorescence and TADF

The phosphorescence rate of the  $T_1 \rightarrow S_0$  transition is very fast with  $k(T_1) = 5 \cdot 10^4 \text{ s}^{-1}$  (20  $\mu\text{s}$ ) if compared to most other Cu(I) complexes discussed so far. Thus, although TADF emission grows in with temperature increase, the phosphorescent decay path still prevails at ambient temperature. This is already indicated by comparing the rates of the individual processes. The TADF rate  $k(\text{TADF})$  can be expressed by

$$k(\text{TADF}) = k(\text{combined}) - k(T_1) \quad (2.3)$$

Here and in Figures 2.6 and 2.7,  $k(\text{combined})$  is defined as  $k(T_1) + k(\text{TADF})$ . With  $k(\text{combined}) = k(300 \text{ K}) = (12 \mu\text{s})^{-1} = 8.3 \cdot 10^4 \text{ s}^{-1}$  and  $k(T_1) = 5 \cdot 10^4 \text{ s}^{-1}$ ,  $k(\text{TADF}) = 3.3 \cdot 10^4 \text{ s}^{-1} = (30 \mu\text{s})^{-1}$  is found (Figure 2.7). For an estimate, assuming equal quantum yields of the  $T_1$  and  $S_1$  emission and setting the individual rates  $k(T_1)$  and  $k(\text{TADF})$  in relation to the total emission rate  $k(\text{combined})$ , a ratio of the intensity contributions of phosphorescence : TADF  $\approx 60 \% : 40 \%$  at ambient temperature is obtained. Accordingly, compound **3** can be regarded as being dominantly a phosphorescent emitter even at ambient temperature.<sup>123</sup> The TADF emission represents a supporting emission path. In contrast, for almost all other Cu(I) complexes reported so far, the TADF path dominates at ambient temperature.

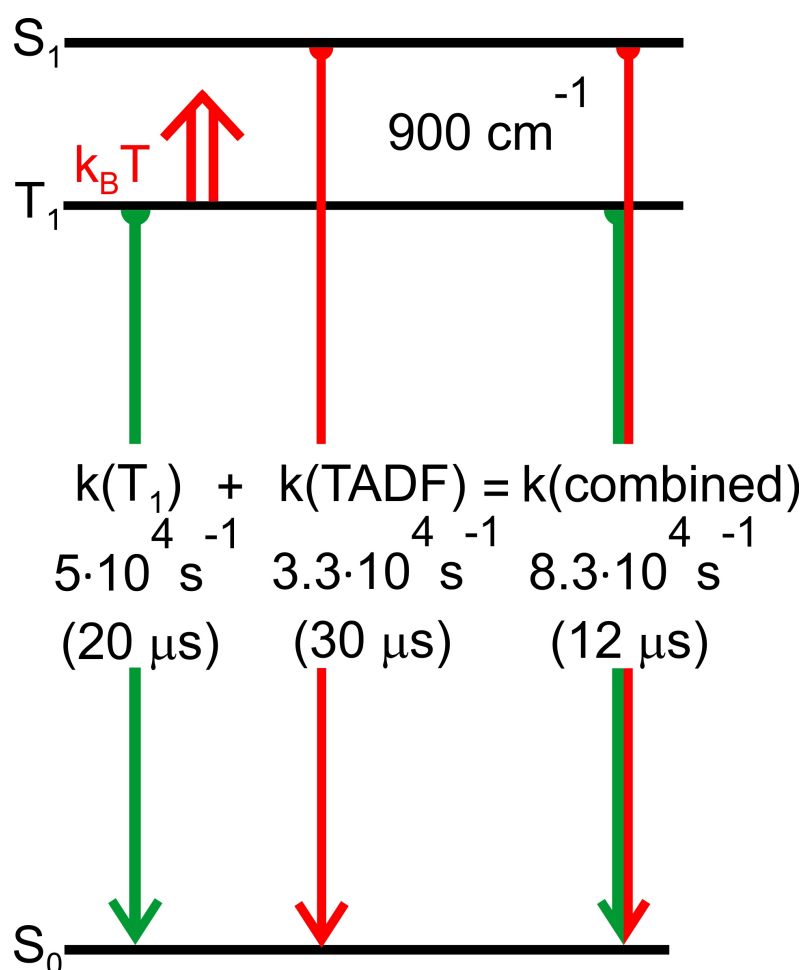


**Figure 2.7:** Schematic energy level diagram and decay times of  $[\text{Cu}(\text{tpym})(\text{P}(o\text{-tol})_3)]\text{PF}_6$  **3** powder. At ambient temperature, the emission stems dominantly ( $\approx 60 \%$ ) from the lowest excited triplet  $T_1$  state as phosphorescence, which is assisted by TADF ( $\approx 40 \%$ ) from the singlet state  $S_1$ .

## 2.7 Conclusion

It is demonstrated that the strategy of rigidifying molecular structures of Cu(I) complexes to largely suppress geometry reorganizations upon excitation, and hence nonradiative processes, is highly successful. To achieve this aim, design rules for the studied Cu(I) complexes were developed based on DFT and TDDFT calculations. In particular, it could be shown that confining the bending angle P-Cu-C16 (see Figure 2.2) of the mono-dentate ligand relative to the Cu(I)-tripod moiety is of dominant importance for reducing nonradiative processes. Indeed, for compounds dissolved in a fluid solution, such confinement leads to an emission quantum yield increase by several orders of magnitude, if the compound [Cu(tpym)(PPh<sub>3</sub>)]PF<sub>6</sub> **2** with no substitution at the phosphine ligand is compared to [Cu(tpym)(P(*o*-butyl-ph)<sub>3</sub>)]PF<sub>6</sub> **4** with three *ortho* *n*-butyl substituents. For **4** dissolved in dichloromethane, even a benchmark value highlighting at  $\Phi_{\text{PL}} = 76 \%$  is obtained. Such a high quantum yield for dissolved Cu(I) complexes has not been reported before publishing the investigated compounds.<sup>118</sup>

The compounds studied exhibit relatively strong spin-orbit coupling with respect to the lowest triplet state T<sub>1</sub> leading to a high allowedness of the phosphorescence and a distinct zero-field splitting of the T<sub>1</sub> state. The phosphorescence intensity (60 %) even predominates the ambient temperature thermally activated delayed fluorescence (40 %). Therefore, in comparison to compound **1** (see chapter 1) show this compound an even higher expression of this effect. Accordingly, the material used in an OLED acts simultaneously as a singlet and triplet exciton harvesting emitter compound. This concept does not only reduce the overall emission decay time, which might lead to an increase of the device lifetime, but, in future, might also allow researchers to obtain a deeper insight into the dynamics of triplet and singlet excitons<sup>124</sup> generated in an OLED emitter layer.

### 3 Symmetry based design strategy of dinuclear Cu(I) compounds with unprecedentedly fast decaying TADF

This chapter has been published recently in ref. 38. For all emitters, the emission decay time should be as short as possible to reduce device stability problems and roll-off effects.<sup>125</sup> However, this is a challenge: Short TADF decay time requires a small energy gap  $\Delta E(S_1-T_1)$  between the lowest singlet  $S_1$  and triplet  $T_1$  excited states and a fast radiative rate  $k^r(S_1 \rightarrow S_0)$  ( $S_0$  = electronic ground state).<sup>36,37,126</sup> For Cu(I) complexes, a small gap can be achieved for charge transfer (CT) transitions and is related to a small exchange interaction<sup>36,37,95,96</sup> and, thus, a small donor-HOMO to acceptor-LUMO overlap. However, small HOMO-LUMO overlap is usually related to a small transition dipole moment and, thus, a small radiative rate  $k^r(S_1 \rightarrow S_0)$ .<sup>36,37</sup> For completeness, it is mentioned that for many organic TADF molecules the condition of small donor-acceptor orbital overlap is not sufficient to guarantee a small gap between the CT states, since an additional state of different character, for example, a localized excited triplet state ( $^3LE$  states), may become the lowest lying state and, thus, drastically alter the final gap.<sup>126-128</sup> However, for Cu(I) TADF complexes such a situation has not been reported so far.<sup>36,37</sup>

Accordingly, developing TADF Cu(I) emitters that show radiative emission decay times of  $\tau^r(\text{TADF})$  shorter than about 5  $\mu\text{s}$  is very difficult and requires nontrivial approaches.<sup>36,37</sup> It is the main intention of this chapter to present a new and presumably general strategy to increase the radiative rate  $k^r(S_1 \rightarrow S_0)$  while maintaining  $\Delta E(S_1-T_1)$  small. Indeed, this is successful and leads to benchmark TADF decay times as short as  $\tau = 1.2 \mu\text{s}$  ( $\tau^r = 1.5 \mu\text{s}$ ). This strategy is exemplified by designing a new type of dinuclear Cu(I) complexes.

The new strategy is inspired by the well-known Davidov model<sup>129-132</sup> that is applied here for the first time to TADF materials. The original Davidov model is related to two equal, symmetry related molecules that are sitting in a unit cell of a crystal. The transition dipole moments  $\vec{\mu}$  referring to transitions between an excited singlet state and an electronic ground state of these two molecules can couple by adding and subtracting the transition dipole moment vectors, respectively. Thus, one obtains two modified transition dipoles for the coupled situation that are related to two energy states,  $S_1$  and  $S_2$ . Guided by this idea, a specific Cu(I) monomer complex was designed that exhibits low-lying metal-to-ligand CT (MLCT) transitions and that can be modified by attaching a second quasi-monomer unit in an almost linear substitution to give a dimer. This approach is schematically presented in Figure 3.1.

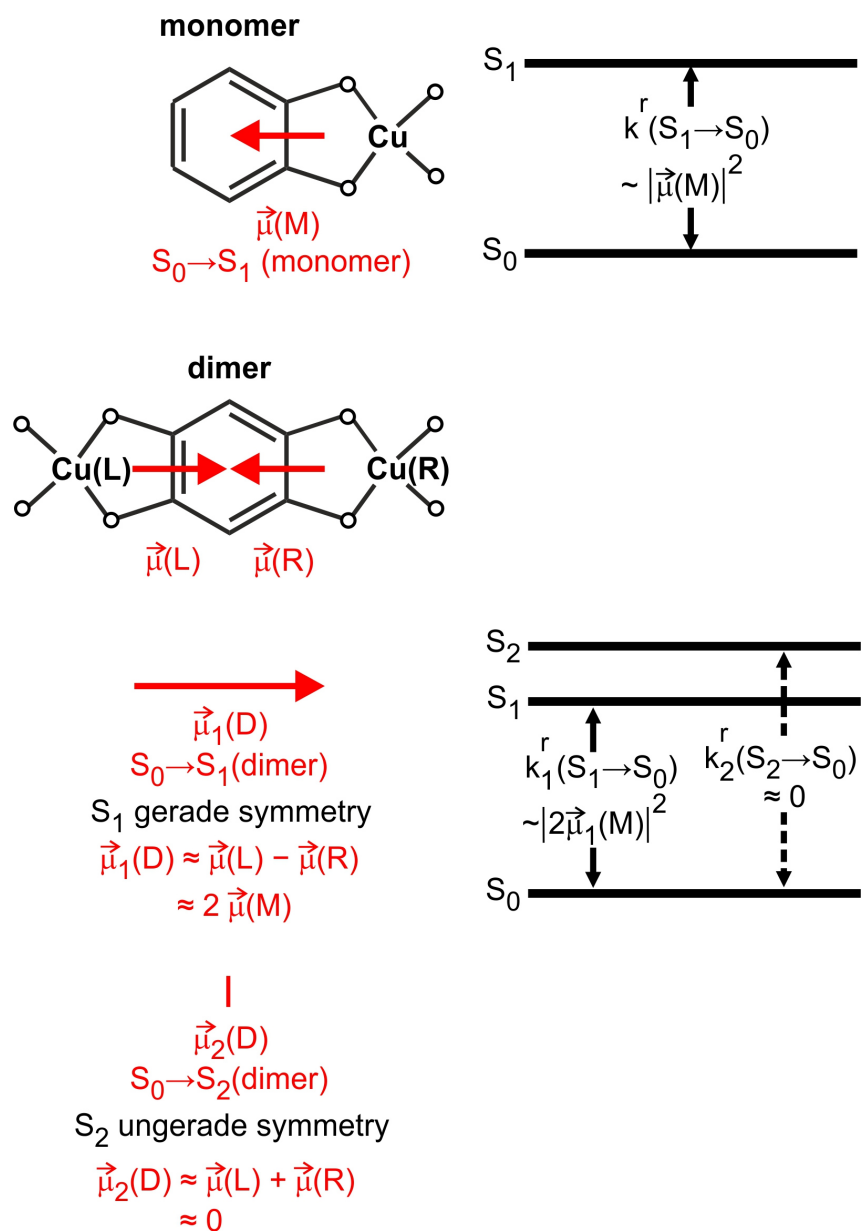


**Figure 3.1:** Schematic guiding model for a Cu(I) dimer with a left(L)-right(R) inversion symmetry relation. For this dimer, one finds a distinctly faster rate of the  $S_1 \rightarrow S_0$  transition than for a related monomer, however, maintaining a small  $\Delta E(S_1 - T_1)$  energy gap. The model does not provide the sequence of the two singlet states  $S_1$  and  $S_2$  of the dimer. However, TD-DFT calculations, as discussed below, will show that the  $S_1$  ( $^1\text{MLCT}$ ) dimer state will be the lower one in energy. The triplet states are not discussed in this guiding model. TD-DFT calculations place them energetically below but near to the singlets (see below).  $k^r$  is the radiative rate that is proportional to the squared transition dipole moment.

According to the schematic model, the dimer D consists of the “left” and the “right” copy of the quasi-monomer M.<sup>38</sup> Both are related by an inversion (*i*) symmetry that lies in the center of the benzene ring of the dimer D. Each quasi-monomer exhibits a  $^1\text{MLCT} \leftrightarrow S_0$  transition dipole, however, oriented in a parallel and an anti-parallel way,

respectively. They will couple and, thus, generate two resulting dimer transition dipoles  $S_1 \leftrightarrow S_0$  and  $S_2 \leftrightarrow S_0$ . As illustrated in Figure 3.1, the transition dipoles of the two quasi-monomers  $\vec{\mu}(M)$  can essentially cancel for one of the symmetry-adapted states to give  $\vec{\mu}_2(D) \approx 0$ , but add to an approximately twice as large transition dipole  $\vec{\mu}_1(D) \approx 2\vec{\mu}(M)$  for the other symmetry-adapted state. As a consequence of the latter situation, it is expected to find a coarsely four times faster radiative rate for the dimer in comparison to the monomer. It is remarked that similar considerations can also apply in other (approximate or quasi) 2-fold symmetry situations. Below, the model's validity will be demonstrated by a TD-DFT approach. Further, in section 8 of the supplementary information,<sup>38</sup> the guiding model is illustrated in a simple orbital model. In addition to the guiding model, it is expected to have two energetically low-lying triplet states. However, although this guiding model should not be over-interpreted, the model would predict only very small changes of the triplet state properties, since the corresponding transition dipole moments are very small.<sup>129-132</sup> Moreover, since spin-orbit coupling (SOC) is a short-range interaction, significant changes of the triplet state properties due to coupling between the "left" and the "right" centers are not expected.

In a particularly favorable situation, the  $S_1$  dimer state, the one that carries the faster radiative rate, represents the energetically lower lying singlet state. In this situation, it is expected to find a small  $\Delta E(S_1-T_1)$  gap combined with a high  $S_1 \leftrightarrow S_0$  oscillator strength.

Indeed, using this schematic guiding model, a benchmark Cu(I) dimer can be realized that shows the one of the shortest radiative TADF decay time found for Cu(I) complexes so far,<sup>118</sup> amounting to a value lying only slightly above 1  $\mu$ s.

For completeness, it is referred to a different design approach that has been applied recently to organic TADF molecules to keep large oscillator strengths when reducing the  $\Delta E(S_1-T_1)$  gap. For example, for accordingly designed coplanar donor-acceptor molecules, one finds a large (calculated) oscillator strength being as high as  $f = 0.8$  at a gap of about 0.4 eV. Even at this large gap, it is still possible to observe TADF that decays in a millisecond range.<sup>133</sup>

This chapter is organized as follows: In the first part, an adequate monomer is presented and will be characterized by TD-DFT model calculations as well as by photophysical studies, while the focus of this chapter lies in section 3.4, where a series of dimer molecules is described that indeed represent benchmark materials. In section 3.6, the obtained results were compared to a series of other Cu(I) compounds.

## 3.1 Monomer Cu(dppb)(PPh<sub>3</sub>)Cl

### 3.1.1 Synthesis and chemical characterization

The chemical structure of compound **5** is reproduced in Figure 3.2.

Synthesis, chemical characterization, and X-ray structure data of compound **5** were provided by Dr. Alfiya F. Suleymanova and Marsel Z. Shafikov<sup>38</sup> and are summarized in the SI sections 1 and 2 of ref. 38.

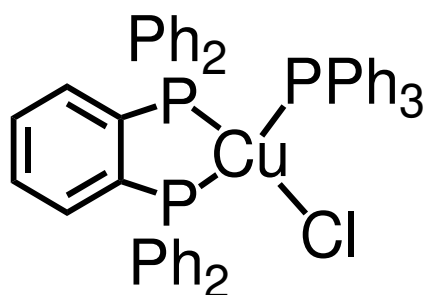
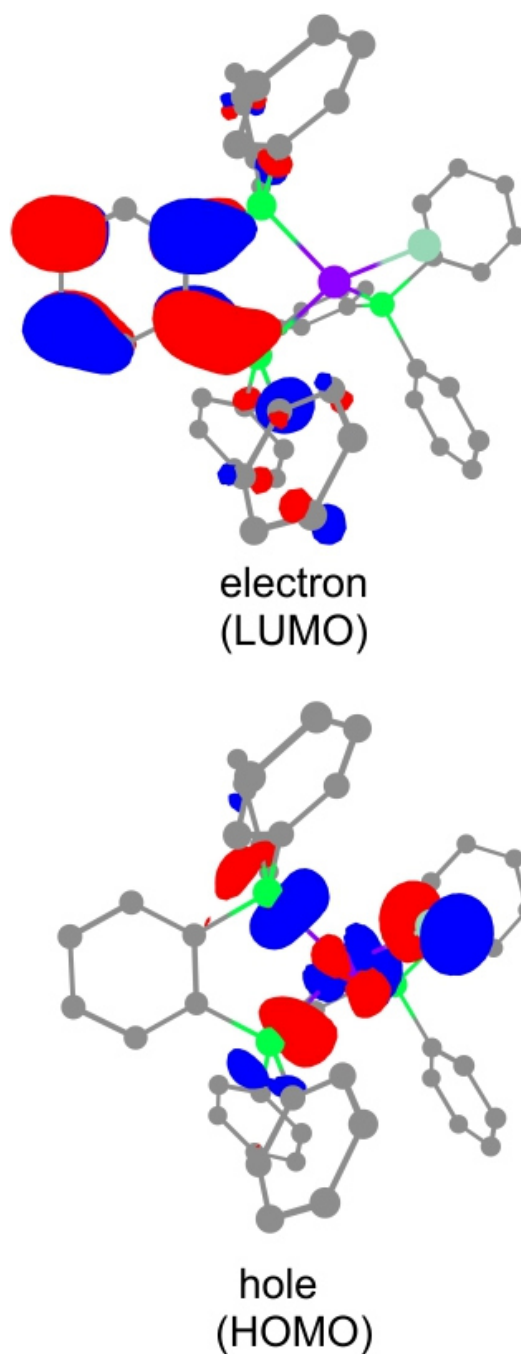


**Figure 3.2:** Chemical structure of Cu(dppb)(PPh<sub>3</sub>)Cl **5**

### 3.1.2 DFT and TD-DFT calculations of the monomer Cu(dppb)(PPh<sub>3</sub>)Cl

DFT/TD-DFT calculations, carried out with the NWChem 6.5 code<sup>82</sup> at the B3LYP/def2-SVP level of theory<sup>80,81</sup> for the optimized triplet state geometry (if not mentioned otherwise), give the NTOs (natural transition orbitals) as reproduced in Figure 3.3. The optimized triplet T<sub>1</sub> state geometry is used, because the focus is on emission properties. Further, it is assumed that the lowest singlet state S<sub>1</sub> geometry is similar to the T<sub>1</sub> state geometry, because in the latter one both states result from a transition between largely the same orbital contributions (see below). A similar approach is discussed in some detail in ref. 59.



### NTOs for the $S_1$ state

**Figure 3.3:** Contour plots of NTOs (natural transition orbitals) referring to the  $S_1$  ( $^1\text{MLCT}$ ) state (iso-value = 0.04). These orbitals are mainly composed of the highest occupied orbital (HOMO) and the lowest unoccupied molecular orbital (LUMO) of  $\text{Cu}(\text{dppb})(\text{PPh}_3)\text{Cl}$  **5**, respectively. The NTOs of the  $T_1$  state (not shown) are almost identical to the ones reproduced for the  $S_1$  state. Further MOs are displayed in Figure SI-12 of ref. 38. The calculations were performed at the B3LYP/def2-SVP level of theory for the optimized gas phase  $T_1$  state geometry. All hydrogen atoms are omitted for clarity.

TD-DFT calculations show that the transition between NTOs, as displayed in Figure 3.3, represents a charge transfer (CT) transition with dominant charge rearrangements from Cu (40 %), P (27 %), and Cl (12 %) (charge contributions as calculated for the distribution of the HOMO) to the benzene ring. The TD-DFT calculations reveal that the resulting  $^3\text{MLCT}$  ( $T_1$ ) and  $^1\text{MLCT}$  ( $S_1$ ) states are of 98.6 % and 99.3 % of HOMO $\rightarrow$ LUMO character, respectively. (Table SI-5 of ref. 38) Therefore, the corresponding NTOs essentially represent HOMO (hole) and LUMO (electron), respectively. In Figure 3.3, only the NTOs for the  $S_1$  state are reproduced, since those referring to the  $T_1$  state are almost identical. However, both states exhibit an energy difference of 57 meV ( $460\text{ cm}^{-1}$ ).

The TD-DFT calculated  $\Delta E(S_1-T_1)$  value amounts to  $460\text{ cm}^{-1}$  (57 meV). This indicates already that an occurrence of TADF at ambient temperature can be expected. As will be shown below, the experimentally determined activation energy is very close, amounting to  $490\text{ cm}^{-1}$  (61 meV). The next higher lying states,  $T_2$  and  $S_2$  (calculated in the  $T_1$  optimized geometry), are found by 0.56 and 0.59 eV higher in energy than  $T_1$  and  $S_1$ , respectively. (See Table SI-5 of ref. 38) Thus,  $T_2$  and  $S_2$  are well separated from  $T_1$  and  $S_1$  and will not be involved in the thermal activation process. For a later comparison, the oscillator strength of the  $S_0\rightarrow S_1$  transition will be determined. Since this value depends distinctly on the geometry of the complex and, in particular, on distortions that occur upon excitation, it will be referred in this case to the ground state  $S_0$  geometry. The corresponding value amounts to  $f(S_0\rightarrow S_1, \text{monomer}) \approx 0.01269$ . (Table SI-3 of ref. 38.)

### 3.1.3 Photophysical studies of the monomer $\text{Cu}(\text{dppb})(\text{PPh}_3)\text{Cl}$

In Figure 3.4a, absorption and emission spectra are displayed for the monomer compound **5**. In the lower wavelength range up to  $\approx 300\text{ nm}$  intense absorption bands are seen. They are assigned to  $\pi\rightarrow\pi^*$  transitions of the dppb and the  $\text{PPh}_3$  ligand. The broad shoulder between about 350 nm and 410 nm is attributed to electronic transitions being assigned to  $S_0\rightarrow ^1\text{MLCT}$  transition(s). As powder, complex **5** shows green-blue emission at ambient temperature with an emission quantum yield of  $\Phi_{\text{PL}} = 58\%$ . The emission maxima are found at 548 nm (300 K) and 566 nm (10 K). The bands are broad and unstructured even at  $T = 10\text{ K}$  or 1.6 K. An unstructured shape is typical for charge transfer (CT) transitions. This result excludes an assignment to ligand localized (LE) transitions.

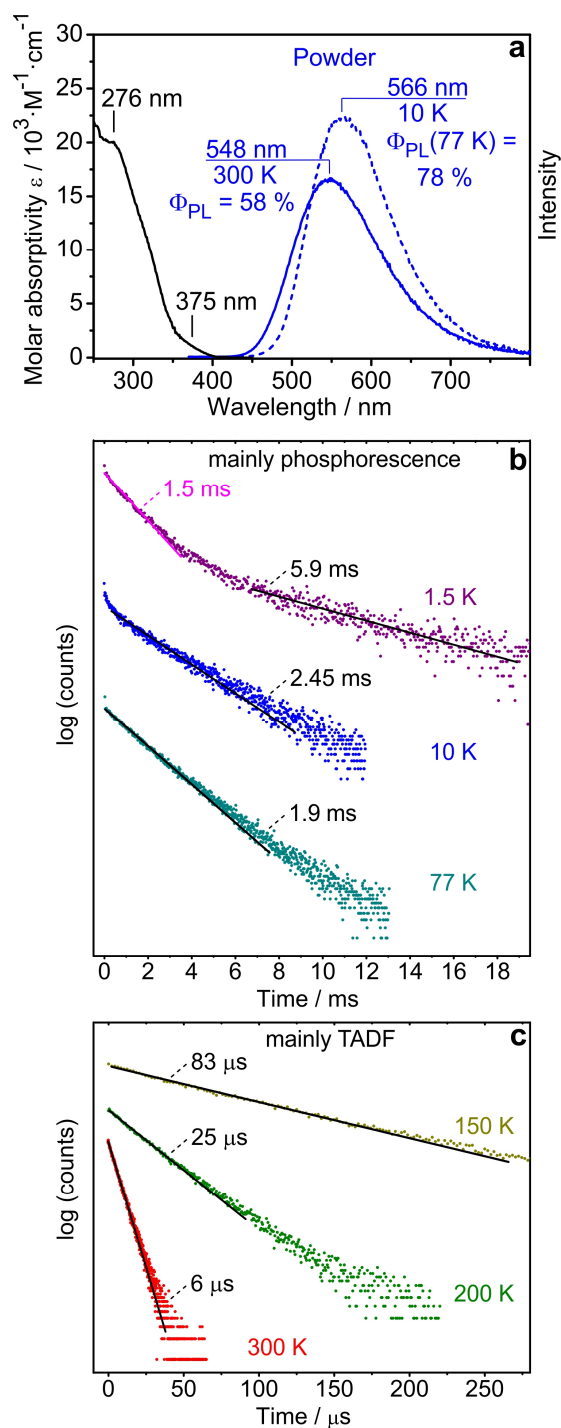


**Figure 3.4.** (a) Absorption spectrum of compound  $\text{Cu}(\text{dppb})(\text{PPh}_3)\text{Cl}$  **5** dissolved in chloroform  $c \approx 10^{-5} \text{ mol/L}$  ( $T = 300 \text{ K}$ ) and emission spectra of the powder at 300 K (solid blue line) and 10 K (dashed blue line), respectively. Excitation wavelength  $\lambda_{\text{exc}} = 330 \text{ nm}$ . (b, c) Emission decay curves and decay times of  $\text{Cu}(\text{dppb})(\text{PPh}_3)\text{Cl}$  **5** powder at different temperatures.  $\lambda_{\text{exc}} = 378 \text{ nm}$ ,  $\lambda_{\text{det}} = 550 \text{ nm}$ , and excitation pulse width  $< 100 \text{ ps}$  for all decay curves. Properties of the nonmono-exponential decay curve measured at  $T = 1.5 \text{ K}$  are discussed in SI section 4 of ref. 38. Note the different time scales in b and c.

The unstructured spectral form is a consequence of strong structural reorganizations upon excitation induced by a distinct change of electron density and the involvement of a large number of vibrations and local phonons in the Franck-Condon transitions. A similar behavior is found for almost all Cu(I) complexes.<sup>34-37,39,40,43,49,56-59,98</sup> It is mentioned that the emission of compound **5** dissolved in chloroform is almost quenched, showing a quantum yield of  $\Phi_{\text{PL}} < 1 \%$ . The situation is similar for compound **6**.

The shift of the peak maximum from 566 nm at  $T = 10 \text{ K}$  to 548 nm at 300 K by 18 nm ( $580 \text{ cm}^{-1}$ , 72 meV) is rationalized by the occurrence of a thermally activated emission from the energetically higher lying  $S_1$  state to the electronic ground state  $S_0$ , representing a TADF emission at ambient temperature. This assignment is strongly supported by the drastic decrease of the emission decay time from  $\tau = 2.45 \text{ ms}$  at  $T = 10 \text{ K}$  to  $6 \mu\text{s}$  at 300 K as displayed in the Figure 3.4b, c. These figures reproduce the emission decay times measured at different temperatures. At  $T = 1.5 \text{ K}$ , the decay is strongly non-mono-exponential indicating that fast thermalization does not occur between the involved states (see below). However, above  $T = 10 \text{ K}$ , the mono-exponential part strongly prevails induced by fast thermal equilibration processes. In this situation, a plot of the emission decay times versus temperature follows a Boltzmann-type behavior.

In the temperature range  $\approx 10 \text{ K} \leq T \leq 50 \text{ K}$ , one finds a plateau that is determined by the  $T_1 \rightarrow S_0$  phosphorescence process with a very long decay time of  $\tau(T_1) = 2450 \mu\text{s}$ . (Figure SI-15 of ref. 38) This demonstrates weak SOC between the  $T_1$  state and higher lying singlet states. The  $S_1$  state, lying energetically proximate, is not active with respect to SOC due to the El-Sayed-forbiddenness.<sup>12,97,134</sup> (For further discussion see the SI section 4 of ref. 38) With growing temperature, the  $S_1$  state is increasingly populated and the complex' decay time decreases drastically to  $\tau(\text{TADF}) = 6 \mu\text{s}$  at ambient temperature. (Figure 3.4b, c)

By use of the relation of  $k^r = \Phi_{\text{PL}} \cdot \tau^{-1}$  with  $k^r$  being the radiative emission decay rate, it is found that the radiative decay rate increases by a factor of 300 from  $3.2 \cdot 10^2 \text{ s}^{-1}$  at  $T = 10 \text{ K}$  to  $9.7 \cdot 10^4 \text{ s}^{-1}$  at  $T = 300 \text{ K}$ . (The quantum yield at  $T = 300 \text{ K}$  and 77 K has been determined to 58 % and 78 %, respectively. For an estimate of the 10 K rate, it is assumed that  $\Phi_{\text{PL}}$  is the same as measured at 77 K.) The large rate increase is a consequence of the  $S_1(^1\text{MLCT})$  state population from the  $T_1(^3\text{MLCT})$  state with temperature increase and a fast  $S_1 \rightarrow S_0$  decay. This represents a typical TADF behavior.

For completeness it is mentioned that although the radiative rate increases by a factor of 300 with temperature increase from  $T = 77 \text{ K}$  to  $T = 300 \text{ K}$ , the emission quantum yield becomes even lower. A similar behavior has been observed for almost all Cu(I) TADF complexes investigated so far.<sup>36,37,49</sup> Obviously, with increasing temperature additional nonradiative decay paths are activated via population of the  $S_1$  state and/or

higher lying vibrational states. (Compare also refs. 94, 135 and 136.) Thus, the nonradiative rate increase overbalances the radiative rate increase.

From a fit procedure using a Boltzmann-type equation (see section 3.4 and SI section 4 of ref. 38), important photophysical parameters for compound **5** can be determined. In particular, an activation energy of  $\Delta E(S_1-T_1) = 490 \text{ cm}^{-1}$  (61 meV) is found. Similar values were found by the TD-DFT calculation and the shift of the emission peak maximum. (Figure 3.4a) In many respects, the properties of compound **5** are similar to those found for  $\text{Cu}(\text{dppb})(\text{pz}_2\text{Bph}_2)$ , a complex with the same chromophoric ligand dppb and with  $\text{pz}_2\text{Bph}_2 = \text{diphenylbis}-(\text{pyrazol-1-yl})\text{borate}$ .<sup>36,37,98</sup> For compound **5**, the fit procedure allows us also to estimate the radiative rate corresponding to the prompt fluorescence to  $k^r(S_1 \rightarrow S_0) \approx 1.9 \cdot 10^6 \text{ s}^{-1}$  (from the fit value of  $k(S_1 \rightarrow S_0) = 3.3 \cdot 10^6 \text{ s}^{-1}$  and  $\Phi_{\text{PL}}(300 \text{ K}) = 58 \%$ ). This value will be later used for a comparison with the rate of the Cu(I) dimer. For completeness, it is mentioned that the prompt fluorescence is not observed directly due to a time resolution of our equipment in the ns region. The ISC from  $S_1$  to  $T_1$  is much faster, it lies in the 10 ps time range.<sup>85,105,137</sup>

In Figure 3.5, important emission data of compound **5** are summarized in an energy level diagram.

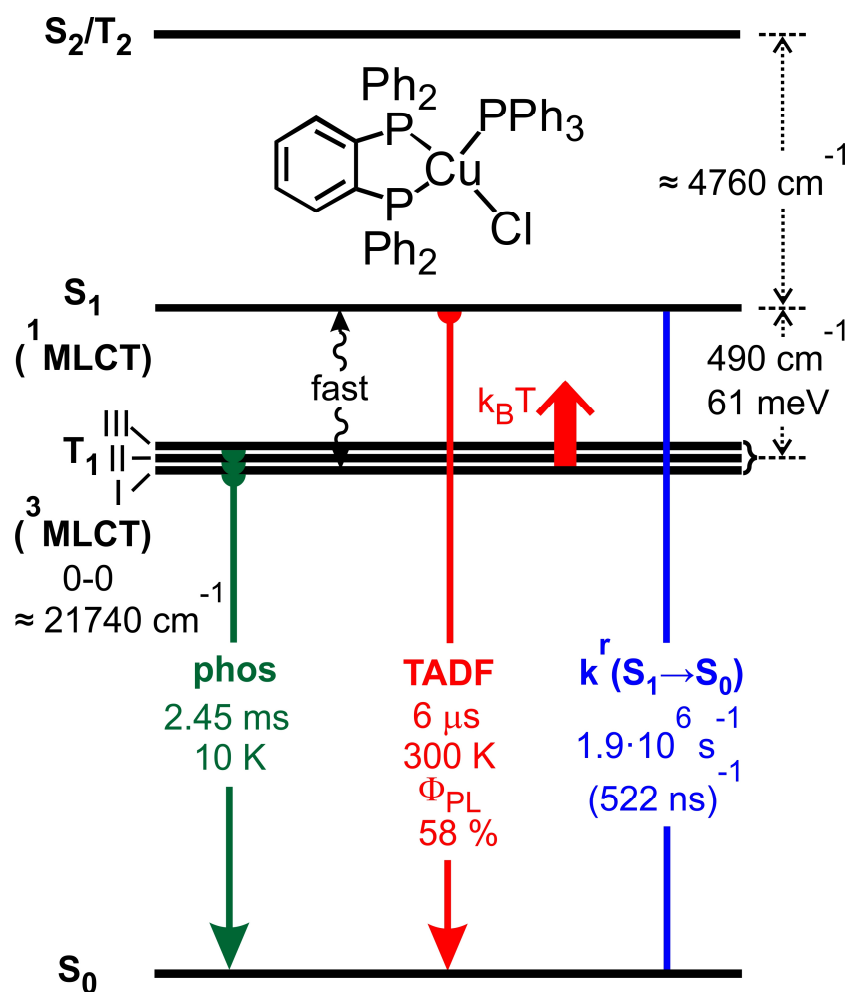


**Figure 3.5:** Schematic energy level diagram with state-related decay rates or times of Cu(dppb)(PPh<sub>3</sub>)Cl **5** powder. The decay time at T = 77 K with  $\tau(77\text{ K}) = 1860\ \mu\text{s}$  is distinctly shorter than at T = 10 K. (Figure 3.4b, c) This indicates that TADF emission is already important at T = 77 K. Note, the higher lying states S<sub>2</sub> and T<sub>2</sub> (Table SI-5 of ref. 38) are too high in energy to be involved in the thermal activation processes. The 0-0 energy of the T<sub>1</sub>→S<sub>0</sub> transition is estimated from the blue flank of the 10 K emission spectrum. (Figure 3.4a) The 10 K phosphorescence decay time corresponds to a low-temperature plateau. The individual decay times of the triplet substates I, II, and III are determined to  $\tau(\text{I}) = 5.9\ \text{ms}$ ,  $\tau(\text{II}) = 2.6\ \text{ms}$ , and  $\tau(\text{III}) = 1.5\ \text{ms}$ , respectively. (See SI section 4 of ref. 38 and also section 3.4.)

## 3.2. Dimers $\text{Cu}_2(\text{tppb})(\text{PPh}_3)_2\text{X}_2$ with X = Cl **6**, Br **7**, I **8**, and NCS **9**

### 3.2.1 Syntheses and chemical characterizations

The chemical structure of the dimer compounds is displayed in Figure 3.6.

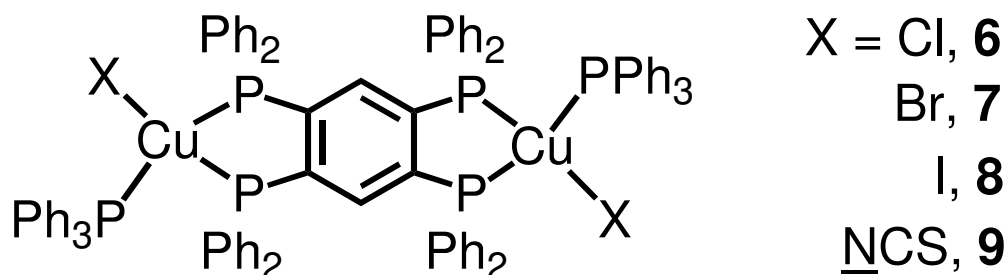


**Figure 3.6:** Chemical structure of the dimer compounds  $\text{Cu}_2(\text{tppb})(\text{PPh}_3)_2\text{X}_2$ .

Syntheses, chemical characterizations, X-ray structure data, and UV spectra for all four dimer compounds were done by Prof. Rongmin Yu et. al.<sup>38</sup> and are given in the SI sections 1 and 2 of ref. 38. Photophysical investigations reveal that the emission properties of all four compounds are similar. Therefore, mainly characteristics of compound **6**  $\text{Cu}_2(\text{tppb})(\text{PPh}_3)_2\text{Cl}_2$  will be discussed here as a representative example and a short comparison with the other compounds will be given at the end of this section. Photophysical details for all four compounds are summarized in the SI section 5 of ref. 38.

### 3.2.2 DFT and TD-DFT calculations for the representative dimer $\text{Cu}_2(\text{tppb})(\text{PPh}_3)_2\text{Cl}_2$ **6**

For a first insight into the electronic structure of compound **6**, the NTOs for the two lowest symmetry-related singlet states are reproduced as resulting from DFT/TD-DFT calculations with the NWChem 6.5 code<sup>82</sup> at the B3LYP/def2-SVP level of theory<sup>80,81</sup> for the optimized triplet state geometry (in gas phase). (Figure 3.7) Also here, it is assumed that the geometry of the  $T_1$  state approximates the geometries of the two lowest excited singlets.

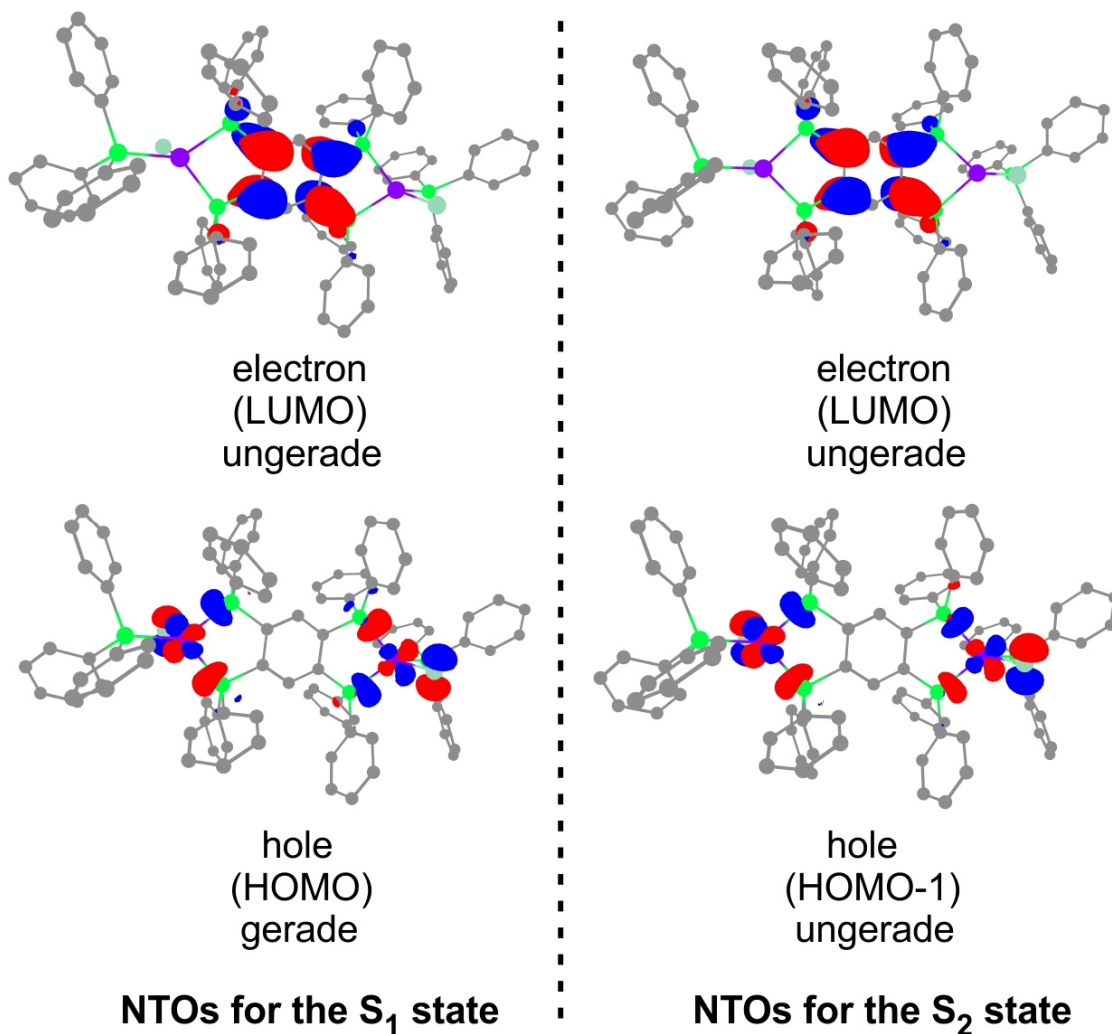


**Figure 3.7:** NTO iso-surface contour plots (iso-value 0.04) for the singlet states  $S_1$  and  $S_2$  of  $\text{Cu}_2(\text{tppb})(\text{PPh}_3)_2\text{Cl}_2$  **6** estimated by the “Chemission” program from the output of a TD-DFT calculation conducted at the relaxed  $T_1$  state geometry. The NTOs of the related triplets,  $T_1$  and  $T_2$ , are similar to those of the corresponding singlets and therefore, are not reproduced. Remark: In an assumed  $C_i$  point group, the inversion center  $i$  lies in the center of the benzene ring. Thus, the hole NTO of the  $S_1$  state, mainly composed of the HOMO, displays an even (gerade) symmetry, while the hole NTO of the  $S_2$  state, mainly composed of HOMO-1, shows an odd (ungerade) symmetry. The electron NTOs of both  $S_1$  and  $S_2$  states are composed of the LUMO and feature odd (ungerade) symmetry.

The calculations show that the transitions between the NTOs, as displayed in Figure 3.7, are also of CT character with essential charge transfer from Cu (35 %), P (27 %), and Cl (12 %) (charge contributions as calculated for the distribution of the HOMO) to the benzene ring, again abbreviated as MLCT transitions. The TD-DFT calculations reveal that the resulting  $^3\text{MLCT}$  ( $T_1$ ) and  $^1\text{MLCT}$  ( $S_1$ ) states are of 98.5 % and 99.1 % of HOMO $\rightarrow$ LUMO character, respectively. (Table SI-9 of ref. 38) Therefore, the

corresponding NTOs represent essentially HOMO (hole) and LUMO (electron), respectively (Table SI-9 of ref. 38). Equivalent considerations apply for the states  $T_2$  and  $S_2$ . In Figure 3.7, only the NTOs for the  $S_1$  and the  $S_2$  state are reproduced, since those of the  $T_1$  and  $T_2$  states are almost identical to the respective singlets. All states exhibit different energies. In particular, the energy splitting of the two singlets is relatively small and amounts to  $\Delta E(S_2-S_1) = 1105 \text{ cm}^{-1}$  (137 meV). Further energies are summarized in Table 3.1 relative to the energy of the lowest lying triplet state  $T_1$ . In the subsequent discussion, the focus is on the four lowest lying states, since the energetically next states are found at distinctly higher energies. (See Table SI-9 of ref. 38.)

**Table 3.1:** Lowest excited states of  $\text{Cu}_2(\text{tppb})(\text{PPh}_3)_2\text{Cl}_2$  **6**, their main orbital characters, the oscillator strengths for the transition to the electronic ground state  $S_0$ , and energy separations relative to the  $T_1$  state based on TD-DFT calculations at the B3LYP/def2-SVP level of theory for the  $T_1$  state optimized geometry in gas phase for vertical excitations. (Compare also Table SI-9 of ref. 38.)

state	transition	Dipole oscillator strength $f$	$\Delta E$ from $T_1$
$T_1$	98.5 % HOMO $\rightarrow$ LUMO	–	–
$S_1$	99.1 % HOMO $\rightarrow$ LUMO	0.04380	62 meV (500 $\text{cm}^{-1}$ )
$T_2$	97.9 % HOMO-1 $\rightarrow$ LUMO	–	114 meV (920 $\text{cm}^{-1}$ )
$S_2$	99.0 % HOMO-1 $\rightarrow$ LUMO	0.00011	199 meV (1605 $\text{cm}^{-1}$ )

Particularly instructive is the information obtained from TD-DFT calculations. In contrast to the monomer, more energy states in a relatively small energy range of about 2000  $\text{cm}^{-1}$  (250 meV) above the lowest  $T_1$  state are found, as summarized in Table 3.1. Here, not the absolute calculated transition energies are reproduced, but energy separations to the lowest  $^3\text{MLCT}$  ( $T_1$ ) state. These states essentially govern the TADF behavior. In contrast to absolute energies, energy separations are frequently displayed with acceptable accuracy by TD-DFT calculations.<sup>138-140</sup> For example, the experimental and the calculated value for  $\Delta E(S_1-T_1)$  amount to 48 meV (390  $\text{cm}^{-1}$ ) (see below) and 62 meV (500  $\text{cm}^{-1}$ ) (Table 3.1), respectively.

### 3.3 TD-DFT calculations and guiding model

Interestingly, the calculated results display a marked correspondence to our simple guiding model as presented in section 3.1. Moreover, the energy sequence of the two lowest singlet states, which could not be predicted by the model, results from the calculations:

- (i) The lower lying singlet state  $S_1$  represents the one that refers to the transition from the HOMO (with significant metal character) of gerade symmetry (in the (approximate)  $C_i$  point group)  $\rightarrow$  the LUMO (mainly located at the benzene ring). (Figure 3.7) The related allowedness with an oscillator strength of  $f(S_1 \rightarrow S_0) = 0.0438$  is relatively large (Table 3.1). In particular, this result is of importance for optimizing the TADF properties.
- (ii) The allowedness of the  $S_2 \rightarrow S_0$  transition of the guiding model molecule is zero. Indeed, the TD-DFT calculation gives a very small value for the oscillator strength of  $f(S_2 \rightarrow S_0) = 0.00011$  for a geometry that is slightly deviating from the  $C_i$  symmetry. This calculated value is a factor of 400 weaker than determined for the  $S_1 \rightarrow S_0$  transition. (Table 3.1)
- (iii) The guiding model predicts a relatively small energy separation between the related  $S_1$  and  $S_2$  states of similar origin. In fact, the calculated  $\Delta E(S_2 - S_1, \text{dimer})$  of 137 meV ( $\approx 1100 \text{ cm}^{-1}$ ) is small (Table 3.1) indicating weak interactions between the two quasi-monomers. In contrast, the monomer exhibits a much larger energy separation of  $\Delta E(S_2 - S_1, \text{monomer}) = 590 \text{ meV}$  ( $4760 \text{ cm}^{-1}$ ). (Figure 3.5) In this latter situation, the two singlets involve different excitations representing HOMO  $\rightarrow$  LUMO and HOMO  $\rightarrow$  LUMO+1 character, respectively.
- (iv) The most important prediction of the guiding model is an increase of the oscillator strength of the dimer compared to the one of the monomer. If it is taken into account that the oscillator strength is proportional to the squared transition dipole moment  $|\vec{\mu}|^2$ <sup>94</sup>, the dimer should exhibit an oscillator strength being a factor of 4 higher. For this comparison, the  $S_0$  state geometry optimized values will be used again to be independent from differences of the oscillator strength values that are induced by the differences in geometry distortions upon excitation. For the dimer,  $f(S_0 \rightarrow S_1, \text{dimer}) = 0.04988$  (Table SI-7 of ref. 38) and for the monomer  $f(S_0 \rightarrow S_1, \text{monomer}) = 0.01269$  (Table SI-3 of ref. 38) is found. Indeed, the TD-DFT calculated value for the dimer is by a factor of 3.93 larger than the one of the monomer, just as predicted.

Obviously, this latter result should be compared to the experimental situation. It will be shown below that the increase of the radiative rate is even slightly more favorable. In particular, the strong increase of the radiative  $S_1 \rightarrow S_0$  rate, combined with a small energy separation  $\Delta E(S_1-T_1)$ , leads to the drastic decrease of the TADF decay time resulting in a measured record value for the Cu(I) dimer **6** of only  $\tau(\text{TADF}) = 1.2 \mu\text{s}$  or for the radiative decay time of  $\tau^r(\text{TADF}) = 1.5 \mu\text{s}$ .

### 3.4 Photophysical studies of the dimer $\text{Cu}_2(\text{tppb})(\text{PPh}_3)_2\text{Cl}_2$

In this section, photophysical properties of  $\text{Cu}_2(\text{tppb})(\text{PPh}_3)_2\text{Cl}_2$  **6** are discussed. Figure 3.8 reproduces absorption and emission spectra. The absorption shows intense bands below about 400 nm that are assigned to  $\pi \rightarrow \pi^*$  transitions of the tppb and the  $\text{PPh}_3$  ligand, while the weaker band in the wavelength range between about 400 nm and 480 nm is assigned to MLCT transitions (with some Cl- and P-orbital contributions).<sup>38</sup> These characterizations are substantiated by the TD-DFT calculations as presented in the previous sections.

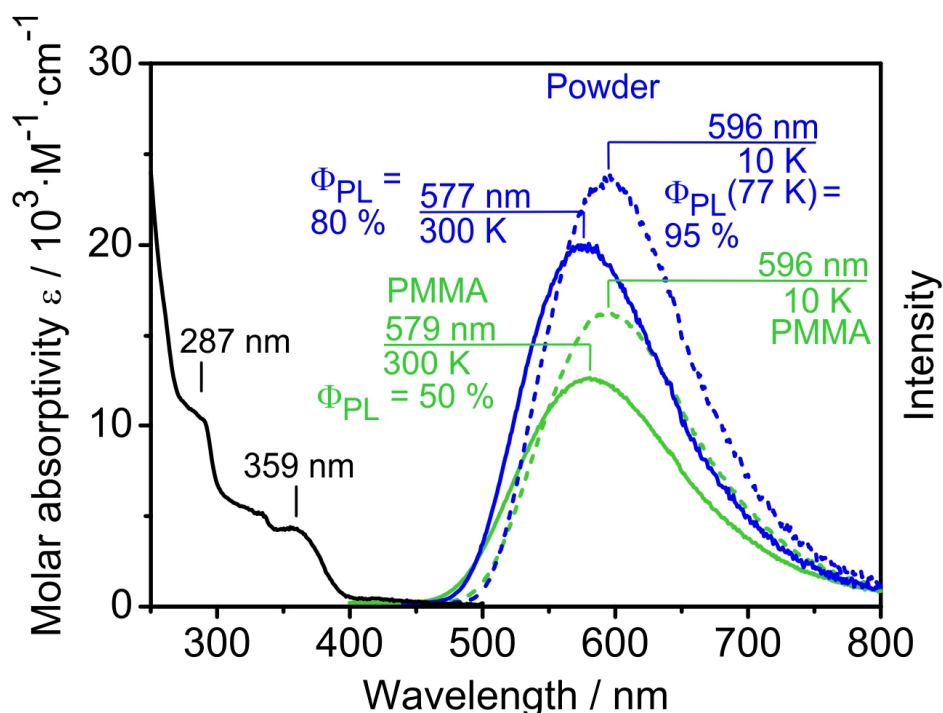


**Figure 3.8.** Absorption spectrum of  $\text{Cu}_2(\text{tppb})(\text{PPh}_3)_2\text{Cl}_2$  **6** dissolved in chloroform  $c \approx 10^{-5}$  mol/L (300 K) and emission spectra of neat powder ( $\lambda_{\text{exc}} = 375$  nm) and doped in PMMA with  $c \approx 1$  w% ( $\lambda_{\text{exc}} = 330$  nm), respectively, measured at different temperatures. Absorption spectra of all investigated dimer compounds were provided by Prof. Rongmin Yu et. al.<sup>38</sup>

The emission spectra, displayed for 300 K and 10 K, are broad and unstructured as expected for CT transitions, similarly as found for the monomer. Also for the dimer,

no indication is found for an involvement of an emitting state of  $^3\text{LE}$  character. The emission quantum yield of the powder of compound **6** is with  $\Phi_{\text{PL}} = 80\%$  at  $T = 300\text{ K}$  significantly higher than the yield of **6** doped in PMMA ( $\Phi_{\text{PL}} = 50\%$ ). A similar behavior has been reported frequently for other Cu(I) complexes and has been rationalized by the higher rigidity in the crystalline environment as compared to the “softer” cage provided by the PMMA matrix.<sup>36,37,49,59,61</sup> Cu(I) compounds have the tendency to exhibit extensive geometry distortions upon MLCT excitation from a quasi-tetrahedral coordination towards a square-planar one. This leads to more distinct nonradiative relaxations from the excited state to the electronic ground state  $S_0$ , since in the distorted case, the Franck-Condon (FC) factors of the energetically higher lying vibrational wavefunctions of the electronic ground state and the lower lying ones of the excited state are significantly larger than in a nondistorted situation.<sup>94</sup> These FC factors govern the nonradiative rate  $k^{\text{nr}}$ .<sup>94,135,136</sup> As a consequence, the more rigid the cage of the environment (external rigidity) the higher is the emission quantum yield. Just this behavior is observed for compound **6**. For completeness, it is mentioned that the rigidity of the molecule itself (internal rigidity) can be equally important as has been reported for Cu(I)<sup>52,59</sup> and Ag(I)<sup>36,60,61</sup> complexes with emission quantum yields of up to  $\Phi_{\text{PL}} = 76\%$  even in fluid solution and of  $100\%$  in a crystalline environment, respectively.<sup>141</sup> An increase of internal rigidity seems in part to be responsible for the higher quantum yield of compound **6** than of **5**. (See also below.) The observed blue shift of the emission by  $19\text{ nm}$  ( $552\text{ cm}^{-1}$ ,  $68\text{ meV}$ ) from  $T = 10\text{ K}$  to  $300\text{ K}$  (Figure 3.8) of the powder of compound **6** indicates already the occurrence of TADF emission at  $T = 300\text{ K}$ . This, however, is mainly substantiated by the drastic increase of the radiative rate. At  $T = 10\text{ K}$ , one observes a long-lived  $T_1 \rightarrow S_0$  phosphorescence with  $\tau(10\text{ K}) = 2.3\text{ ms}$  (Figure 3.9a) giving the radiative rate  $k^{\text{r}}(10\text{ K}) = 4.1 \cdot 10^2\text{ s}^{-1}$  (at  $\Phi_{\text{PL}} = 95\%$ , assuming the same value as measured at  $T = 77\text{ K}$ ), while up to  $300\text{ K}$  with  $\tau = 1.2\text{ }\mu\text{s}$  and  $\Phi_{\text{PL}} = 80\%$ , the radiative rate grows in to  $k^{\text{r}}(300\text{ K}) = 6.7 \cdot 10^5\text{ s}^{-1}$ . (Figure 3.9) Hence, one finds an increase by a factor of more than 1600. Obviously, a different transition becomes involved at higher temperature, representing the  $S_1 \rightarrow S_0$  transition and thus, the typical TADF behavior. Figure 3.9 displays the emission decay time and behavior of compound **6** at different temperatures. Above  $T \approx 10$  or  $15\text{ K}$ , thermal relaxation between the involved excited states is faster than the individual emission decay times. Thus, a largely mono-exponential decay is observed. This is representative of a Boltzmann distribution between the substates of the triplet state  $T_1$  and the  $S_1$  state. On the other hand, the distinctly nonmono-exponential decay, as found at  $T = 1.5\text{ K}$  (Figure 3.9a), displays a nonthermalized situation, as will be explained below. Slight deviations from a strict mono-exponential decay in the temperature range  $\approx 40\text{ K} \leq T \leq \approx 100\text{ K}$  are a consequence of slight  $\Delta E(S_1-T_1)$  inhomogeneities that are observable in the range of drastic  $\tau$  decrease as seen in Figure 3.10.

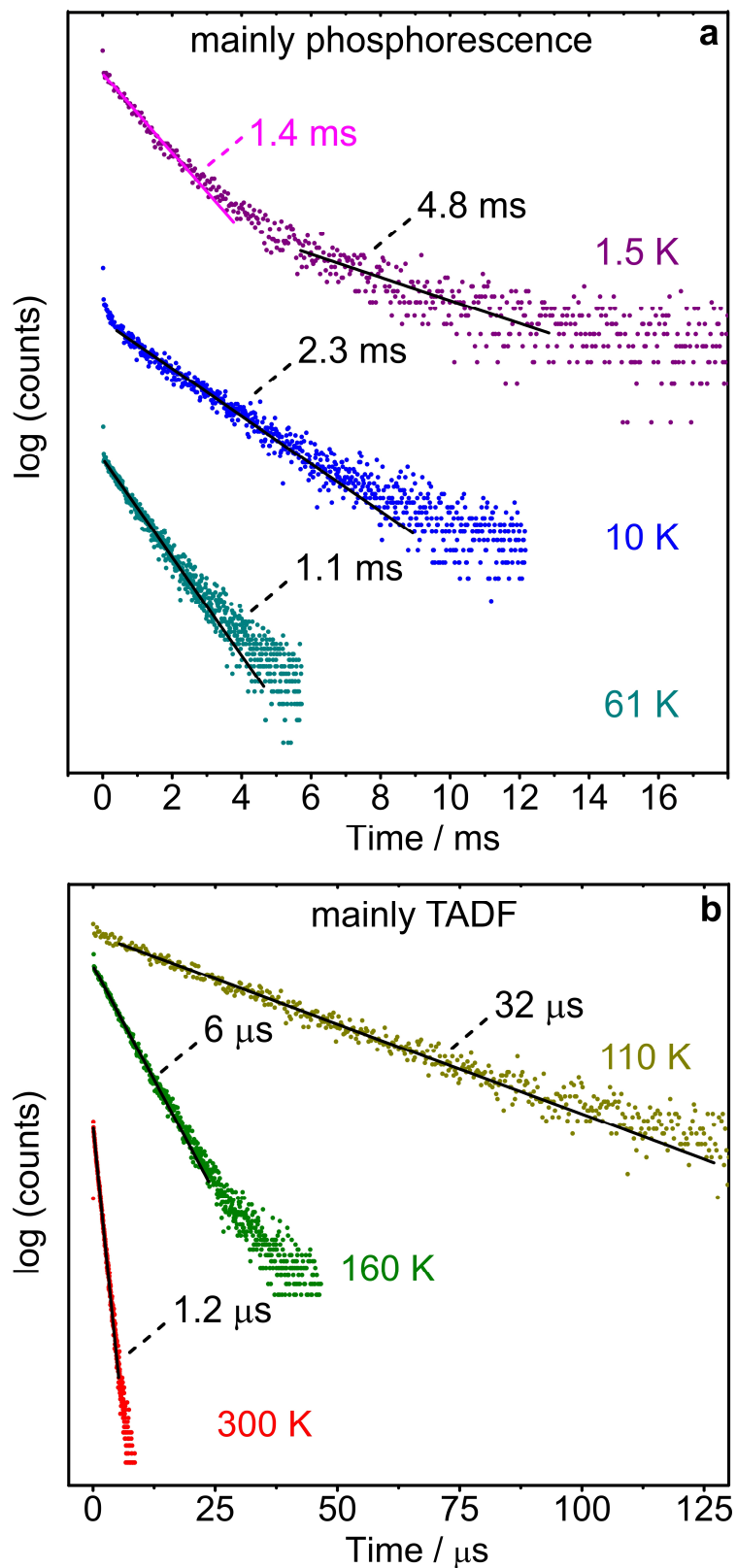


**Figure 3.9:** Emission decay curves and decay times of  $\text{Cu}_2(\text{tppb})(\text{PPh}_3)_2\text{Cl}_2$  **6** powder at different temperatures.  $\lambda_{\text{exc}} = 378$  nm,  $\lambda_{\text{det}} = 570$  nm, and excitation pulse width  $< 100$  ps for all decay curves. Note the different time scales in both figures.

Figure 3.10 reproduces a plot of the experimentally determined emission decay times  $\tau(T)$  versus temperature. In the temperature range  $\approx 10 \text{ K} \leq T \leq 40 \text{ K}$ , a plateau is observed with  $\tau = 2.3 \text{ ms}$  characterized by the  $T_1$  phosphorescence. In this range, no other emitting state is involved. This decay time belongs to the longest values compared to other Cu(I) complexes reported so far.<sup>36,37,49,98</sup> Accordingly, the triplet state  $T_1$  experiences only very weak SOC to higher lying singlet state(s). Indeed, according to the TD-DFT calculations (SI section 3 of ref. 38), the nearest state that exhibits a different d-orbital occupation than the state  $S_1$ , being the  $S_3$  state, is energetically not very proximate ( $\approx 490 \text{ meV}$ ,  $\approx 3900 \text{ cm}^{-1}$ ) and furthermore, it carries only very low oscillator strength ( $f = 0.00068$ , Table SI-9 of ref. 38). Thus, a quantum mechanical admixture of  $S_3$  to  $T_1$  has only insignificant consequences. With temperature increase above  $T \approx 40 \text{ K}$ , the decay time decreases drastically according to the population of the energetically higher lying  $S_1$  state and, finally, at ambient temperature leads to an emission decay time of  $\tau(300 \text{ K}) = 1.2 \text{ }\mu\text{s}$  ( $\tau^r(300 \text{ K}) = 1.5 \text{ }\mu\text{s}$ ). The corresponding emission represents almost completely an  $S_1 \rightarrow S_0$  TADF emission.

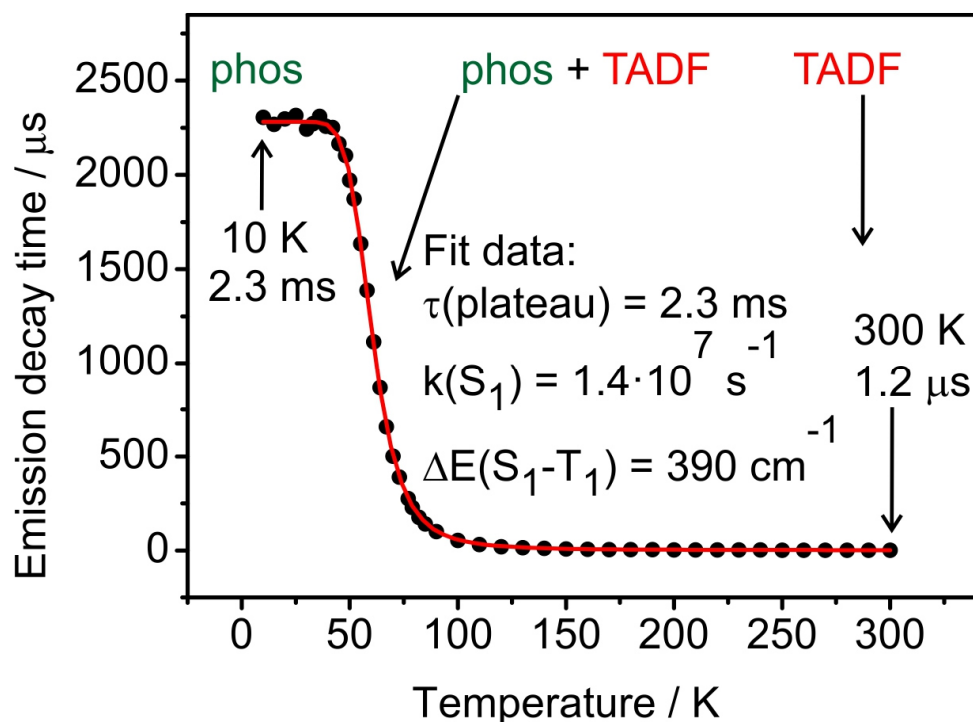


**Figure 3.10:** Temperature dependence of the emission decay time of  $\text{Cu}_2(\text{tppb})(\text{PPh}_3)_2\text{Cl}_2$  **6** powder. The solid red line represents a fit of eq. (3.1) to the experimental data.

The experimental data set, as displayed in Figure 3.10, can be fitted by a Boltzmann-type equation (eq. (3.1)) to elucidate important molecular parameters<sup>36,37</sup>

$$\tau(T) = \frac{3 + \exp\left[-\frac{\Delta E(S_1 - T_1)}{k_B T}\right]}{3k(T_1) + k(S_1) \cdot \exp\left[-\frac{\Delta E(S_1 - T_1)}{k_B T}\right]} \quad (3.1)$$

Herein,  $\tau(T)$  is the measured emission decay time at a given temperature.  $\Delta E(S_1-T_1)$  is the activation energy from the  $T_1$  state to the  $S_1$  state.  $k(T_1)$  and  $k(S_1)$  are the rates of the transitions to the  $S_0$  state and  $k_B$  is the Boltzmann constant. For this two-level approach, it is assumed that the splitting of the  $T_1$  state into three substates can be ignored (but see below in this section).

The fit of eq. (3.1) to the measured decay times is remarkably good. Accordingly, important molecular parameters for compound **6** can be determined, as summarized in Figure 3.10. In particular, the activation energy is determined to  $\Delta E(S_1-T_1) = 390 \text{ cm}^{-1}$  (48 meV). This value belongs to the smallest values reported for Cu(I) complexes so far.<sup>16,17,36,37,49,98</sup> It is smaller than found for the monomer **5** with a splitting of  $490 \text{ cm}^{-1}$ , being even in line with the prediction of our simple guiding model. The rate for the  $S_1 \rightarrow S_0$  transition is found to  $k(S_1) = 1.4 \cdot 10^7 \text{ s}^{-1}$  (71 ns). A corresponding prompt fluorescence is not observed with our ns time resolution, since the  $S_1$  to  $T_1$  ISC time is by more than three orders of magnitude faster.<sup>32,85,105</sup> By use of the relation of  $k^r = \Phi_{\text{PL}} \cdot k$  and with  $\Phi_{\text{PL}}(300 \text{ K}) = 80 \%$ , the radiative rate can be estimated to  $k^r(S_1 \rightarrow S_0) = 1.13 \cdot 10^7 \text{ s}^{-1}$ . This value is by a factor of about six times faster than found for the monomer and, thus, even slightly exceeds the value predicted by the guiding model. This result is very advantageous having the designing aim of developing a material with short TADF decay time in mind. (See also below.)

For completeness, the emission decay behavior at  $T = 1.5 \text{ K}$  will be discussed shortly. (Figure 3.9a) At this temperature, the decay properties are characteristic of the individually emitting triplet substates I, II, and III, if they experience only very weak SOC to higher lying singlets and triplets.<sup>36,37,106,107</sup> Hence, long emission decay times and small zero-field splittings of  $\Delta E(\text{ZFS}) \ll 1 \text{ cm}^{-1}$  ( $\ll 0.1 \text{ meV}$ ) are found.<sup>107,142</sup> In particular, at such small  $\Delta E(\text{ZFS})$  values, relaxation between the triplet substates is slow at low temperature.<sup>17,35,50,87,106,107,142</sup> This is the reason, why individual triplet sublevels decays with  $\tau(\text{I})$ ,  $\tau(\text{II})$ , and  $\tau(\text{III})$  occur. However, with temperature increase, for example, to  $T = 10 \text{ K}$ , the relaxation becomes fast with respect to the substate decay times. For the dimer compound **6** (and also for the monomer compound **5**), the relevant mechanism is presumably the Raman effect of spin-lattice relaxation (SLR).<sup>32,101,106,143</sup> Thus, in the equilibrated situation, one observes an average decay time  $\tau_{\text{av}}$  according to eq.(1.2)<sup>32,104</sup>  $\tau_{\text{av}}$  can be identified with the emission decay time of 2.3 ms corresponding to the low-temperature plateau. (Figure 3.10) If the two decay components observed at  $T = 1.5 \text{ K}$  of 1.4 ms and 4.8 ms (Figure 3.9a) are further identified to two individual triplet substate decay times, it is possible to estimate the third decay time to 2.6 ms.

The presented discussion shows that the triplet state phosphorescence behavior of the dimer **6** is largely the same as found for the monomer **5**. Apparently, the interaction of the two molecular moieties in the dimer has almost no influence on SOC experienced by the lowest triplet substates. This is due to almost vanishing two-center integrals. Obviously, this behavior is in contrast to the situation for the singlet states.

In Figure 3.11, the photophysical properties of compound **6** are summarized as discussed above.

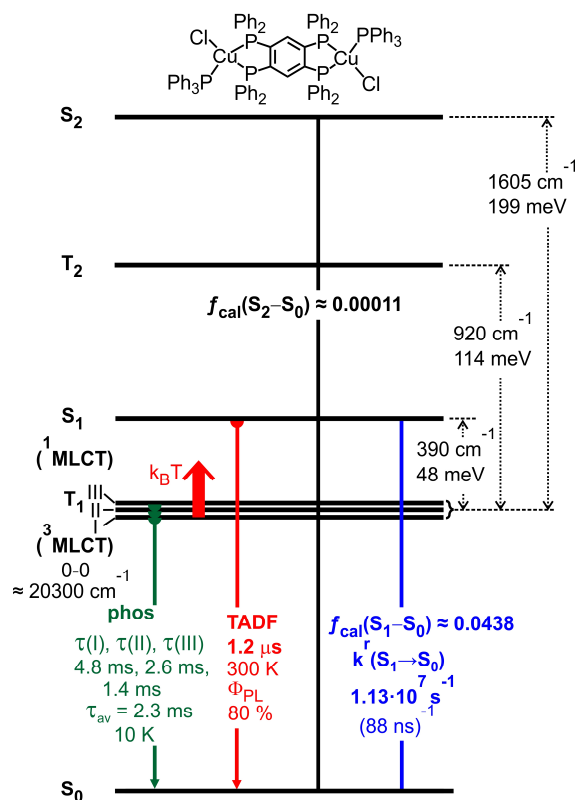


**Figure 3.11:** Schematic energy level diagram with state-related decay rates or times of  $\text{Cu}_2(\text{tppb})(\text{PPh}_3)_2\text{Cl}_2$  **6** powder. Note, the higher lying states  $S_2$  and  $T_2$  (Table 3.1) are energetically too far to be directly involved in the emission process. The 0-0 energy of the  $T_1 \rightarrow S_0$  transition is estimated from the blue flank of the 10 K emission spectrum. (Figure 3.8) The individual decay times of the triplet substates I, II, and III have been determined from the 1.5 K decay curve (Figure 3.9a).  $\tau_{\text{av}}$  is the average decay time that refers to the emission decay plateau found for  $\approx 10 \text{ K} \leq T \leq 40 \text{ K}$ .

### 3.5 Comparison of photophysical properties of the different dimers studied

Photophysical investigations were carried out for all four dimer complexes by methods as described in the previous sections. The resulting data are summarized in Table 3.2.

**Table 3.2:** Summary of photophysical data of the powder materials **6 - 9**. (For further data see Table SI-16 of ref. 38.)

	Cu <sub>2</sub> (tppb)(PPh <sub>3</sub> ) <sub>2</sub> Cl <sub>2</sub> <b>6</b> powder	Cu <sub>2</sub> (tppb)(PPh <sub>3</sub> ) <sub>2</sub> Br <sub>2</sub> <b>7</b> powder	Cu <sub>2</sub> (tppb)(PPh <sub>3</sub> ) <sub>2</sub> I <sub>2</sub> <b>8</b> powder	Cu <sub>2</sub> (tppb)(PPh <sub>3</sub> ) <sub>2</sub> (NCS) <sub>2</sub> <b>9</b> powder
$\lambda_{\max}(300\text{ K}) / \text{nm}$	577	569	562	564
$\Phi_{\text{PL}}(300\text{ K}) / \%$	80	80	82	84
$\tau(300\text{ K}) / \mu\text{s}$	1.2	1.4	1.2	1.3
$k^{\text{r}}(300\text{ K}) / \text{s}^{-1}$	$6.7 \cdot 10^5$	$5.7 \cdot 10^5$	$6.8 \cdot 10^5$	$6.5 \cdot 10^5$
$k^{\text{nr}}(300\text{ K})^{\text{a}} / \text{s}^{-1}$	$1.7 \cdot 10^5$	$1.4 \cdot 10^5$	$1.5 \cdot 10^5$	$1.2 \cdot 10^5$
$\lambda_{\max}(10\text{ K}) / \text{nm}$	596	571	567	581
$\Phi_{\text{PL}}(77\text{ K}) / \%$	95	90	90	94
$\tau(77\text{ K}) / \mu\text{s}$	275	200/2300 <sup>d</sup>	98	170
$\tau(\text{plateau}, 10/15\text{ K})^{\text{b}} / \text{ms}$	2.3	- <sup>e</sup>	0.19	2.6
$k^{\text{r}}(\text{plateau}, 10/15\text{ K})^{\text{c}} / \text{s}^{-1}$	$4.2 \cdot 10^2$	- <sup>e</sup>	$4.7 \cdot 10^3$	$3.6 \cdot 10^2$
$k_1^{\text{nr}}(\text{plateau}, 10/15\text{ K})^{\text{a,c}} / \text{s}^{-1}$	$0.22 \cdot 10^2$	- <sup>e</sup>	$5.3 \cdot 10^2$	$0.23 \cdot 10^2$
$\Delta E(\text{S}_1 - \text{T}_1)^{\text{b}} / \text{cm}^{-1}$	390	- <sup>e</sup>	370	370
$k^{\text{r}}(\text{S}_1 \rightarrow \text{S}_0)^{\text{b}} / \text{s}^{-1}$	$11.3 \cdot 10^6$	- <sup>e</sup>	$12.3 \cdot 10^6$	$15.1 \cdot 10^6$

- The non-radiative rate is expressed by  $k^{\text{nr}} = (1 - \Phi_{\text{PL}})/\tau$ .
- Obtained from a fit using eq.(1).
- For this approach, it is assumed that  $\Phi_{\text{PL}}(10\text{ K}) \approx \Phi_{\text{PL}}(77\text{ K}, \text{measured})$ .
- Bi-exponential decay.
- Strongly non-mono-exponential decay.

A comparison shows that all compounds emit at similar wavelengths with maxima between  $\lambda_{\text{max}} = 562$  and  $577$  nm and exhibit almost the same emission quantum yields at  $T = 300$  K between  $\Phi_{\text{PL}} = 80$  and  $84$  % and at  $77$  K between  $\Phi_{\text{PL}} = 90$  and  $95$  %. Also the relevant parameters that are responsible for the landmarkingly short  $\tau(\text{TADF})$  decay times, amounting to  $1.2$  to  $1.4$   $\mu\text{s}$ , are similar. In particular,  $\Delta E(\text{S}_1\text{-T}_1)$  values lie between  $370$   $\text{cm}^{-1}$  ( $46$  meV) and  $390$   $\text{cm}^{-1}$  ( $48$  meV). Also the radiative rates of the singlet  $\text{S}_1$  to the singlet  $\text{S}_0$  transition vary only slightly from  $k^{\text{r}}(\text{S}_1\rightarrow\text{S}_0) \approx 1.1 \cdot 10^7$  to  $1.5 \cdot 10^7$   $\text{s}^{-1}$  and, thus, are much faster than found for other Cu(I) complexes reported<sup>36,37,49</sup> that show similarly small  $\Delta E(\text{S}_1\text{-T}_1)$  values.

However, one parameter of this series deviates significantly. The phosphorescence decay time, measured at a temperature below about  $T = 40$  K ( $\tau(\text{plateau})$ , compare Figure 3.10), is by factor of more than ten shorter for the iodide complex (compound **8**) than for the other dimers. This is assigned to result from more effective SOC to the  $\text{T}_1$  state. The higher SOC may be induced by the iodide atom that shows a large SOC constant of  $\xi = 5069$   $\text{cm}^{-1}$ <sup>144</sup> compared, for example, to Cl with  $\xi = 587$   $\text{cm}^{-1}$ <sup>144</sup>. On the other hand, SOC may also be enhanced due to the smaller ligand field strength of the I- compared to the Cl-bond,<sup>99</sup> because this reduces the d-orbital splitting and, hence, the energy separation between the  $\text{T}_1$  state and that higher lying singlet state that is relevant for SOC ( $\text{S}_3$  state for compound **6**). A deeper discussion of this aspect is beyond the subject of the study.

### 3.6. Highlights of the guiding-model dimers

The Cu(I) dimers presented in this work show distinctly shorter TADF emission decay times than reported for most other Cu(I) compounds so far. This property is crucial if the OLED device lifetime or the roll-off behavior are addressed.<sup>125</sup> The TADF decay time depends essentially on  $\Delta E(\text{S}_1\text{-T}_1)$  and  $k^{\text{r}}(\text{S}_1\rightarrow\text{S}_0)$ . These parameters should be as small and as fast as possible, respectively. (Compare eq. (3.1)) In Table 3.3, important parameters for the monomer **5** and the related benchmark dimer **6** are compared.

**Table 3.3:** Summary and comparison of photophysical data of the monomer **5** and the dimer **6**

powder	Cu(dppb)(PPh <sub>3</sub> )Cl <b>5</b>	Cu <sub>2</sub> (tppb)(PPh <sub>3</sub> ) <sub>2</sub> Cl <sub>2</sub> <b>6</b>
$\lambda_{\max}$ (300 K)	548 nm	577 nm
$\Phi_{\text{PL}}$ (300 K)	58 %	80 %
$\tau$ (TADF, 300 K)	<b>6 <math>\mu\text{s}</math></b>	<b>1.2 <math>\mu\text{s}</math></b>
$k^{\text{r}}$ (TADF, 300 K)	$9.7 \cdot 10^4 \text{ s}^{-1}$	$67 \cdot 10^4 \text{ s}^{-1}$
$k^{\text{nr}}$ (300 K)	$7.0 \cdot 10^4 \text{ s}^{-1}$	$17 \cdot 10^4 \text{ s}^{-1}$
$\Delta E(\text{S}_1 - \text{T}_1)$	<b>490 <math>\text{cm}^{-1}</math></b>	<b>390 <math>\text{cm}^{-1}</math></b>
$k^{\text{r}}(\text{S}_1 \rightarrow \text{S}_0)$	<b><math>1.9 \cdot 10^6 \text{ s}^{-1}</math></b>	<b><math>11.3 \cdot 10^6 \text{ s}^{-1}</math></b>
$f_{\text{cal}}(\text{S}_1 - \text{S}_0)^{\text{a}}$	0.0127	0.0499
$\tau(\text{T}_1, 15 \text{ K})$	2.45 ms	2.3 ms

a. Calculated for the ground state  $\text{S}_0$  geometry; compare Tables SI-3 and SI-9 of ref. 38.

The guiding model predicts an increase of the important allowedness of the  $\text{S}_1 \rightarrow \text{S}_0$  transition by a factor of four (section 3.3). This is largely reproduced by TD-DFT calculations that indicate a factor of 3.9 increase, while the experimental value is even by a factor of about 6 larger. (Table 3.3) This tells us that the guiding model leads us to very valuable material design rules. However, the model should not be overestimated quantitatively. Interestingly, the singlet-triplet gap is also distinctly smaller for the dimer **6** with  $\Delta E(\text{S}_1 - \text{T}_1) = 390 \text{ cm}^{-1}$  than for the monomer **5** with a splitting of  $490 \text{ cm}^{-1}$ . This behavior is at least not in contradiction to the guiding model, because the singlet energy splitting of the dimer shifts the resulting lower lying singlet to lower energy towards the  $\text{T}_1$  state. In particular, these two parameters, the energy gap  $\Delta E(\text{S}_1 - \text{T}_1)$  and the radiative rate  $k^{\text{r}}(\text{S}_1 \rightarrow \text{S}_0)$ , highlighted in Table 3.3, are responsible for the very short TADF decay time of  $1.2 \mu\text{s}$  ( $\tau^{\text{r}}(\text{TADF}) = 1.5 \mu\text{s}$ ). For completeness, it is mentioned that the triplet  $\text{T}_1$  (phosphorescence) decay time is not altered distinctly if dimer and monomer are compared. Also this behavior is not in contradiction to the guiding model, since a significant interaction between the triplets or changes of the SOC strength are not expected. The observed increase of the emission quantum yield from  $\Phi_{\text{PL}}(\text{monomer}) = 58 \%$  to  $\Phi_{\text{PL}}(\text{dimer}) = 80 \%$  may be a consequence of the higher dimer transition rate at ambient temperature (factor  $\approx 7$ ) and the higher rigidity of the dimer structure in the crystalline environment as compared to the monomer structure.

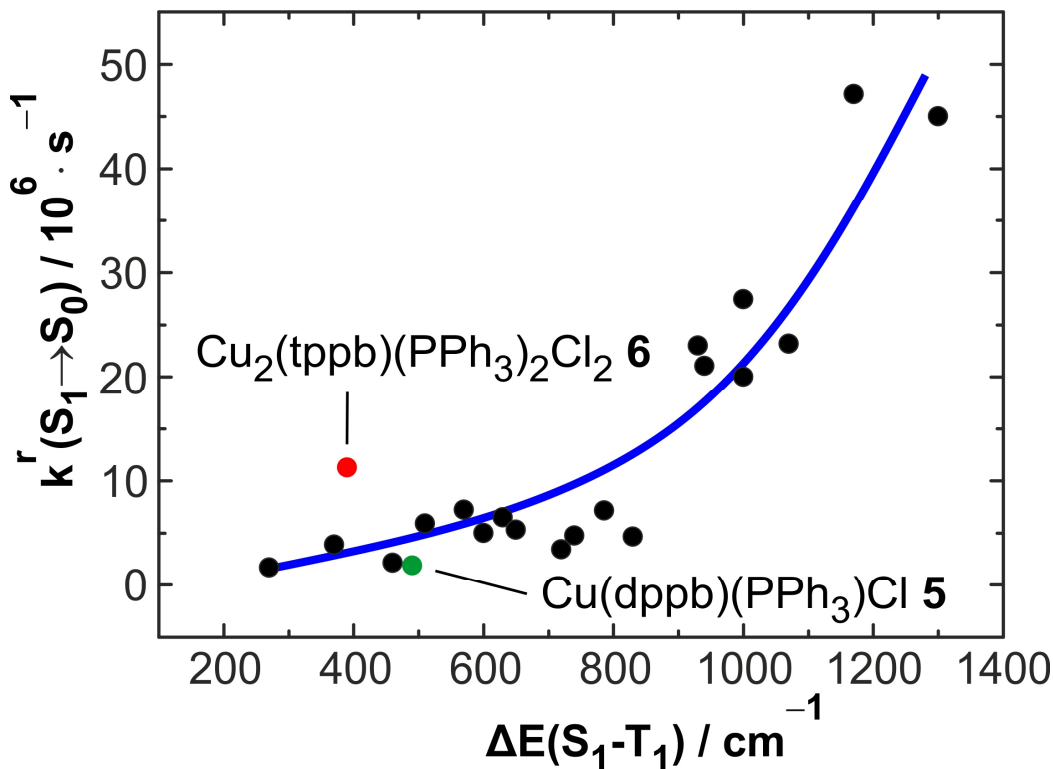


**Figure 3.12:** Radiative decay rate  $k^r(S_1 \rightarrow S_0)$  plotted versus the energy splitting  $\Delta E(S_1 - T_1)$  between the lowest excited singlet  $S_1$  and triplet  $T_1$  state. The black point data are reproduced from Table SI-17<sup>36</sup>. The green and red point data refer to the monomer **5** and the dimer **6**, respectively. The curve represents an exponential fit function to guide the eye.

Moreover, it is instructive to compare the properties of the dimer **6** to a trend which relates the energy separation  $\Delta E(S_1 - T_1)$  to the radiative rate of the  $S_1 \rightarrow S_0$  transition.<sup>36,37</sup> This trend, as displayed in Figure 3.12 for a large number of Cu(I) monomers and dimers, is related to simple quantum mechanical considerations. In a situation in which the  $S_1$  and  $T_1$  states are described by a transition from HOMO  $\varphi_H$  to LUMO  $\varphi_L$ , the radiative rate and the singlet-triplet splitting, respectively, can be expressed by:<sup>36,37,145,146</sup>

$$k^r(S_1 - S_0) \approx c_1 \left| \int \varphi_H(\vec{r}) \vec{r} \varphi_L(\vec{r}) d^3r \right|^2 \quad (3.3)$$

and

$$\Delta E(S_1 - T_1) \approx c_2 \int \varphi_H(\vec{r}_1) \varphi_L(\vec{r}_1) \frac{1}{|\vec{r}_2 - \vec{r}_1|} \varphi_H(\vec{r}_2) \varphi_L(\vec{r}_2) d^3r_1 d^3r_2 \quad (3.4)$$

Herein,  $c_1$  and  $c_2$  are constants,<sup>36</sup> and  $r$ ,  $r_1$ , and  $r_2$  are the electron coordinates.

Both  $k^r(S_1 \rightarrow S_0)$  and  $\Delta E(S_1-T_1)$  depend quadratically on the product of  $\phi_H(r) \cdot \phi_L(r)$ . Thus, the described trend, as found for all Cu(I) complexes described so far (Figure 3.12) becomes obvious. Small  $\Delta E(S_1-T_1)$  is related to slow  $k^r(S_1 \rightarrow S_0)$ . The monomer **5** properties follow just the trend as described in Figure 3.12 (green point).

Obviously, the data of the dimer **6** do not fit the general trend. For a given value of  $\Delta E(S_1-T_1) = 390 \text{ cm}^{-1}$ , the radiative rate is by a factor of about three faster than expected from the plot as shown in Figure 3.12 (red point). This significantly faster radiative rate, in particular, in the range of very small  $\Delta E(S_1-T_1)$ , leads to one of the shortest TADF decay time reported so far. A value of only  $\tau = 1.2 \text{ }\mu\text{s}$  ( $\tau^r = 1.5 \text{ }\mu\text{s}$ ) is found, thus, highlighting  $\text{Cu}_2(\text{tppb})(\text{PPh}_3)_2\text{Cl}_2$  **6** as a benchmark material.

### 3.7. Conclusion and outlook

It is a challenge to develop short-lived TADF emitters which are required for obtaining better OLED device stability and lower roll-off effects.<sup>125</sup> Frequently, it is assumed that reducing the energy gap  $\Delta E(S_1-T_1)$  will represent an adequate design method. However, a small gap is related to a small radiative rate  $k^r(S_1 \rightarrow S_0)$  and this sets a limit.<sup>36,37,126</sup> For example, as has been shown for Cu(I) complexes, monomers and dimers, the lowest radiative TADF decay time obtainable lies at around  $5 \text{ }\mu\text{s}$ .<sup>36,37</sup> In this chapter, it is shown that a new molecular design strategy allows to overcome this close relation between both molecular parameters and open a step towards shorter-lived TADF of Cu(I) compounds. The design concept, inspired by the Davidov model known from molecular crystal theory,<sup>129-132</sup> is applied here for the first time to TADF molecules. It is essentially based on the effects of couplings of symmetry-related transition dipole moments of the same molecule. The concept may be realized by two quasi-Cu(I)-monomer units that combine to a dimer. Accordingly, one finds two resulting combinations for the transition dipole moments. For example, if they are arranged in a parallel or anti-parallel way, the transition dipoles approximately cancel or add up to give about a twice as large resulting transition dipole moment. This is equivalent to a factor of about four times faster radiative rate  $k^r(S_1 \rightarrow S_0)$  of the dimer than that of the monomer. In this model, the triplet state properties of the dimer are largely similar to those of the monomer, while the gap  $\Delta E(S_1-T_1)$  of the resulting dimer may become even smaller than of the related monomer. Indeed, by designing new Cu(I) dimers according to our guiding model, it is demonstrated by TD-DFT calculations and experimental studies that this new design concept is highly successful. In particular, it guides to a Cu(I) dimer,  $\text{Cu}_2(\text{tppb})(\text{PPh}_3)_2\text{Cl}_2$  **6**, with a landmark short TADF decay time of only  $\tau = 1.2 \text{ }\mu\text{s}$  ( $\tau^r = 1.5 \text{ }\mu\text{s}$ ) being a factor of about three shorter than found for most other Cu(I) monomer or dimer. (For completeness, it is remarked that meanwhile another group<sup>118</sup> reported a similarly short decay time for a different Cu(I) compound.) Thus, the TADF decay time of this new Cu(I) dimer is as short as found for the

phosphorescence of the well-known Ir(ppy)<sub>3</sub> complex.<sup>12,16,17,21,23,147,148</sup> The design strategy presented could be used to increase the fluorescence rate at a small energy gap and can lead in future investigations to molecules that show TADF decay times even in a sub-microsecond range.

## Conclusion

In the last years the demand for OLED displays rose steadily and is expected to continue rising in the next years. Especially, in the mobile device sector, where power efficiency is important, OLED displays are superior to displays with liquid crystal technology. However, there is always a demand for even more efficient emitter materials and lower production costs. In this thesis, it was shown that copper complexes prove to be promising materials to meet these criteria. Due to their special electronic properties, all induced excitations formed may be used for light generation due to the singlet harvesting effect or even with a combined singlet and triplet harvesting effect.

For a deeper understanding of the desired effects, a detailed investigation of the triplet state properties, including the influence of SOC, was performed. Important is also a more detailed understanding of the structure-property relation. Insights were achieved by fine-tuning emission properties by variation of steric rigidity.

Furthermore, a deep blue emitter with an outstanding photoluminescence quantum yield of  $\Phi_{\text{PL}} = 76\%$  in solution was studied.

Also, it was shown that Cu(I) complexes are able to show radiative emission decay times of around 1  $\mu\text{s}$ ,<sup>38,118</sup> which is among the shortest radiative emission decay times published in literature so far.

Thus, this thesis presents the successful design of new Cu(I) complexes with desired properties of high quantum yields and short emission decay times. It also contributes to a deeper understanding of the structure-property relationship and therefore, may serve as a contribution for further research.

## Experimental

Experimental details as being relevant for the investigation of all compounds studied in this thesis have been published in ref. 59.

For measuring UV-Vis absorption spectra, a Varian Cary 300 double beam spectrometer was used. The photoluminescence quantum yields at 300 K and 77 K, respectively, were determined with a C9920-02 system of Hamamatsu Photonics. For measuring of emission spectra, a Fluorolog 3-22 system (Horiba Jobin Yvon) with a cooled photomultiplier for noise reduction was used. Emission decay times were determined by using a multichannel scaler PCI card from FAST ComTec (time resolution 250 ps) in combination with a pulsed diode laser (Picobrite PB-375L) with an excitation wavelength of  $\lambda_{\text{exc}} = 378$  nm (pulse width  $< 100$  ps). Measurements at lower temperatures were carried out in a cryostat (Cryovac Konti Cryostat IT) in which the temperature is adjustable by liquid helium flux and heating. (With the exception of the 77 K emission spectrum and emission decay curve shown in figure 1.3 and 1.4, respectively, which were measured in a dewar filled with liquid nitrogen.)

## References

- (1) [https://www.umweltbundesamt.de/sites/default/files/medien/376/publikationen/nanotechnology-based\\_lighting\\_systems\\_organic\\_light-emitting\\_diode\\_oled\\_datenblatt.pdf](https://www.umweltbundesamt.de/sites/default/files/medien/376/publikationen/nanotechnology-based_lighting_systems_organic_light-emitting_diode_oled_datenblatt.pdf) (July 12, 2020).
- (2) Singh, M.; Jou, J.-H.; Sahoo, S.; S. S, S.; He, Z.-K.; Krucaite, G.; Grigalevicius, S.; Wang, C.-W. High light-quality OLEDs with a wet-processed single emissive layer. *Sci. Rep.* **2018**, *8*, 7133.
- (3) [http://www.novaled.com/oleds/oleds\\_in\\_lighting/](http://www.novaled.com/oleds/oleds_in_lighting/) (July 12, 2020).
- (4) Krigel, A.; Berdugo, M.; Picard, E.; Levy-Boukris, R.; Jaadane, I.; Jonet, L.; Dernigoghossian, M.; Andrieu-Soler, C.; Torriglia, A.; Behar-Cohen, F. Light-induced Retinal Damage Using Different Light Sources, Protocols and Rat Strains Reveals LED Phototoxicity. *Neuroscience* **2016**, *339*, 296-307.
- (5) <https://www.oled-info.com/oled-introduction> (July 12, 2020).
- (6) <https://www.lg.com/us/tvs/lg-OLED88Z9PUA-signature-oled-8k-tv> (July 12, 2020).
- (7) <https://www.displaysupplychain.com/blog/dscs-latest-long-term-oled-forecast-in-oled-shipment-fab-utilization-report> (July 12, 2020).
- (8) Round, H. J. A note on carborundum. *Elect. World* **1907**, *49*, 309.
- (9) Pope, M.; Kallmann, H. P.; Magnante, P. Electroluminescence in Organic Crystals. *J. Chem. Phys.* **1963**, *38*, 2042-2043.
- (10) Tang, C. W.; VanSlyke, S. A. Organic electroluminescent diodes. *Appl Phys Lett* **1987**, *51*, 913-915.
- (11) Yersin, H. Triplet Emitters for OLED Applications. Mechanisms of Exciton Trapping and Control of Emission Properties. *Top. Curr. Chem.* **2004**, *241*, 1-26.
- (12) Yersin, H.; Finkenzeller, W. J., Triplet Emitters for Organic Light-Emitting Diodes: Basic Properties. In *Highly Efficient OLEDs with Phosphorescent Materials*, Yersin, H., Ed. Wiley-VCH Verlag: 2008; pp 1-97.
- (13) Shinar, J., ed. *Organic Light-Emitting Devices: A Survey*. Springer: New York, NY, United States, 2004.
- (14) Baldo, M. A.; O'Brien, D. F.; You, Y.; Shoustikov, A.; Sibley, S.; Thompson, M. E.; Forrest, S. R. Highly efficient phosphorescent emission from organic electroluminescent devices. *Nature* **1998**, *395*, 151-154.
- (15) Ma, Y.; Zhang, H.; Shen, J.; Che, C.-M. Electroluminescence from Triplet Metal-Ligand Charge-Transfer Excited State of Transition Metal Complexes. *Synth. Met.* **1998**, *94*, 245-248.
- (16) Yersin, H.; Rausch, A. F.; Czerwieńiec, R., Organometallic Emitters for OLEDs: Triplet Harvesting, Singlet Harvesting, Case Structures, and Trends. In *Physics of Organic Semiconductors*, Brütting, W., Adachi, C., Eds. Wiley-VCH Verlag: 2012; pp 371-424.
- (17) Yersin, H.; Rausch, A. F.; Czerwieńiec, R.; Hofbeck, T.; Fischer, T. The triplet state of organo-transition metal compounds. Triplet harvesting and singlet harvesting for efficient OLEDs. *Coord. Chem. Rev.* **2011**, *255*, 2622-2652.

- (18) Baldo, M. A.; Lamansky, S.; Burrows, P. E.; Thompson, M. E.; Forrest, S. R. Very high-efficiency green organic light-emitting devices based on electrophosphorescence. *Appl. Phys. Lett* **1999**, *75*, 4-6.
- (19) Reddy, M. L. P. L.; K S, B. M. D.; Kumar, A.; Varughese, S.; Varathan, E.; Subramanian, V. Photophysical and electroluminescent properties of bis(2',6'-difluoro-2,3'-bipyridinato-N,C4')iridium(picolate) complexes: Effect of electron-withdrawing and electron-donating group substituent at the 4' position on the pyridyl moiety of the cyclometalated ligand. *J. Mater. Chem. C* **2015**, *3*, 7405-7420.
- (20) Zhou, Y.; Li, W.; Yu, L.; Liu, Y.; Wang, X.; Zhou, M. Highly efficient electrochemiluminescence from iridium(III) complexes with 2-phenylquinoline ligand. *Dalton Trans.* **2015**, *44*, 1858-1865.
- (21) Deaton, J. C.; Castellano, F. N., Archetypal Iridium(III) Compounds for Optoelectronic and Photonic Applications: Photophysical Properties and Synthetic Methods. In *Optoelectronic and Photonics Applications*, Zysman-Colman, E., Ed. Wiley-VCH, Weinheim: 2017; pp 1-69.
- (22) Rausch, A. F.; Homeier, H. H. H.; Yersin, H. Organometallic Pt(II) and Ir(III) Triplet Emitters for OLED Applications and the Role of Spin-Orbit Coupling: A Study Based on High-Resolution Optical Spectroscopy. *Top. Organomet. Chem.* **2010**, *29*, 193-235.
- (23) Hofbeck, T.; Yersin, H. The Triplet State of *fac*-Ir(ppy)<sub>3</sub>. *Inorg. Chem.* **2010**, *49*, 9290-9299.
- (24) Li, G.; Fleetham, T.; Turner, E.; Hang, X.-C.; Li, J. Highly Efficient and Stable Narrow-Band Phosphorescent Emitters for OLED Applications. *Adv. Optical Mater.* **2015**, *3*, 390-397.
- (25) Solomatina, A. I.; Krupenya, D. V.; Gurzhiy, V. V.; Zlatkin, I.; Pushkarev, A. P.; Bochkarev, M. N.; Besley, N. A.; Bichoutskaia, E.; Tunik, S. P. Cyclometallated platinum(II) complexes containing NHC ligands: synthesis, characterization, photophysics and their application as emitters in OLEDs. *Dalton Trans.* **2015**, *44*, 7152-7162.
- (26) Yang, X.; Yao, C.; Zhou, G. Highly Efficient Phosphorescent Materials Based on Platinum Complexes and Their Application in Organic Light-Emitting Devices (OLEDs). *Platinum Metals Rev.* **2013**, *57*, 2-16.
- (27) Li, G.; Fleetham, T.; Li, J. Efficient and Stable White Organic Light-Emitting Diodes Employing a Single Emitter. *Adv. Mater.* **2014**, *26*, 2931-2936.
- (28) Fleetham, T.; Li, G.; Wen, L.; Li, J. Efficient "Pure" Blue OLEDs Employing Tetradentate Pt Complexes with a Narrow Spectral Bandwidth. *Adv. Mater.* **2014**, *26*, 7116-7121.
- (29) Kui, S. C. F.; Chow, P. K.; Cheng, G.; Kwok, C.-C.; Kwong, C. L.; Low, K.-H.; Che, C.-M. Robust phosphorescent platinum(II) complexes with tetradentate O<sup>N</sup>C<sup>N</sup> ligands: high efficiency OLEDs with excellent efficiency stability. *Chem. Commun.* **2013**, *49*, 1497-1499.
- (30) Cheng, G.; Chow, P.-K.; Kui, S. C. F.; Kwok, C.-C.; Che, C.-M. High-Efficiency Polymer Light-Emitting Devices with Robust Phosphorescent Platinum(II) Emitters Containing Tetradentate Dianionic O<sup>N</sup>C<sup>N</sup> Ligands. *Adv. Mater.* **2013**, *25*, 6765-6770.

- (31) Hang, X.-C.; Fleetham, T.; Turner, E.; Brooks, J.; Li, J. Highly Efficient Blue-Emitting Cyclometalated Platinum(II) Complexes by Judicious Molecular Design. *Angew. Chem. Int. Edit.* **2013**, *52*, 6753-6756.
- (32) Yersin, H.; Donges, D. Low-Lying Electronic States and Photophysical Properties of Organometallic Pd(II) and Pt(II) Compounds. Modern Research Trends Presented in Detailed Case Studies. *Top. Curr. Chem.* **2001**, *214*, 81-186.
- (33) Yersin, H.; Monkowius, U. Komplexe mit kleinen Singulett-Triplett-Energie-Abständen zur Verwendung in opto-elektronischen Bauteilen (Singulett-Harvesting-Effekt). Internal patent filing, University of Regensburg 2006. German Patent DE 10 2008 033563 A1. 2008.
- (34) Yersin, H., ed. *Highly efficient OLEDs – Materials based on Thermally Activated Delayed Fluorescence*. Wiley-VCH, Weinheim, Germany, 2019; DOI: 10.1002/9783527691722.
- (35) Czerwieniec, R.; Yu, J.; Yersin, H. Blue-Light Emission of Cu(I) Complexes and Singlet Harvesting. *Inorg. Chem.* **2011**, *50*, 8293-8301.
- (36) Yersin, H.; Czerwieniec, R.; Shafikov, M. Z.; Suleymanova, A. F. TADF Material Design: Photophysical Background and Case Studies Focusing on Cu<sup>I</sup> and Ag<sup>I</sup> Complexes. *ChemPhysChem* **2017**, *18*, 3508-3535.
- (37) Czerwieniec, R.; Leidl, M. J.; Homeier, H. H. H.; Yersin, H. Cu(I) complexes – Thermally activated delayed fluorescence. Photophysical approach and material design. *Coord. Chem. Rev.* **2016**, *325*, 2-28.
- (38) Schinabeck, A.; Chen, J.; Kang, L.; Teng, T.; Homeier, H. H. H.; Suleymanova, A. F.; Shafikov, M. Z.; Yu, R.; Lu, C.-Z.; Yersin, H. Symmetry-Based Design Strategy for Unprecedentedly Fast Decaying Thermally Activated Delayed Fluorescence (TADF). Application to Dinuclear Cu(I) Compounds. *Chem. Mater.* **2019**, 4392-4404.
- (39) Bizzarri, C.; Hundemer, F.; Busch, J.; Bräse, S. Triplet Emitters vs TADF Emitters in OLEDs: a comparative study. *Polyhedron* **2018**, *140*, 51-66.
- (40) Artem'ev, A. V.; Ryzhikov, M. R.; Taidakov, I. V.; Rakhmanova, M. I.; Varaksina, E. A.; Bagryanskaya, I. Y.; Malysheva, S. F.; Belogorlova, N. A. Bright green-to-yellow emitting Cu(I) complexes based on bis(2-pyridyl)phosphine oxides: synthesis, structure and effective thermally activated-delayed fluorescence. *Dalton Trans.* **2018**, *47*, 2701-2710.
- (41) Osawa, M.; Hoshino, M.; Hashimoto, M.; Kawata, I.; Igawa, S.; Yashima, M. Application of three-coordinate copper(I) complexes with halide ligands in organic light-emitting diodes that exhibit delayed fluorescence. *Dalton Trans.* **2015**, *44*, 8369-8378.
- (42) Tsuge, K.; Chishina, Y.; Hashiguchi, H.; Sasaki, Y.; Kato, M.; Ishizaka, S.; Kitamura, N. Luminescent copper(I) complexes with halogenido-bridged dimeric core. *Coord. Chem. Rev.* **2016**, *306*, Part 2, 636-651.
- (43) Ohara, H.; Kobayashi, A.; Kato, M. Effects of N-heteroaromatic ligands on highly luminescent mononuclear copper(I)-halide complexes. *C. R. Chim.* **2015**, *18*, 766-775.
- (44) Kato, M.; Ohara, H.; Kobayashi, A. Simple and Extremely Efficient Blue Emitters Based on Mononuclear Cu(I)-Halide Complexes with Delayed Fluorescence. *Dalton Trans.* **2014**, *43*, 17317-17323.

- (45) Igawa, S.; Hashimoto, M.; Kawata, I.; Yashima, M.; Hoshino, M.; Osawa, M. Highly efficient green organic light-emitting diodes containing luminescent tetrahedral copper(I) complexes. *J. Mater. Chem. C* **2013**, *1*, 542-551.
- (46) Gneuß, T.; Leitl, M. J.; Finger, L. H.; Rau, N.; Yersin, H.; Sundermeyer, J. A new class of luminescent Cu(I) complexes with tripodal ligands - TADF emitters for the yellow to red color range. *Dalton Trans.* **2015**, *44*, 8506-8520.
- (47) Gneuß, T.; Leitl, M. J.; Finger, L. H.; Yersin, H.; Sundermeyer, J. A new class of deep-blue emitting Cu(I) compounds - effects of counter ions on the emission behavior. *Dalton Trans.* **2015**, *44*, 20045-20055.
- (48) Gneuß, T.; Leitl, M. J.; Sundermeyer, J.; Yersin, H. Metallkomplexverbindungen mit Tripod-Liganden für verbessertes Singulett-Harvesting durch kombinierte Singulett- und Triplett-Emission für OLEDs und andere optoelektronische Vorrichtungen. Internal patent filing, University of Regensburg 2014. German Patent DE 10 2014 116314 A. 2014.
- (49) Leitl, M. J.; Zink, D. M.; Schinabeck, A.; Baumann, T.; Volz, D.; Yersin, H. Copper(I) Complexes for Thermally Activated Delayed Fluorescence: From Photophysical to Device Properties. *Top. Curr. Chem.* **2016**, *374*, 1-34.
- (50) Leitl, M. J.; Kühle, F. R.; Mayer, H. A.; Wesemann, L.; Yersin, H. Brightly Blue and Green Emitting Cu(I) Dimers for Singlet Harvesting in OLEDs. *J. Phys. Chem. A* **2013**, *117*, 11823-11836.
- (51) Chen, X.-L.; Yu, R.; Wu, X.-Y.; Liang, D.; Jia, J.-H.; Lu, C.-Z. A strongly greenish-blue-emitting Cu<sub>4</sub>Cl<sub>4</sub> cluster with an efficient spin-orbit coupling (SOC): fast phosphorescence *versus* thermally activated delayed fluorescence. *Chem. Commun.* **2016**, *52*, 6288-6291.
- (52) Linfoot, C. L.; Leitl, M. J.; Richardson, P.; Rausch, A. F.; Chepelin, O.; White, F. J.; Yersin, H.; Robertson, N. Thermally Activated Delayed Fluorescence (TADF) and Enhancing Photoluminescence Quantum Yields of [Cu<sup>I</sup>(diimine)(diphosphine)]<sup>+</sup> Complexes-Photophysical, Structural, and Computational Studies. *Inorg. Chem.* **2014**, *53*, 10854-10861.
- (53) Schinabeck, A.; Leitl, M. J.; Yersin, H. Dinuclear Cu(I) Complex with Combined Bright TADF and Phosphorescence. Zero-Field Splitting and Spin-Lattice Relaxation Effects of the Triplet State. *J. Phys. Chem. Lett.* **2018**, *9*, 2848-2856.
- (54) Zink, D. M.; Volz, D.; Baumann, T.; Mydlak, M.; Flügge, H.; Friedrichs, J.; Nieger, M.; Bräse, S. Heteroleptic, Dinuclear Copper(I) Complexes for Application in Organic Light-Emitting Diodes. *Chem. Mater.* **2013**, *25*, 4471-4486.
- (55) Dumur, F. Recent advances in organic light-emitting devices comprising copper complexes: A realistic approach for low-cost and highly emissive devices? *Org. Electron.* **2015**, *21*, 27-39.
- (56) Yu, R.; Chen, X.-L.; Lu, C.-Z., Ionic [Cu(NN)(PP)]<sup>+</sup> TADF Complexes with Pyridine-Based Diimine Chelating Ligands and Their Use in OLEDs. In *Highly efficient OLEDs – Materials based on Thermally Activated Delayed Fluorescence*, Yersin, H., Ed. Wiley-VCH, Weinheim, Germany, 2019; DOI: 10.1002/9783527691722.
- (57) Deaton, J. C.; Switalski, S. C.; Kondakov, D. Y.; Young, R. H.; Pawlik, T. D.; Giesen, D. J.; Harkins, S. B.; Miller, A. J. M.; Mickenberg, S. F.; Peters, J. C. E-Type Delayed Fluorescence of a Phosphine-Supported Cu<sub>2</sub>(μ-NAr<sub>2</sub>)<sub>2</sub> Diamond Core:

Harvesting Singlet and Triplet Excitons in OLEDs. *J. Am. Chem. Soc.* **2010**, *132*, 9499–9508.

(58) So, G. K.-M.; Cheng, G.; Wang, J.; Chang, X.; Kwok, C.-C.; Zhang, H.; Che, C.-M. Efficient Color-Tunable Copper(I) Complexes and Their Applications in Solution-Processed Organic Light-Emitting Diodes. *Chem. Asian J.* **2017**, *12*, 1490-1498.

(59) Schinabeck, A.; Rau, N.; Klein, M.; Sundermeyer, J.; Yersin, H. Deep blue emitting Cu(I) tripod complexes. Design of high quantum yield materials showing TADF-assisted phosphorescence. *Dalton Trans.* **2018**, *47*, 17067-17076.

(60) Shafikov, M. Z.; Suleymanova, A. F.; Czerwieniec, R.; Yersin, H. Design Strategy for Ag(I)-Based Thermally Activated Delayed Fluorescence Reaching an Efficiency Breakthrough. *Chem. Mat.* **2017**, *29*, 1708-1715.

(61) Shafikov, M. Z.; Suleymanova, A. F.; Czerwieniec, R.; Yersin, H. Thermally Activated Delayed Fluorescence from Ag(I) Complexes: A Route to 100% Quantum Yield at Unprecedentedly Short Decay Time. *Inorg. Chem.* **2017**, *56*, 13274-13285.

(62) Shafikov, M. Z.; Suleymanova, A. F.; Schinabeck, A.; Yersin, H. Dinuclear Ag(I) Complex Designed for Highly Efficient Thermally Activated Delayed Fluorescence. *J. Phys. Chem. Lett.* **2018**, 702-709.

(63) Gan, X.-M.; Yu, R.; Chen, X.-L.; Yang, M.; Lin, L.; Wu, X.-Y.; Lu, C.-Z. A unique tetranuclear Ag(I) complex emitting efficient thermally activated delayed fluorescence with a remarkably short decay time. *Dalton Trans.* **2018**, *47*, 5956-5960.

(64) Chen, J.; Teng, T.; Kang, L.; Chen, X.-L.; Wu, X.-Y.; Yu, R.; Lu, C.-Z. Highly Efficient Thermally Activated Delayed Fluorescence in Dinuclear Ag(I) Complexes with a Bis-Bidentate Tetrphosphane Bridging Ligand. *Inorg. Chem.* **2016**, *55*, 9528-9536.

(65) Zhang, Q. S.; Li, B.; Huang, S. P.; Nomura, H.; Tanaka, H.; Adachi, C. Efficient blue organic light-emitting diodes employing thermally activated delayed fluorescence. *Nat. Photonics* **2014**, *8*, 326-332.

(66) Chin-Yiu, C.; Lin-Song, C.; Uk, K. J.; Hajime, N.; Adachi, C. Rational Molecular Design for Deep-Blue Thermally Activated Delayed Fluorescence Emitters. *Adv. Funct. Mater.* **2018**, *28*, 1706023.

(67) Uoyama, H.; Goushi, K.; Shizu, K.; Nomura, H.; Adachi, C. Highly Efficient Organic Light-Emitting Diodes from Delayed Fluorescence. *Nature* **2012**, *492*, 234-238.

(68) Sommer, G. A.; Mataranga-Popa, L. N.; Czerwieniec, R.; Hofbeck, T.; Homeier, H. H. H.; Müller, T. J. J.; Yersin, H. Design of Conformationally Distorted Donor–Acceptor Dyads Showing Efficient Thermally Activated Delayed Fluorescence. *J. Phys. Chem. Lett.* **2018**, *9*, 3692-3697.

(69) Yersin, H.; Mataranga-Popa, L.; Li, S.-W.; Czerwieniec, R. Design strategies for materials showing thermally activated delayed fluorescence and beyond: Towards the fourth-generation OLED mechanism. *J. Soc. Inf. Disp.* **2018**, *26*, 194-199.

(70) Komatsu, R.; Ohsawa, T.; Sasabe, H.; Nakao, K.; Hayasaka, Y.; Kido, J. Manipulating the Electronic Excited State Energies of Pyrimidine-Based Thermally Activated Delayed Fluorescence Emitters To Realize Efficient Deep-Blue Emission. *ACS Appl. Mater. Interfaces* **2017**, *9*, 4742-4749.

(71) Sharma, N.; Wong, M. Y.; Samuel, I. D. W.; Zysman-Colman, E., Solution Processed TADF Materials and Devices Based on Organic Emitters. In *Highly efficient*

- OLEDs – Materials based on Thermally Activated Delayed Fluorescence*, Yersin, H., Ed. Wiley-VCH, Weinheim, Germany, 2018; DOI: 10.1002/9783527691722.
- (72) Yokoyama, M.; Inada, K.; Tsuchiya, Y.; Nakanotani, H.; Adachi, C. Trifluoromethane modification of thermally activated delayed fluorescence molecules for high-efficiency blue organic light-emitting diodes. *Chem. Commun.* **2018**, *54*, 8261-8264.
- (73) Kim, D.-H.; D'Aléo, A.; Chen, X.-K.; Sandanayaka, A. D. S.; Yao, D.; Zhao, L.; Komino, T.; Zaborova, E.; Canard, G.; Tsuchiya, Y.; Choi, E.; Wu, J. W.; Fages, F.; Brédas, J.-L.; Ribierre, J.-C.; Adachi, C. High-efficiency electroluminescence and amplified spontaneous emission from a thermally activated delayed fluorescent near-infrared emitter. *Nat. Photonics* **2018**, *12*, 98-104.
- (74) [https://www.photonikforschung.de/media/organische-elektronik/pdf/5-bf-Psb\\_cyCESH-korr2016-05\\_bf\\_C1.pdf](https://www.photonikforschung.de/media/organische-elektronik/pdf/5-bf-Psb_cyCESH-korr2016-05_bf_C1.pdf) (July 12, 2020).
- (75) Leitl, M. J. Photophysical Characterizations of OLED Relevant Cu(I) Complexes Exhibiting Thermally Activated Delayed Fluorescence (TADF), Dissertation, Universität Regensburg. 2015.
- (76) Yersin, H.; Monkowius, U.; Fischer, T.; Hofbeck, T. German Patent DE 10 2009 030 475 A1. 2009.
- (77) Zink, D. M.; Baumann, T.; Friedrichs, J.; Nieger, M.; Brase, S. Copper(I) Complexes Based on Five-Membered P<sup>N</sup> Heterocycles: Structural Diversity Linked to Exciting Luminescence Properties. *Inorg. Chem.* **2013**, *52*, 13509-13520.
- (78) Hofbeck, T.; Monkowius, U.; Yersin, H. Highly Efficient Luminescence of Cu(I) Compounds: Thermally Activated Delayed Fluorescence Combined with Short-Lived Phosphorescence. *J. Am. Chem. Soc.* **2015**, *137*, 399-404.
- (79) Yersin, H.; Leitl, M.; Czerwieńiec, R.; Monkowius, U. Patent WO 2014 202675 A1. 2014.
- (80) Becke, A. D. Density-functional thermochemistry. III. The role of exact exchange. *J. Chem. Phys.* **1993**, *98*, 5648-5652.
- (81) Weigend, F.; Ahlrichs, R. Balanced basis sets of split valence, triple zeta valence and quadruple zeta valence quality for H to Rn: Design and assessment of accuracy. *Phys. Chem. Chem. Phys.* **2005**, *7*, 3297-3305.
- (82) Valiev, M.; Bylaska, E. J.; Govind, N.; Kowalski, K.; Straatsma, T. P.; Van Dam, H. J. J.; Wang, D.; Nieplocha, J.; Apra, E.; Windus, T. L.; de Jong, W. A. NWChem: A comprehensive and scalable open-source solution for large scale molecular simulations. *Comput. Phys. Commun.* **2010**, *181*, 1477-1489.
- (83) Blasse, G.; McMillin, D. R. On The Luminescence Of Bis(Triphenylphosphine) Phenanthroline Copper(I). *Chem. Phys. Lett.* **1980**, *70*, 1-3.
- (84) Yersin, H.; Leitl, M. J.; Czerwieńiec, R. TADF for singlet harvesting: next generation OLED materials based on brightly green and blue emitting Cu(I) and Ag(I) compounds. *Proc. SPIE* **2014**, *9183*, 91830N.
- (85) Iwamura, M.; Takeuchi, S.; Tahara, T. Ultrafast Excited-State Dynamics of Copper(I) Complexes. *Acc. Chem. Res.* **2015**, *48*, 782-791.
- (86) Vorontsov, I. I.; Graber, T.; Kovalevsky, A. Y.; Novozhilova, I. V.; Gembicky, M.; Chen, Y.-S.; Coppens, P. Capturing and Analyzing the Excited-State Structure of a Cu(I) Phenanthroline Complex by Time-Resolved Diffraction and Theoretical Calculations. *J. Am. Chem. Soc.* **2009**, *131*, 6566-6573.

- (87) Leitl, M. J.; Krylova, V. A.; Djurovich, P. I.; Thompson, M. E.; Yersin, H. Phosphorescence versus Thermally Activated Delayed Fluorescence. Controlling Singlet-Triplet Splitting in Brightly Emitting and Sublimable Cu(I) Compounds. *J. Am. Chem. Soc.* **2014**, *136*, 16032-16038.
- (88) Zhang, Q.; Chen, X.-L.; Chen, J.; Wu, X.-Y.; Yu, R.; Lu, C.-Z. Four highly efficient cuprous complexes and their applications in solution-processed organic light-emitting diodes. *RSC Adv.* **2015**, *5*, 34424-34431.
- (89) Wallesch, M.; Volz, D.; Zink, D. M.; Schepers, U.; Nieger, M.; Baumann, T.; Bräse, S. Bright Opportunities: Multinuclear Cu<sup>I</sup> Complexes with N-P Ligands and their Applications. *Chem. Eur. J.* **2014**, *20*, 6578-6590.
- (90) Hashimoto, M.; Igawa, S.; Yashima, M.; Kawata, I.; Hoshino, M.; Osawa, M. Highly Efficient Green Organic Light-Emitting Diodes Containing Luminescent Three-Coordinate Copper(I) Complexes. *J. Am. Chem. Soc.* **2011**, *133*, 10348-10351.
- (91) Osawa, M.; Hoshino, M., Molecular Design and Synthesis of Metal Complexes as Emitters for TADF-Type OLEDs. In *Highly efficient OLEDs – Materials based on Thermally Activated Delayed Fluorescence*, Yersin, H., Ed. Wiley-VCH, Weinheim, Germany, 2019; DOI: 10.1002/9783527691722.
- (92) Nozaki, K.; Iwamura, M., Highly Emissive d<sup>10</sup> Metal Complexes as TADF Emitters with Versatile structures and Photophysical Properties In *Highly efficient OLEDs – Materials based on Thermally Activated Delayed Fluorescence*, Yersin, H., Ed. Wiley-VCH, Weinheim, Germany, 2019; DOI: 10.1002/9783527691722.
- (93) Tsuboyama, A., Luminescent Dinuclear Copper(I) Complexes with Short Intramolecular Cu–Cu Distances. In *Highly efficient OLEDs – Materials based on Thermally Activated Delayed Fluorescence*, Yersin, H., Ed. Wiley-VCH, Weinheim, Germany, 2019; DOI: 10.1002/9783527691722.
- (94) Turro, N. J. *Modern molecular photochemistry*. Benjamin/Cummings Pub. Co.: 1978.
- (95) Atkins, P. W. *Quanta: A Handbook of Concepts*. Oxford University Press: Oxford, U.K.: 1991.
- (96) Barltrop, J. A.; Coyle, J. D. *Excited states in organic chemistry*. Wiley: New York: 1975.
- (97) El-Sayed, M. A. Spin—Orbit Coupling and the Radiationless Processes in Nitrogen Heterocyclics. *J. Chem. Phys.* **1963**, *38*, 2834-2838.
- (98) Czerwieńiec, R.; Yersin, H. Diversity of Copper(I) Complexes Showing Thermally Activated Delayed Fluorescence: Basic Photophysical Analysis. *Inorg. Chem.* **2015**, *54*, 4322-4327.
- (99) Zink, D. M.; Bächle, M.; Baumann, T.; Nieger, M.; Kuhn, M.; Wang, C.; Klopfer, W.; Monkowius, U.; Hofbeck, T.; Yersin, H.; Bräse, S. Synthesis, Structure, and Characterization of Dinuclear Copper(I) Halide Complexes with P<sup>N</sup> Ligands Featuring Exciting Photoluminescence Properties. *Inorg. Chem.* **2013**, *52*, 2292-2305.
- (100) Often, the decay behavior of powder materials is modified, for example, by processes of energy transfer or triplet-triplet annihilation. However, if the low-lying molecular states show distinct geometry distortions such as found for Cu(I) complexes, localization (self-trapping) can occur and prevent energy transfer effects. Thus, the emission of the powder material can essentially display the molecular properties.[17].
- (101) Yersin, H.; Humbs, W.; Strasser, J., Characterization of Excited Electronic and Vibronic States of Platinum Metal Compounds with Chelate Ligands by Highly

- Frequency-Resolved and Time-Resolved Spectra. In *Electronic and Vibronic Spectra of Transition Metal Complexes II*, Yersin, H., Ed. Springer Berlin Heidelberg: Berlin, Heidelberg, 1997; pp 153-249.
- (102) Azumi, T.; O'Donnell, C. M.; McGlynn, S. P. On the Multiplicity of the Phosphorescent State of Organic Molecules. *J. Chem. Phys.* **1966**, *45*, 2735-2742.
- (103) Niehaus, T. A.; Yersin, H. unpublished results.
- (104) Tinti, D. S.; El-Sayed, M. A. New Techniques in Triplet State Phosphorescence Spectroscopy: Application to the Emission of 2,3-Dichloroquinoxaline. *J. Chem. Phys.* **1971**, *54*, 2529-2549.
- (105) Bergmann, L.; Hedley, G. J.; Baumann, T.; Bräse, S.; Samuel, I. D. W. Direct observation of intersystem crossing in a thermally activated delayed fluorescence copper complex in the solid state. *Sci. Adv.* **2016**, *2*, e1500889.
- (106) Yersin, H.; Strasser, J. Triplets in metal-organic compounds. Chemical tunability of relaxation dynamics. *Coord. Chem. Rev.* **2000**, *208*, 331-364.
- (107) Schmidt, J.; Wiedenhofer, H.; von Zelewsky, A.; Yersin, H. Time-Resolved Vibrational Structures of the Triplet Sublevel Emission of Pd(2-thpy)<sub>2</sub>. *J. Phys. Chem.* **1995**, *99*, 226-229.
- (108) Henderson, B.; Imbusch, G. F. *Optical Spectroscopy of Inorganic Solids*. Clarendon Press: Oxford, 1989.
- (109) Manenkov, A. A.; Orbach, R. *Spin-Lattice Relaxation in Ionic Solids*. Harper & Row: New York, 1966.
- (110) Abragam, A.; Bleaney, B. *Electron Paramagnetic Resonance of Transition Ions*. Clarendon Press: Oxford, 1970.
- (111) Scott, P. L.; Jeffries, C. D. Spin-Lattice Relaxation in Some Rare-Earth Salts at Helium Temperatures; Observation of the Phonon Bottleneck. *Phys. Rev.* **1962**, *127*, 32-51.
- (112) Orbach, R.; Blume, M. Spin-Lattice Relaxation in Multilevel Spin Systems. *Phys. Rev. Lett.* **1962**, *8*, 478-480.
- (113) Prokhorov, A. M.; Hofbeck, T.; Czerwieniec, R.; Suleymanova, A. F.; Kozhevnikov, D. N.; Yersin, H. Brightly luminescent Pt(II) pincer complexes with a sterically demanding carboranyl-phenylpyridine ligand – A new material class for diverse opto-electronic applications. *J. Am. Chem. Soc.* **2014**, *136*, 9637-9642.
- (114) Finkenzeller, W. J.; Stöbel, P.; Yersin, H. Emission and absorption of Ir(ppy)<sub>2</sub>(CO)(Cl) – temperature dependence, phosphorescence decay dynamics, and assignment of excited states. *Chem. Phys. Lett.* **2004**, *397*, 289-295.
- (115) Yersin, H.; Mataranga-Popa, L.; Czerwieniec, R. Design of organic TADF molecules. The role of  $\Delta E(S1-T1)$ : From fluorescence to TADF and beyond – towards the fourth generation OLED mechanism. **2017**, *Design of organic TADF molecules. The role of  $\Delta E(S1-T1)$ : From fluorescence to TADF and beyond – towards the fourth generation OLED mechanism*, 22nd International Krutyn Summer School, Krutyn, <http://www.excilight.eu/node/203> (July 12, 2020).
- (116) Yersin, H.; Mataranga-Popa, L.; Czerwieniec, R., Organische Moleküle für Direktes Singulett-Harvesting mit kurzer Emissionsabklingzeit zur Verwendung in optoelektronischen Vorrichtungen European patent: EP 17170682.3, **2017** and German patent DE 10 2017 101432.2, **2017**.

- (117) Yersin, H.; Mataranga-Popa, L.; Czerwieniec, R.; Dovbii, Y. Design of a New Mechanism beyond Thermally Activated Delayed Fluorescence toward Fourth Generation Organic Light Emitting Diodes. *Chem. Mater.* **2019**, *31*, 6110-6116.
- (118) Shi, S.; Jung, M. C.; Coburn, C.; Tadde, A.; Sylvinson, D.; Djurovich, P. I.; Forrest, S. R.; Thompson, M. E. Highly Efficient Photo- and Electroluminescence from Two-Coordinate Cu(I) Complexes Featuring Nonconventional N-Heterocyclic Carbenes. *J. Am Chem. Soc* **2019**, *141*, 3576-3588.
- (119) Rössler, U.; Yersin, H. Destabilization of a self-trapped exciton in a quasi-one-dimensional semiconductor: Mg[Pt(CN)<sub>4</sub>]•7H<sub>2</sub>O with hydrostatic pressure. *Phys. Rev. B* **1982**, *26*, 3187-3191.
- (120) Gliemann, G.; Yersin, H., Spectroscopic Properties of the Quasi One-Dimensional Tetracyanoplatinate(II) Compounds. In *Clusters*, Springer Berlin Heidelberg: Berlin, Heidelberg, 1985; pp 87-153.
- (121) Hager, G. D.; Watts, R. J.; Crosby, G. A. Charge-transfer excited states of ruthenium(II) complexes. II. Relation of level parameters to molecular structure. *J. Am Chem. Soc* **1975**, *97*, 7037-7042.
- (122) Both values DE(S<sub>1</sub>-T<sub>1</sub>) and k(S<sub>1</sub>→S<sub>0</sub>), are correlated as is discussed in detail in refs. [36] and [37]. The values determined for compound **2** fit well to the trend found for a large number of Cu(I) complexes (compare figure 12 of ref. [36]).
- (123) A more detailed description that takes the temperature dependence of the TADF intensity into account is found in SI section 6 of ref. [59].
- (124) Ratzke, W.; Bange, S.; Lupton, J. M. Direct Detection of Singlet-Triplet Interconversion in OLED Magneto-electroluminescence with a Metal-Free Fluorescence-Phosphorescence Dual Emitter. *Phys. Rev. Applied* **2018**, *9*, 054038.
- (125) Noda, H.; Nakanotani, H.; Adachi, C. Excited state engineering for efficient reverse intersystem crossing. *Sci. Adv.* **2018**, *4* : eaa06910, 1-7.
- (126) Chen, X.-K.; Kim, D.; Brédas, J.-L. Thermally Activated Delayed Fluorescence (TADF) Path toward Efficient Electroluminescence in Purely Organic Materials: Molecular Level Insight. *Acc. Chem. Res.* **2018**, *51*, 2215-2224.
- (127) Samanta, P. K.; Kim, D.; Coropceanu, V.; Brédas, J.-L. Up-Conversion Intersystem Crossing Rates in Organic Emitters for Thermally Activated Delayed Fluorescence: Impact of the Nature of Singlet vs Triplet Excited States. *J. Am. Chem. Soc.* **2017**, *139*, 4042-4051.
- (128) Penfold, T. J.; Gibson, J., The role of Vibronic Coupling for intersystem crossing and reverse intersystem crossing rates in TADF molecules. In *Highly Efficient OLEDs: Materials Based on Thermally Activated Delayed Fluorescence*, Yersin, H., Ed. Wiley-VCH: Weinheim, 2019; pp 297-330.
- (129) Davydov, A. S. The Theory of Molecular Excitons. *Sov. Phys. Usp.* **1964**, *7*, 145-178.
- (130) Hesse, M.; Meier, H.; Zeeh, B.; Hesse, M.; Meier, H.; Zeeh, B. *Spectroscopic Methods in Organic Chemistry, 2nd Edition 2007*. Thieme: 2014.
- (131) Yersin, H.; Gliemann, G. Spectroscopic Studies of M<sub>x</sub>[Pt(CN)<sub>4</sub>] · yH<sub>2</sub>O. *Ann. N. Y. Acad. Sci.* **1978**, *313*, 539-559.
- (132) Day, P. Excitons in one-dimensional tetracyanoplatinate salts. *J. Am. Chem. Soc.* **1975**, *97*, 1588-1589.

- (133) Chen, X.-K.; Tsuchiya, Y.; Ishikawa, Y.; Zhong, C.; Adachi, C.; Brédas, J.-L. A New Design Strategy for Efficient Thermally Activated Delayed Fluorescence Organic Emitters: From Twisted to Planar Structures. *Adv. Mater.* **2017**, *29*, 1702767.
- (134) Azumi, T.; Miki, H. Spectroscopy of the Spin Sublevels of Transition Metal Complexes. *Top. Curr. Chem.* **1997**, *191*, 1-40.
- (135) Siebrand, W. Radiationless Transitions in Polyatomic Molecules. I. Calculation of Franck—Condon Factors. *J. Chem. Phys.* **1967**, *46*, 440-447.
- (136) Robinson, G. W.; Frosch, R. P. Electronic Excitation Transfer and Relaxation. *J. Chem. Phys.* **1963**, *38*, 1187-1203.
- (137) Iwamura, M.; Watanabe, H.; Ishii, K.; Takeuchi, S.; Tahara, T. Coherent Nuclear Dynamics in Ultrafast Photoinduced Structural Change of Bis(diimine)copper(I) Complex. *J. Am. Chem. Soc.* **2011**, *133*, 7728-7736.
- (138) Jesser, A.; Rohrmüller, M.; Schmidt, W. G.; Herres-Pawlis, S. Geometrical and optical benchmarking of copper guanidine—quinoline complexes: Insights from TD-DFT and many-body perturbation theory. *J. Comput. Chem.* **2014**, *35*, 1-17.
- (139) Niehaus, T. A.; Hofbeck, T.; Yersin, H. Charge-transfer excited states in phosphorescent organo-transition metal compounds: a difficult case for time dependent density functional theory? *RSC Advances* **2015**, *5*, 63318-63329.
- (140) Kim, D. Effects of Intermolecular Interactions on the Singlet–Triplet Energy Difference: A Theoretical Study of the Formation of Excimers in Acene Molecules. *J. Phys. Chem. C* **2015**, *119*, 12690-12697.
- (141) Often, the decay behavior of powder materials is modified, for example, by processes of energy transfer or triplet-triplet annihilation. However, if the low-lying molecular states show distinct geometry distortions such as found for Cu(I) or Ag(I) complexes, localization (self-trapping) can occur and prevent, for example, energy transfer effects. Thus, the emission of the powder material can essentially display the molecular properties.[12, 36, 37].
- (142) Yersin, H.; Donges, D.; Nagle, J. K.; Sitters, R.; Glasbeek, M. Intraligand Charge Transfer in the Pd(II) Oxinate Complex Pd(qol)<sub>2</sub>. Site-Selective Emission, Excitation, and Optically Detected Magnetic Resonance. *Inorg. Chem.* **2000**, *39*, 770-777.
- (143) Strasser, J.; Homeier, H. H. H.; Hartmut, Y. Triplet sublevels of metal organic complexes – temperature dependence of spin–lattice relaxation. *Chem. Phys.* **2000**, *255*, 301-316.
- (144) Murov, S. L.; Carmichael, J.; Hug, G. L. *Handbook of Photochemistry*, 2<sup>nd</sup> ed. Marcel Dekker: New York: 1993; p 340.
- (145) McHale, J. L. *Molecular Spectroscopy*. Prentice Hall, Englewood: NJ 1999; p 159.
- (146) Szabo, A.; Ostlund, N. S. *Modern Quantum Chemistry: Introduction to Advanced Electronic Structure Theory*. Dover Publications, Mineola, New York: 1989; p 86.
- (147) Lamansky, S.; Djurovich, P. I.; Murphy, D.; Abdel-Razzaq, F.; Lee, H.-E.; Adachi, C.; Burrows, P. E.; Forrest, S. R.; Thompson, M. E. Highly Phosphorescent Bis-Cyclometalated Iridium Complexes: Synthesis, Photophysical Characterization, and Use in Organic Light Emitting Diodes. *J. Am. Chem. Soc.* **2001**, *123*, 4304–4312.

(148) Adachi, C.; Baldo, M. A.; Thompson, M. E.; Forrest, S. R. Nearly 100% internal phosphorescence efficiency in an organic light-emitting device. *J. Appl. Phys.* **2001**, *90*, 5048-5051.

## Danksagung

An dieser Stelle möchte ich mich bei allen Personen bedanken, die zum erfolgreichen Abschluss dieser Dissertation beigetragen haben. Ich bedanke mich bei ...

...Herrn Prof. Dr. Hartmut Yersin für die herzliche Aufnahme in seinem Arbeitskreis und für die vielen ausführlichen Diskussionen während meiner Promotionszeit

... Herrn Prof. Dr. Bernhard Dick für die Bereitstellung von Laboren und diversen Geräten sowie für die sehr angenehme Arbeitsatmosphäre am Lehrstuhl für Physikalische und Theoretische Chemie

...allen ehemaligen und aktuellen Mitarbeitern am Arbeitskreis von Herrn Prof. Dr. Hartmut Yersin: Herrn Axel Bolz, Herrn Dr. Rafal Czerwieniec, Frau Dr. Larisa Mataranga-Popa, Herrn Dr. Markus Leitl, Herrn Dr. Thomas Hofbeck insbesondere Herrn Marsel Z. Shafikov, Frau Dr. Alfiya F. Suleymanova, Herrn Shu-Wei Li und Frau Dr. Mahboubeh Jamshidi für all die wissenschaftlichen Diskussionen und die wunderschöne Zeit, die ich mit euch verbringen durfte

...Frau Madeleine von Sanden-Flohe für die Unterstützung bei Fragen bezüglich der Labore

...allen wissenschaftlichen und nicht-wissenschaftlichen Mitarbeitern des Lehrstuhls für Physikalische und Theoretisch Chemie für das kollegiale Arbeitsklima

...Kooperationspartnern Herrn Dr. Nicholas Rau (Universität Marburg), der Arbeitsgruppe von Herrn Prof. Rongmin Yu (State Key Laboratory of Structural Chemistry, Fujian Institute of Research on the Structure of Matter, Chinese Academy of Sciences, Fuzhou, Fujian), Herrn Dr. Thomas Baumann, Herrn Dr. Daniel Zink, (Cynora GmbH), Frau Dr. Alfiya F. Suleymanova sowie Herrn Marsel Z. Shafikov für das Bereitstellen der gemessenen Verbindungen

...Herrn Randy Rückner für die Lösung aller Probleme bei der Nutzung des High Performance Clusters des Rechenzentrums der Universität Regensburg

... allen Mitarbeitern der Glasbläserei, die auch die Reparatur von sehr herausfordernden (Quarz)Glasbrüchen gemeistert haben

...meinen Eltern für die fortwährende Unterstützung während meiner gesamten Promotionszeit

## Erklärung

Ich versichere hiermit, dass ich die vorliegende Arbeit selbst verfasst und keine anderen als die angegebenen Quellen und Hilfsmittel verwendet habe.

Regensburg, den \_\_\_\_\_

---

Alexander Schinabeck